On Speckle Patterns: Integrating Spheres, Metrology, and Beyond

Morgan Facchin

University of
St Andrews

This thesis is submitted in partial fulfilment for the degree of
Doctor of Philosophy (PhD)
at the University of St Andrews

September 2022

Declaration

Candidate's Declaration

I, Morgan Facchin, do hereby certify that this thesis, submitted for the degree of PhD, which is $(3.10 \pm 0.03) \times 10^4$ words in length, has been written by me, and that it is the record of work carried out by me, or principally by myself in collaboration with others as acknowledged, and that it has not been submitted in any previous application for any degree. I confirm that any appendices included in my thesis contain only material permitted by the 'Assessment of Postgraduate Research Students' policy.

I was admitted as a research student at the University of St Andrews in January 2019. I received funding from an organisation or institution and have acknowledged the funder(s) in the full text of my thesis.

Date 3/10/2023 Signature of candidate

Supervisor's Declaration

I hereby certify that the candidate has fulfilled the conditions of the Resolution and Regulations appropriate for the degree of PhD in the University of St Andrews and that the candidate is qualified to submit this thesis in application for that degree. I confirm that any appendices included in the thesis contain only material permitted by the 'Assessment of Postgraduate Research Students' policy.

Date 3/10/2023 Signature of supervisor

Permission for publication

In submitting this thesis to the University of St Andrews we understand that we are giving permission for it to be made available for use in accordance with the regulations of the University Library for the time being in force, subject to any

copyright vested in the work not being affected thereby. We also understand, unless exempt by an award of an embargo as requested below, that the title and the abstract will be published, and that a copy of the work may be made and supplied to any bona fide library or research worker, that this thesis will be electronically accessible for personal or research use and that the library has the right to migrate this thesis into new electronic forms as required to ensure continued access to the thesis. I, Morgan Facchin, confirm that my thesis does not contain any third-party material that requires copyright clearance. The following is an agreed request by candidate and supervisor regarding the publication of this thesis:

Printed Copy

No embargo on print copy.

Electronic Copy

Embargo on part (Chapter 8) of electronic copy for a period of 2 years on the following ground(s): Publication would preclude future publication

Supporting statement for electronic embargo request
The content of Chapter 8 will be the subject to future publications.

Title and Abstract

I agree to the title and abstract being published.

Date	3/10/2023	Signature of candidate
Date	3/10/2023	Signature of supervisor

Underpinning Research Data or Digital Outputs

Candidate's declaration

I, Morgan Facchin, understand that by declaring that I have original research data or digital outputs, I should make every effort in meeting the University's and research funders' requirements on the deposit and sharing of research data or research digital outputs.

Date	3/10/2023	Signature of candidate

Permission for publication of underpinning research data or digital outputs

We understand that for any original research data or digital outputs which are deposited, we are giving permission for them to be made available for use in accordance with the requirements of the University and research funders, for the time being in force.

We also understand that the title and the description will be published, and that the underpinning research data or digital outputs will be electronically accessible for use in accordance with the license specified at the point of deposit, unless exempt by award of an embargo as requested below.

The following is an agreed request by candidate and supervisor regarding the publication of underpinning research data or digital outputs: No embargo on underpinning research data or digital outputs.

Permission for publication of underpinning research data or digital outputs

I wish to embargo the digital outputs, as I intend to publish based upon them.

Date	3/10/2023	Signature of candidate
Date	3/10/2023	Signature of supervisor

Publications and Presentations

Publications

- "Measuring picometre-level displacements using speckle patterns produced by an integrating sphere", **M. Facchin**, G. D. Bruce, K. Dholakia, *ArXiv preprint* (2021): 2110.15939.

- "Measurement of variations in gas refractive index with 10^{-9} resolution using laser speckle", **M. Facchin**, G. D. Bruce, K. Dholakia, *ACS Photonics* 9 (3) (2022): 830-836.

- "Wavelength sensitivity of the speckle patterns produced by an integrating sphere", **M. Facchin**, K. Dholakia, G. D. Bruce, *JPhys Photonics* 3 (3) (2021): 035005.

- "Speckle-based determination of the polarisation state of single and multiple laser beams", **M. Facchin**, G. D. Bruce, K. Dholakia, *OSA Continuum* 3 (5) (2020): 1302-1313.

- "Femtometer-resolved simultaneous measurement of multiple laser wavelengths in a speckle wavemeter", G. D. Bruce, L. O'Donnell, M. Chen, **M. Facchin**, K. Dholakia, *Optics Letters* 45 (7) (2020): 1926-1929.

Presentations

- "Optimizing laser speckle production and analysis for high precision metrology", Photonics West, San Francisco, January 2022

- "Wavelength sensitivity of the speckle patterns produced by an integrating sphere", Photonics West, San Francisco, January 2022

- "Speckle metrology", Second year PhD talks, St Andrews, June 2020

- "Speckle metrology", Group seminar, St Andrews, September 2021

Posters

- "Speckle Metrology", Third year PhD poster session, St Andrews, June 2021

Awards

- Arthur Maitland Prize (University of St Andrews), best talk (second place), 2020

Acknowledgements

I would like to express my deep gratitude to my two supervisors, Kishan Dholakia and Graham Bruce, who have always been very supportive throughout my PhD. A special thank to Kishan for offering me this opportunity, and a special thank to Graham for his excellent day-to-day guidance.

A big thanks as well for all those who crossed my path in St Andrews, who helped create a wonderful atmosphere and memory. Thanks to them for forgiving (and sometimes even entertaining) my eccentric passions, such as Mr Bean, The Queen, and Ducks.

Also, I am grateful to the random chain of events that brought me to Crail in May 2019 and led me to discover the Clipper Seriously Velvet Instant Hot Chocolate, the missing piece to my special Mocha, without which I might not have had the energy to complete this work.

I would also like to thank Covid, in a certain way, for providing the isolation and contemplative mood necessary to the mathematical exercise pursued in this thesis.

More seriously, this is perhaps the occasion to thank my two high school teachers, René Ruiz and Vincent Robert, who sparked in me the love of Physics and Math, respectively. As well as a few characters that were of importance in my academic path, in chronological order: Rémi Blancon, Elisabeth Pozzo Di Borgo, Philippe Beltrame, Arnaud Mesgouez, Hassan Safouhi, Walter Kob, Francis Auclair, Richard Fournier, Gabriel Fruit, Alain Blanchard, Hervé Carfantan, Brahim Lamine, Thierry Roudier, and last but not least, Arturo Lopez Ariste.

Finally, I would like to thank my two assessors, Friedrich Koenig and Thomas Charrett, for lending their time to the review process and providing valuable feedback.

Funding

The work presented in this thesis was funded by St Leonard Research Scholarship, the Leverhulme Trust (RPG-2017-197), and the UK Engineering and Physical Sciences Research Council (EP/P030017/1).

Research Data/Digital Outputs access statement

Research data underpinning this thesis are available at the following links, for each work that has been published in peer-reviewed journals.

Model:
https://doi.org/10.17630/323aebbc-6063-4f71-be41-0e73b45d4997

Wavelength:
https://doi.org/10.17630/d7026c4c-0310-48cc-8b09-bdebec307333

Refractive index:
https://doi.org/10.17630/f19b1d1f-5064-4575-bad5-a50d15ba2f34

Polarisation:
https://doi.org/10.17630/386f6c3f-df00-4415-a24b-33fd8494e483

Abstract

"There are certain Phænomena of this scatter'd Light, which when I first observed them, seem'd very strange and surprizing to me."
– Isaac Newton, *Optiks*

Speckle patterns are grainy intensity patterns resulting from the random interference of light. They often arise from the interaction of light with systems that have a complex structure at the scale of the wavelength. As most ordinary objects have this property, speckle patterns are a somewhat universal phenomenon, although not easily observable under ordinary circumstances due to the lack of coherence of natural light. Since the invention of lasers however, the production of speckle patterns has become extremely simple, and a whole field of optics has emerged from it.

Speckle patterns are an excellent tool for metrology. Where intuition says that precise control over all aspects of a setup is required, it is found that introducing some disorder can lead to very powerful techniques, with considerably simpler implementations.

In this thesis, we explore new theoretical aspects of speckle patterns and develop new metrology techniques. We pay particular attention to the case of speckle patterns produced by an integrating sphere, which has only recently been used in this field of study. In this geometry, we develop a general model that predicts the amount of change in the resulting speckle, as a result of an arbitrary transformation. This model gives explicit results for various physical effects that can be solved from first principles, such as a variation in wavelength, refractive index, temperature, and position. We use this model in the context of metrology, and improve the state of the art by several orders of magnitude in the case of refractive index variations and displacement. We also explore the relationship between speckle and polarisation, and describe new mathematical techniques for the design of speckle patterns with custom properties (i.e. with maximal and minimal sensitivity to a measurand of interest) using light shaping.

Contents

Chapter 1

Introduction

List of symbols and abbreviations

E	complex field
N	number of scatterers
ρ	amplitude of the field from one scatterer
ϕ	phase of the field from one scatterer
a	global amplitude of the field
θ	global phase of the field
$\mathcal{R}$	real part of the field
$\mathcal{I}$	imaginary part of the field
σ	standard deviation of $\mathcal{R}$ and $\mathcal{I}$
f	probability density function
I	intensity of light

1.1 What are speckle patterns?

Speckle patterns are random interference patterns, characterised by a grainy structure. The simplest illustration of a speckle phenomenon is the following. Take a laser pointer (preferably green[1]), shine it on an optically rough[2] surface (such as paper, plastic, or wood), and observe the diffused light, as projected onto a wall for example. The diffused light does not appear uniform, but has a granular structure: this is a speckle pattern. An example of speckle produced in this way is shown in Fig. 1.1, along with an example of higher quality speckle obtained in the laboratory,

[1] A green laser is ideal to observe the effect with the naked eye, as the eye has a peak of sensitivity in the green, if we assume most laser pointers have similar powers.

[2] Microscopically, rough means that the surface fluctuations are large compared to the wavelength. Empirically, it means any surface that does not produce a specular reflection.

whose details of production will be discussed in Chapter 2.

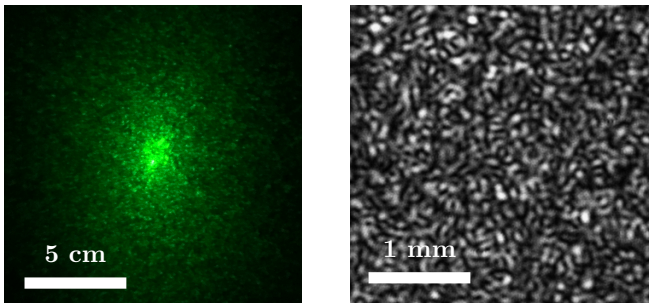

Figure 1.1: Left: an "everyday life" speckle pattern, obtained by shining a green laser pointer on a piece of white plastic. The picture shows the diffused light projected onto a wall. The granular structure of the intensity profile is a characteristic feature of speckle patterns. Right: an example of speckle pattern obtained in the laboratory.

The explanation of this effect lies in the combination of two factors: the coherence of the light, and the roughness of the surface. When illuminated, each point of the surface acts as a source of secondary spherical waves. The coherence implies that those secondary waves interfere with each other, and the roughness implies that each of them leaves the surface with a phase randomly distributed on the interval $[0, 2\pi]$. What we have on the wall then is a superposition of many spherical waves with random phases and slightly different directions of propagation, which produces a random interference pattern, as illustrated in Fig. 1.2. In some points the interference is constructive, producing bright spots, in others destructive, producing dark spots. This results in the typical granular structure shown in Fig. 1.1. Both coherence and roughness are essential. If we have non coherent light shining on a rough surface, we obtain a uniform diffused light. If we have coherent light shining on a non rough (smooth) surface, we obtain a specular reflection.

1.2 Historical retrospective

The observation of speckle patterns became inevitable after the invention of lasers, the first of which was built in 1960 [1]. Three nearly simultaneous papers published between 1962 and 1963 [2–4] describe the phenomenon.

However, observations of speckle phenomena precede the invention of lasers. Indeed, the required coherence of the source mentioned in the previous section can be either temporal or spatial. Lasers have a high temporal coherence, which makes speckle production simplest, but speckles can also be observed with spatially coherent light instead, although in much more delicate conditions. This can be observed

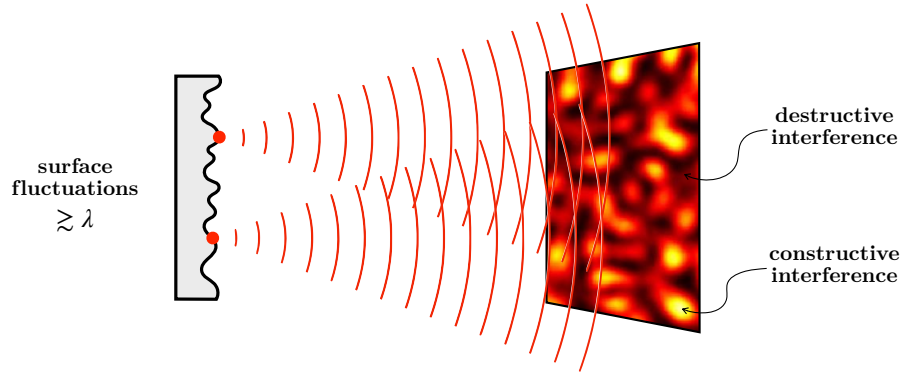

Figure 1.2: When illuminated, each point of a rough surface acts as a source of spherical waves. These interfere in the far field, forming randomly distributed regions of constructive and destructive interference, resulting in the typical granular structure of speckle. The input beam is not represented for clarity.

in everyday life, by using a small and bright source of white light (such as an LED) illuminating a shiny rough surface (such as aluminium foil or brushed metal). When the eye is placed approximately in the specular direction, where the diffused light is brightest, the surface glitters with coloured speckle patterns. An example of such pattern is shown in Fig. 1.3. Sunlight is also a good source for this observation, and with a trained eye, this can be seen on all sorts of surfaces such as wood or even skin.

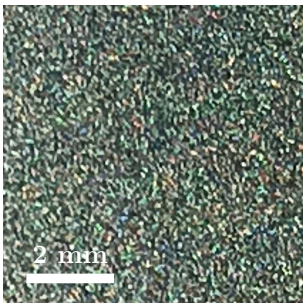

Figure 1.3: An example of speckle pattern which arises from the spatial coherence of light, rather than temporal coherence. The image shows the surface of brushed metal illuminated by an LED from a distance of about 1 m, observed in the specular direction.

Unfortunately the historical aspects surrounding these early (pre-laser) observations are rather disjointed. A few books and articles [5–7], as well as on the reputable Wikipedia [8], state that speckle phenomena were first reported by Newton, without however giving references to attest it. It took me some personal research to find the first occurrence of this statement, which seems to be in a chapter written by Françon in 1975 in "Laser speckle and related phenomena" [9], one of the first comprehensive books on the subject (according to Goodman [10, Chapter 1.1]). In this chapter the

reference is simply *Opticks* by Newton (1704) [11], with no more details. The interested reader of the time would have to wait 4 years before learning more. In 1979 Françon wrote his own book "Laser Speckle and Applications in Optics" (one of the other few comprehensive books on speckle, still according to Goodman), where he refers to the work of Newton in *Opticks*, Book II, Part IV, titled "Observations concerning the Reflexions and Colours of thick transparent polish'd Plates". There Newton reports observations on the interference of light scattered by impurities on the surface of a concave mirror, forming irregular coloured rings at the focal point of the mirror. At the very start of this chapter can be read "There are certain Phænomena of this scatter'd Light, which when I first observed them, seem'd very strange and surprizing to me". This might be the first written record of the wonders of random light, from one of the great figures of physics, and for that reason deserved to serve as an inspirational quote in the abstract of this thesis.

In a much more recent book from 2009, Gustavo and Pomarico [12] argue that Newton made another observation of speckle-like phenomena in *Opticks*. In Book I, Part I, Prop. VIII, titled "To shorten Telescopes", Newton reports on the effect of a turbulent atmosphere on the image of a star, in relation to the length and aperture size of the telescope, and describes observations that are reminiscent of a stellar speckle.

Concerning the work made in the 256 years between Newton and the first laser, there seems to be different versions of history. According to Françon [13], Young (1802) used the wave theory of light to explain the phenomena observed by Newton, as well as Stokes who gave a more general theory in 1851. He notes that Herschel also studied speckle phenomena (1830). Another paper by Hariharan [14] gives a historical retrospective, and mentions other works. According to them, the first observation of speckle was made by Exner in 1877, while studying diffraction from randomly distributed particles, and the first theoretical description made by von Laue in 1914.

1.3 Modelling speckle patterns

In this section we describe a simple approach to model speckle patterns, from which we will derive a few fundamental properties that will be useful later.

Consider a source of temporally coherent light impinging on a rough surface and scattered onto an observation plane, as shown in Fig. 1.4. This is essentially a continuous problem that would involve some delicate maths to model the diffusion of the incident field. However, we shall for the moment only consider the statistical

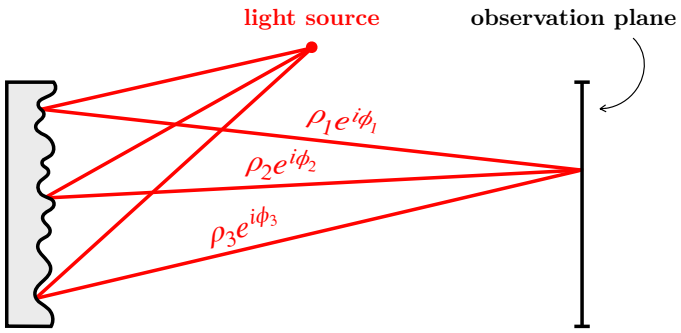

Figure 1.4: In order to infer the statistical properties of speckle patterns, we can make a simple model where we consider a set of discrete scatterers randomly distributed on the rough surface. Any point of the observation plane receives a contribution from each scatterer (three of which are shown), modelled as a complex number, which add coherently.

properties of speckle. To this end, a great simplification is to make a discrete model where we only consider discrete scatterers randomly distributed on the rough surface. By this choice of description we lose all information on the detailed spatial properties of the scattered field, but retain all the statistical information. For now, let us use a scalar model of light, where the field is described by a single complex number $\rho e^{i\phi}$, with ρ the amplitude and ϕ the phase (two real numbers). For completeness, the use of complex numbers in this context is discussed in Appendix A. One single complex number describes a speckle pattern that is fully polarised[3], for example a speckle that goes through a polariser before reaching the observation plane. Each point of the observation plane receives the sum of the contributions of each scatterer, so that the resulting field can be expressed as

$$E(\mathbf{r},t) = \frac{1}{\sqrt{N}} \sum_{n=1}^{N} \rho_n(\mathbf{r}) e^{i\phi_n(\mathbf{r},t)}, \tag{1.1}$$

where each term of the sum corresponds to the contribution of one scatterer, with a total of N scatterers. All quantities are functions of position on the observation plane $\mathbf{r}$ (in the rest of this thesis, bold fonts designate vectors), and as we consider monochromatic light, only the phase contains a time dependence in the form of a ωt term. This time dependence is not important here and we shall omit it for clarity. The factor $1/\sqrt{N}$ is a normalisation constant to ensure that the intensity (proportional to $|E|^2$) is finite when N goes to infinity, so that our model is consistent with a real situation.

Note that in this model, and in the rest of this thesis, light is described by an

[3]Or more precisely, that has a constant state of polarisation across the observation plane.

underlying physical quantity simply denoted as "the field". This imprecise denomination is intentional, since the knowledge of the actual nature of light is unnecessary to perform wave optics derivations. This is in fact the elegant power of wave optics, where the mere assumption of a wave nature is sufficient to provide the formal basis of modelling. As a matter of fact, the foundational works on wave optics by Young and Fresnel (1807 and 1818 respectively) preceded by about 50 years the synthesis of electromagnetism by Maxwell (1865). From our modern knowledge of the nature of light we will only keep one letter, E for electric[4], to designate the field.

Let us now introduce some common assumptions that will greatly simplify the derivations:

- The amplitude $\rho_n(\mathbf{r})$ and phase $\phi_n(\mathbf{r})$ are statistically independent.
- The amplitudes $\rho_n(\mathbf{r})$ and $\rho_m(\mathbf{r})$ are statistically independent (for $n \neq m$) and similarly for $\phi_n(\mathbf{r})$ and $\phi_m(\mathbf{r})$.
- The phase $\phi_n(\mathbf{r})$ is uniformly distributed on a 2π-interval.

A speckle pattern verifying these assumptions is called a *fully developed speckle*. These three assumptions have direct consequences on the statistics of the field on the observation plane. To better appreciate them, we introduce the following notations: $E(\mathbf{r}) = a(\mathbf{r})e^{i\theta(\mathbf{r})} = \mathcal{R}(\mathbf{r}) + i\mathcal{I}(\mathbf{r})$, where $a(\mathbf{r})$ is the global amplitude and $\theta(\mathbf{r})$ the global phase, $\mathcal{R}(\mathbf{r})$ the real part and $\mathcal{I}(\mathbf{r})$ the imaginary part of the field. The average value of a quantity across the observation plane is denoted by an overbar. The consequences are the following

1. **The average field is zero.** We have $\overline{\mathcal{R}(\mathbf{r})} = 0$, $\overline{\mathcal{I}(\mathbf{r})} = 0$, and $\overline{E(\mathbf{r})} = 0$. Also, we have $\overline{\mathcal{R}(\mathbf{r})\mathcal{I}(\mathbf{r})} = 0$, which means that $\mathcal{R}(\mathbf{r})$ and $\mathcal{I}(\mathbf{r})$ are uncorrelated.

2. **$\mathcal{R}(\mathbf{r})$ and $\mathcal{I}(\mathbf{r})$ are Gaussian random variables of the same statistics.** $\mathcal{R}(\mathbf{r})$ and $\mathcal{I}(\mathbf{r})$ have the same variance, that we shall denote σ^2 ($\sigma^2_{\mathcal{R}} = \sigma^2_{\mathcal{I}} = \sigma^2$), whose precise value depends on the initial probability density of ρ in (1.1). Moreover, as $\mathcal{R}(\mathbf{r})$ and $\mathcal{I}(\mathbf{r})$ are both sums of a large number of independent random variables, the central limit theorem implies that they are Gaussian random variables, with mean 0 and variance σ^2. Taking N to infinity, the joint probability density of $\mathcal{R}$ and $\mathcal{I}$ is given by

$$f(\mathcal{R}, \mathcal{I}) = \frac{1}{2\pi\sigma^2}\, e^{-\frac{\mathcal{R}^2+\mathcal{I}^2}{2\sigma^2}}. \tag{1.2}$$

[4]Note however that light can equally be described by its magnetic component, although this is an often forgotten truth. In fact, the total energy density (or flux) of an electromagnetic wave is equally divided between its electric and magnetic components.

When plotting this density in the $\mathcal{R}-\mathcal{I}$ plane, it is circularly symmetric around the origin. For this reason E is said to be a *circular complex Gaussian* random variable, or just *circular Gaussian*[5].

3. **The global amplitude of the field is Rayleigh-distributed, and the global phase is uniformly distributed.** Using the relationship between (a, θ) and $(\mathcal{R}, \mathcal{I})$, namely $(\mathcal{R} = a\cos\theta, \mathcal{I} = a\sin\theta)$, we can find the probability density of a and θ from that of $\mathcal{R}$ and $\mathcal{I}$ (Eq. (1.2)) using variable transformation rules. We find

$$f(a,\theta) = \frac{a}{2\pi\sigma^2}\, e^{-\frac{a^2}{2\sigma^2}}. \tag{1.3}$$

As $f(a, \theta)$ does not depend on θ, it means that the probability density of θ is uniform, just like the phase of each individual component of (1.1). The probability density of a is then

$$f(a) = \frac{a}{\sigma^2}\, e^{-\frac{a^2}{2\sigma^2}}, \tag{1.4}$$

which is called a Rayleigh distribution.

Let us now turn our attention to the statistics of intensity, which is what is most commonly measured. The intensity is power per unit area. It is proportional to the time average of the field's square modulus

$$I(\mathbf{r}) \propto \langle |E(\mathbf{r},t)|^2 \rangle, \tag{1.5}$$

where the angled brackets denote time averaging. We do not give the exact proportionality constant implied[6], as, again, in the spirit of wave optics, we do not need to know what the field actually is. Here we simply invoke a general property of waves, which is that the energy density is proportional to the field's square modulus. In the case of monochromatic light, the time dependence can be fully factored out in a complex exponential of the form $E(\mathbf{r}, t) = E_0(\mathbf{r})e^{i\omega t}$, and therefore disappears when taking the square modulus. We can then omit the time averaging and simply write $I(\mathbf{r}) \propto |E(\mathbf{r})|^2$.

4. **The probability density of intensity of a polarised speckle is an exponential function.** Using our previous notations, we have $I(\mathbf{r}) = a^2(\mathbf{r})$.

[5] Or in fact any combination of the words *complex*, *circular*, and *Gaussian*.

[6] Actually, it is $cn\epsilon_0/2$.

Using this relation, we can find the probability density of I by again using the rules of variable transformation, and we find

$$f(I) = \frac{1}{2\sigma^2} e^{-\frac{I}{2\sigma^2}}, \tag{1.6}$$

which is an exponential distribution, expressed in terms of σ which is a property of the underlying field. From this we find that the average intensity is $\overline{I} = 2\sigma^2$, we can then rewrite $f(I)$ in terms of intensity only

$$f(I) = (1/\overline{I}) e^{-I/\overline{I}}. \tag{1.7}$$

So far we have assumed a scalar model of light, where light is described by a single complex number. In the general case, however, the field has two independent components. Indeed, the field most often reaches a detector in a paraxial geometry and close to normal incidence, and has two components within the observation plane. The field is then described by a 2D vector containing the components of the field along two perpendicular axes, say x and y:

$$\mathbf{E}(\mathbf{r}) = \begin{pmatrix} a_x(\mathbf{r}) e^{i\theta_x(\mathbf{r})} \\ a_y(\mathbf{r}) e^{i\theta_y(\mathbf{r})} \end{pmatrix}. \tag{1.8}$$

If the diffusion process does not favour one particular polarisation of light, each component of $\mathbf{E}(\mathbf{r})$ has the same properties as the scalar field described above, and $\mathbf{E}(\mathbf{r})$ is said to be non-polarised. The intensity is now defined as $I(\mathbf{r}) \propto |\mathbf{E}(\mathbf{r})|^2 = \mathbf{E}^*(\mathbf{r}) \cdot \mathbf{E}(\mathbf{r}) = \mathbf{E}^\dagger(\mathbf{r})\mathbf{E}(\mathbf{r})$, where we can either use the dot product of the field with its complex conjugate, or use the language of matrices and use a matrix product with the conjugate transpose (denoted by †).

5. **The intensity of a non-polarised speckle is gamma-distributed.** For a fully vector speckle field, we then have $I(\mathbf{r}) = a_x^2(\mathbf{r}) + a_y^2(\mathbf{r})$, where $a_x^2(\mathbf{r})$ and $a_y^2(\mathbf{r})$ are the intensities corresponding to the x and y component of the field (it is a simple sum, as both components are perpendicular). We derived above the statistics of each individual component. The sum of two such components give the following probability density

$$f(I) = 1/\left(\overline{I_x} - \overline{I_y}\right) \left(e^{-I/\overline{I_x}} - e^{-I/\overline{I_y}}\right), \tag{1.9}$$

where $\overline{I_x} = \overline{a_x^2(\mathbf{r})}$ and $\overline{I_y} = \overline{a_y^2(\mathbf{r})}$ are the average speckle intensities on the x and y component, assuming $\overline{I_x} > \overline{I_y}$. In the general case $\overline{I_x}$ and $\overline{I_y}$ can be

different, for example if the scattering surface is conductive, one component may be favoured. If both are equal however, as obtained when using a non-conductive surface (such as paper), the probability density simplifies to

$$f(I) = 4I/\overline{I}^2 \, e^{-2I/\overline{I}}, \tag{1.10}$$

where $\overline{I}$ is now the average total speckle intensity ($\overline{I} = \overline{I_x} + \overline{I_y}$). This is known as a gamma distribution of shape parameter 2.

Those are the main statistical properties of speckle patterns. The detailed derivation of each point can be found in [10, Chapters 2, 3.2.1, 3.3.3]. It is worth keeping those properties in mind, as misconceptions exist on this matter in the optics community, and have been source of confusion in a few interactions I had with other researchers of the field.

1.4 What is the point of speckle?

The advantages of speckle patterns mainly lie in two aspects. First, they are very simple to produce and observe. For example, a speckle produced by reflection on a rough surface can be observed using a camera[7] directly in free space, positioned anywhere within the illuminated area, without the need of any fine alignment. The diffusion process has the effect of spreading light in space and making it more readily observable. Second, depending on the diffusion process involved, speckle can display a very high sensitivity to some physical parameters of interest. This is typically the case when the diffusion process implies multiple reflections. We will exploit this extensively by use of the integrating sphere in the coming chapters.

In this line of thought, speckle patterns have been applied to a variety of problems: the measurement of velocity fields in fluids [15], the detection of heartbeat [16] and blood pressure [17], the measurement of vibration [18, 19], spacial mapping of blood flow in tissues [20, 21], spectroscopy [22–25], the detection of cracks in art pieces [26], and velocimetry for robotics [27] and autonomous vehicles [28]. In a different vein, speckle patterns are also important in astronomy, where techniques exploit them to circumvent the effect of the atmosphere to achieve diffraction limited imaging of astronomical objects [29, 30].

[7] By camera I mean a chip (CCD or CMOS) directly exposed to the light, without any intermediate lens.

1.5 Structure of this thesis

In this thesis, we will explore new ideas in the field of speckle patterns, both theoretical and experimental.

Chapter 2 describes the key experimental aspects for the production of speckle patterns, and give a summary of the experimental parameters found in the rest of this thesis.

Chapter 3 is devoted to the analytical study of speckle patterns produced by an integrating sphere, which is a new and largely unexplored way of producing speckles, for which a general theory is lacking. We will develop a model that predicts the change occurring in the speckle pattern as a result of an arbitrary transformation.

Chapter 4 is devoted to the experimental verification of the model in the particular case of a wavelength variation, where excellent agreement if found. Analytical results are also found along the way that are of importance for the field of speckle-based measurement of wavelength and spectra.

In Chapter 5 we apply the model to the case of refractive index variations in a metrological perspective. We describe a new method that allows the measurement of refractive index variations as small as 4.5×10^{-9}, which is a 3 orders of magnitude improvement over the previous best speckle-based method.

In Chapter 6 we apply the model to the case of displacement measurement, where we demonstrate the measurement of 17 pm amplitude motion, or 6 times smaller than a hydrogen atom. This might constitute one of the simplest interferometric setups, as it requires no fine alignment, and contains only 3 simple elements: a laser, an integrating sphere, and a camera.

In Chapter 7 we explore the relationship between the polarisation of an incident laser beam and the speckle pattern it produces. We find that the speckle image is linearly related to the Stokes parameters of the incident beam. We derive this in an original way and exploit it in a metrological perspective to measure the polarisation of the incident beam. The method utilises a set of reference polarisation states to estimate that of the incident beam, which is based on simple linear algebra, and is generalisable to multiple beams.

In Chapter 8, we explore new ways of customising the properties of a speckle pattern by shaping the structure of the incident beam. In particular, we give a set of original methods to minimise and maximise the sensitivity of the speckle pattern to a physical parameter of interest.

Chapter 2

A short guide to speckle production

In this chapter we give a short review of the key parameters involved in speckle experiments, as well as some aspects of the experimental implementation that are common throughout this thesis.

List of symbols and abbreviations

λ	wavelength of light
ω	angular frequency of light
E	complex field
I	intensity of light
N	number of scatterers
D	distance between scatterer and observation plane
A	area of the input beam
W_{beam}	width of the input beam
A_c	correlation area of the speckle field
W_{grain}	average width of a speckle grain
NA	numerical aperture
a	fibre core size

2.1 Different ways of producing speckle patterns

At the start of Chapter 1 we introduced the simplest way to produce speckle patterns, which is reflection on a rough surface. The two other most commonly used diffusers are ground glass (which can be used in reflection or transmission) and multimode optical fibres. These are shown in Fig. 2.1. Multimode fibres are a non trivial example as they do not themselves contain disorder. Yet, when laser light is

coupled into the input facet of a multimode fibre, a speckle is formed at the output. This happens because the different modes of the fibre acquire different phases along propagation due to their different phase velocities [10, Chapter 7.1]. This destroys the structure of the input field and creates a random interference pattern. Another less common way of producing speckles is by the multiple reflections of light inside an integrating sphere. This was used extensively throughout this thesis and Chapter 3 is dedicated to the theory of speckle produced in this way.

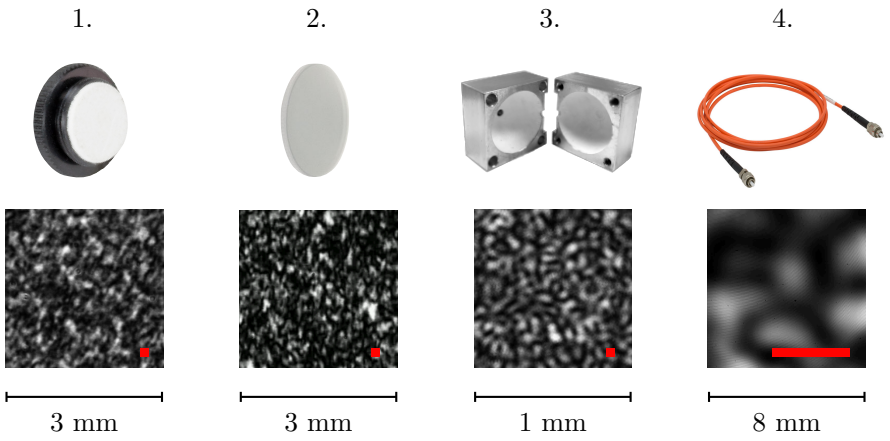

Figure 2.1: Different systems used to generate speckles and examples of obtained speckles. 1. Rough surface, 2. ground glass, 3. integrating sphere, 4. multimode fibre. The inset red square (or line for 4.) shows the expected speckle grain size, as computed from Eq. (2.2).

The speckle patterns shown in Fig. 2.1 were produced in the following way. Speckle 1: Reflection on a rough surface, made of a 1 mm thick spectralon-like white diffuse reflective material (Thorlabs SM05CP2C), recorded at a distance of 20 cm. Speckle 2: Transmission through a piece of ground glass (DG05-220-MD), recorded at a distance of 20 cm. Speckle 3: Multiple reflections of light inside an integrating sphere, the light escapes the sphere via a 3 mm diameter hole, situated 20 cm away from the camera. Speckle 4: Light is coupled into the input facet of a multimode fibre (Thorlabs M115L01) in free space, and the output facet is placed 10 cm away from the camera. In all cases, the input light was a 1 mm width laser beam of 780 nm wavelength and 10 mW, and the light was shone directly onto the CMOS chip without any intermediate lens.

2.2 Speckle grain size

An experimental parameter of importance is the speckle grain size. Consider a simple diffusion geometry such as the reflection on a rough surface or transmission

through a rough diffuser, with a distance of propagation large compared to the wavelength and the spot size. The geometry is depicted in Fig. 2.2 for the case of transmission. The speckle grain size can be estimated analytically by computing the autocorrelation of the speckle intensity profile [10, section 4.4.1], from which we infer the correlation correlation area A_c, given by

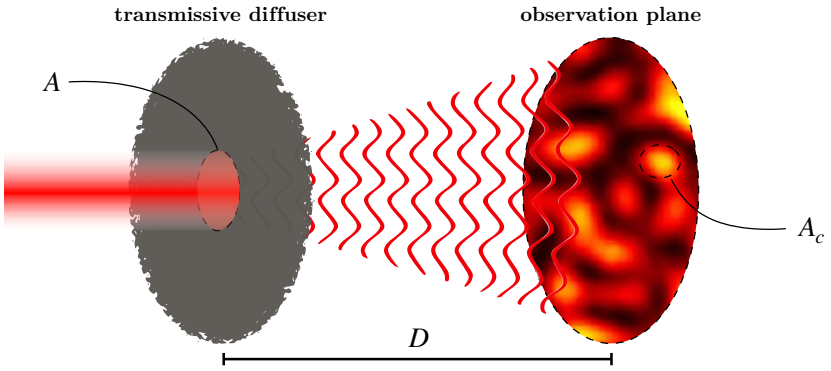

Figure 2.2: Diffusion geometry. A laser beam of cross-sectional area A impinges on a transmissive diffuser, and a speckle is formed at a distance D with a typical grain size A_c. The relationship between A, D, and A_c is given by Eq. (2.1).

$$A_c = \frac{(\lambda D)^2}{A}, \tag{2.1}$$

with λ the wavelength of the input beam, A its cross-sectional area, and D the distance between the diffuser and the observation plane. This expression is for an input beam of uniform intensity and any shape. For an arbitrary input beam, we have an additional factor of the order of unity. We can use A_c as a measure of the speckle grain area, and a corresponding measure of the one-dimensional width of a speckle grain is given by the square root:

$$W_{grain} = \frac{\lambda D}{W_{beam}}, \tag{2.2}$$

where W_{grain} is the typical width of a speckle grain and W_{beam} is the beam width. For the speckles 1 and 2 of Fig. 2.1, the parameters are $W_{beam} = 1$ mm, $\lambda = 780$ nm, and $D = 20$ cm, which gives $W_{grain} = 156\,\mu$m. An inset red square shows this length in Fig. 2.1.

We can apply the same relation to the case of speckle patterns produced by an integrating sphere. In this case A in Eq. (2.1) has to be taken equal to the area of

the output port, with D the distance between the output port and the observation plane. Alternatively, one can take A equal to the area of the region at the back surface of the sphere "visible" from the observation plane, with D the distance between the back surface and the observation plane. This leads to the same result as the two surfaces vary in the same proportion as D^2. In fact, any intermediate plane can be chosen as the source of speckle field. For a port diameter of 3 mm, $\lambda =$ 780 nm, and $D = 20$ cm, we find $W_{grain} = 52\,\mu$m. An inset red square shows this length in Fig. 2.1.

For the case of fibres, we can estimate the speckle grain size from the total number of speckle grains and the size of the illumination area. The number of speckle grains is approximately equal to the number of modes supported by the fibre, which is given by $2\pi(NA)a/\lambda$, with NA the numerical aperture, a the core radius, and λ the wavelength. The illumination area is approximately $\pi D^2(NA)^2$, with D the distance from the output facet. The ratio gives a speckle grain area of $(NA)\lambda D^2/(2a)$. The square root gives the speckle grain size $W_{grain} = \sqrt{(NA)\lambda/(2a)}D$. For the fibre used in Fig. 2.1, we have $NA = 0.2$, $a = 50\,\mu$m, $\lambda = 780$ nm, and $D = 10$ cm, which gives $W_{grain} = 4$ mm. An inset red line shows this length in Fig. 2.1.

Similarity (see section 3.2) is the main computation performed with speckle images in this thesis. In this particular case, the result is found to be very little dependent on speckle grain size. Empirically, the speckle grain size can be taken down to a few pixels without observing any significant change in the similarity. Small speckle grains are obtained when the camera is close to the speckle source, allowing to collect more power, which is generally desirable.

2.3 Recording speckle patterns

When recording speckle patterns using a camera, two parameters must be adjusted to obtain recordings of good quality: the exposure time and the black level. The exposure time must be chosen so as to maximise the global intensity, while at the same time minimising saturation. The black level (which applies a global shift to the intensity) must be adjusted to eliminate background light, while not discarding any speckle light. Both parameters can be adjusted by looking at the intensity distribution of the speckle image: the exposure time is adjusted by looking at the saturation peak in the intensity distribution, and the black level is adjusted such that the start of the distribution coincides with the origin. An example of correct intensity distribution is shown in Fig. 2.3, which is that obtained from speckle 3 of Fig. 2.1, together with the theoretical gamma distribution 1.10. Note that

the reason for deviation of the observed distribution from the gamma distribution around zero is unknown.

If any computation is performed on the speckle images, the variance of the final output decreases as the size of the images increases. However, as the image size increases, the computation time also increases. A balance must be found between the variance of the final output and computation time. In the context of this thesis we found that 200×200-pixel images offer a good compromise.

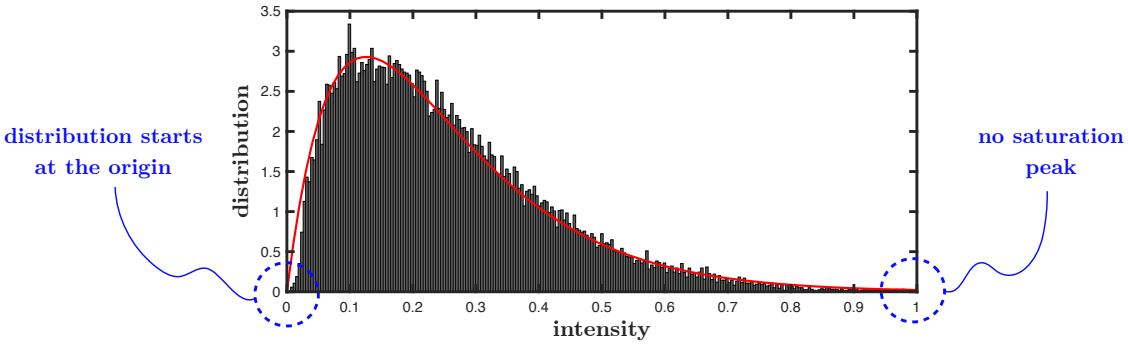

Figure 2.3: Black: example of a measured intensity distribution with correct values of exposure time and black level, where the distribution starts at the origin and shows no saturation peak (1 is the saturation value). Red: theoretical gamma distribution for a non-polarised speckle.

2.4 Experimental parameters common throughout this thesis

To avoid repetition, we compile here a few experimental parameters that are common to the experiments involved in this thesis.

The source of light is a Toptica DL Pro laser, which is a tunable diode laser with a mode-hop free tuning range of about 20GHz. Its specifications are: wavelength of 780 nm, linear polarisation with $>$ 100:1 extinction ratio, and coherence length of the order of kilometres (linewidth down to 10 kHz). It is used with a typical power of 10 mW.

The source of speckle patterns is either an integrating sphere (Chapters 4, 5, and 6), or a rough surface (Chapter 7), and in either case the camera is located 20 cm away from it, which is the same conditions as used in the examples of Fig. 2.1. The rough surface is a Thorlabs SM05CP2C, and the integrating sphere is a custom made spherical cavity carved in a 3 cm edge aluminium cube, with a radius $R = 1.25$ cm and a reflectivity $\rho = 0.918$. The inner surface of the sphere is coated

with several layers of Spectraflect, applied manually with a paintbrush, to give a near Lambertian reflectance. The sphere is made of two separate hemispheres, and bears two 3 mm diameter holes, located at 90° from each other. One hole is used to inject light while the other is used for collection. The hole receiving the input light must be different from the hole by which light escapes, otherwise direct reflections can dominate the output field. A detailed description of integrating spheres and their properties is given in the next chapter.

2.5 Camera noise analysis

The camera used throughout this thesis is a CMOS Mikrotron MotionBLITZ EoSens mini2, which has 8 µm×8 µm pixels, with which 200×200-pixel images are recorded. At several occasions we will need to know what noise source dominates, and we shall show here that it is Poisson noise in our experimental conditions, i.e. the noise which originates from the photon shot noise converted to digital.

Each pixel converts a number of photons into a "grey" value, on a scale of 256 divisions that we shall call digital units. An uncertainty analysis including the photon shot noise, dark noise, rounding error, and neglecting readout noise, shows that the variance of the final output (in digital units) is given by [31]:

$$\sigma_y^2 = K^2\sigma_d^2 + \sigma_q^2 + K(\mu_y - \mu_{yd}), \tag{2.3}$$

where σ^2 designates the variance, μ the average, y the final grey value from 0 to 255, K the overall system gain (which converts the initial number of electrons into a grey value, in digital unit per electron), q is the rounding error (coming from the quantisation of y into 256 levels), and yd the amount of output grey value coming from the dark signal.

We want to find an estimation of each term. From the specifications of the CMOS chip, we estimate $K = 0.0096/e^-$, $\sigma_d = 21\ e^-$, and the dark signal $\mu_{yd} = 67T$, with T the exposure time (in seconds). σ_q^2 is equal to $1/12$, and μ_y is found empirically. In our setups the average intensity is about 0.2 times the saturation value, or a grey value of about 51. Using a typical value $T = 3$ ms, and conserving the same order of the terms, we have

$$\sigma_y^2 = 0.04 + 0.08 + (0.49 - 0.002). \tag{2.4}$$

We see that in our experimental conditions the μ_y term (corresponding to the

photon shot noise) dominates. This gives a noise on the grey value of $\sigma_y \approx 0.8$, although this value will not be used in the rest of this thesis.

The Value of K is found by using the full well charge (27000 e^-), and the conversion gain (39.2 µV/e^-), and μ_{yd} is found from the dark signal (277 mV/s).

Chapter 3

Speckle produced by an integrating sphere

The work presented in this chapter was published in [32].

List of symbols and abbreviations

S	speckle similarity (Pearson correlation coefficient of intensity)
C	field correlation (Pearson correlation of the complex field)
I	speckle intensity
σ_I	standard deviation of speckle intensity
$\boldsymbol{E}$	3D complex field
R, ρ	radius and reflectivity of an integrating sphere
p	path taken in the sphere
P	power
ϕ	phase variation applied to the field
M	number of surface elements constituting the surface of the sphere
N	number of chords constituting a path in the sphere
μ	average phase variation of the field on a chord
σ	standard deviation of the phase variation of the field on a chord
k	wavenumber
HWHM	half width at half maximum
T	linear operator describing the transformation of the field
$\mathcal{F}$	Fourier transform operator
$\mathbb{1}$	identity operator, or identity matrix
N	number of chords constituting a path in the sphere
A	absorptance $(1 - \rho)$

P	power
$\mathcal{R}$	operator acting on the Jones vector (for a reflection)
$\mathbb{J}$	operator acting on the Jones vector (for an arbitrary transformation)
q	electrical charge
$\hbar$	reduced Planck's constant
$\mathbf{A}$	vector potential
t_0	HWHM in time of the similarity profile

3.1 Introduction

An integrating sphere is a spherical cavity whose inner surface is covered by a diffuse reflectance coating. It is typically used to measure the power of light sources or the reflectance properties of surfaces. The important parameters of an integrating sphere are its radius and reflectivity[1]. The coating is chosen to provide a nearly Lambertian[2] reflectance. A common coating is spectraflect, composed of barium sulfate, which can provide a reflectivity up to 0.97 in the visible. The best commercial spheres are made of spectralon, a soft thermoplastic (fluoropolymer), which can provide a reflectivity higher than 0.99.

A integrating sphere can be used to generate speckle patterns in the following way. A beam of laser light is inserted via a small aperture, and undergoes multiple reflection inside the sphere. If the sphere is equipped with another small aperture, a small fraction of the light will escape by it after each reflection (see Fig. 3.1). The escaping light forms a speckle pattern.

This is a non-standard use of integrating spheres. Speckles produced in this way were first studied in [33], where the first and second order statistics of speckle were characterised. Since then, a few works mentioned the speckles encountered while using coherent light with integrating spheres, but those were seen as nuisance or limitations [34–36]. Before the work presented in this thesis, deliberate harnessing of such speckle patterns had been restricted to two purposes: measuring the modulation transfer function of optical systems [37, 38] and measuring small wavelength variations [39–42] (see Chapter 4). The latter is the topic that initiated the study of speckles in my group. Speckle patterns produced in this way were empirically

[1] The reflectivity of a surface is a number between 0 and 1 defined as the fraction of incident power that is reflected by the surface

[2] A surface presents a Lambertian reflectance if its apparent surface brightness depends on the direction of illumination, but not on the direction of observation.

found to be highly sensitive to any perturbation. However, a complete theoretical understanding of such speckles was missing. In this chapter we propose to make a model to characterise the change of speckle patterns produced by an integrating sphere resulting from an arbitrary transformation. The term *transformation* refers to any effect that changes the intensity/phase/polarisation of light in the sphere. This can be a deformation of the sphere, a wavelength change, or more exotic effects. A few examples of such transformations are given in section 3.3 and are treated in subsequent chapters of this thesis. For the moment, however, we will remain as general as possible.

3.2 Model

Our purpose is to characterise the change occurring in the speckle as a result of a transformation. We first need a tool to quantify this change. A natural choice is the following quantity:

$$S = \left\langle \left(\frac{I - \langle I \rangle}{\sigma_I} \right) \left(\frac{I' - \langle I' \rangle}{\sigma_{I'}} \right) \right\rangle, \tag{3.1}$$

with I and I' two speckle images (before and after the transformation), σ_I and $\sigma_{I'}$ their respective standard deviation, the brackets denoting averaging over the image. This gives a value of 1 for identical images and decreases towards 0 as they diverge from one another. In the rest of this thesis, this quantity will be referred to as *similarity*. It is formally the same as the Pearson correlation coefficient (or normalised covariance). However as it applies to images, and not realisations of random variables, we shall use the term similarity instead of correlation.

Our problem statement is the following. A beam of monochromatic light enters an integrating sphere of radius R and uniform reflectivity ρ via a small aperture. The light undergoes multiple reflections inside the sphere and escapes via another small aperture. A schematic setup is shown in Fig. 3.1. We consider that the inner surface is rough to the wavelength used, and presents a Lambertian reflectance. We now apply a transformation to the system, and we want to estimate the resulting change in the speckle, as quantified by the similarity (3.1).

Finding the answer to this question will essentially consist of expressing the similarity in terms of the field (rather than the intensity), inserting an expression for the field that takes into account its journey through the sphere, and do some algebraic manipulation. This will lead us to a general expression for the similarity (Eq. (3.14)) which depends only on the reflectivity of the sphere and some statistics

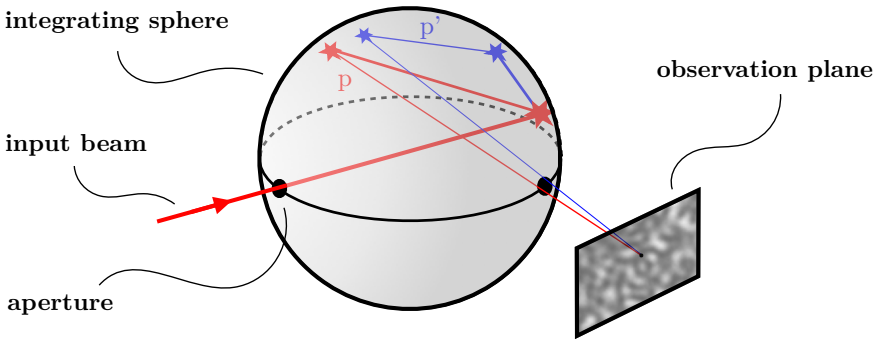

Figure 3.1: Geometry of the problem. Laser light enters an integrating sphere via a small aperture and undergoes multiple diffusive reflections. The diffusive reflections imply that light takes all the possible paths through the sphere. Two such paths, p and p', are represented. Light exits the sphere via another small aperture and forms a speckle pattern on the observation plane.

of the transformation.

We start by expressing the observed intensity pattern in terms of the underlying field, modelled by a 3D complex-valued vector field:

$$I \propto |\boldsymbol{E}|^2 = \boldsymbol{E}^\dagger \boldsymbol{E}, \tag{3.2}$$

with I the intensity, $\boldsymbol{E}$ the 3×1 field, and $\dagger$ denoting the conjugate transpose. Here we keep the full 3D nature of the field, as we work in an arbitrary coordinate system, not necessarily one aligned with the observation plane. I and $\boldsymbol{E}$ are functions of space in the observation plane, but we omit this dependency for clarity. We have similarly $I' \propto \left|\boldsymbol{E}'\right|^2$, with $\boldsymbol{E}'$ the field after the transformation. If we assume a fully developed speckle, it can be shown [10, section 3.3.4] that the similarity can be expressed in terms of the field as

$$S = \left| \frac{\left\langle \boldsymbol{E}^\dagger \boldsymbol{E}' \right\rangle}{\sqrt{\left\langle \boldsymbol{E}^\dagger \boldsymbol{E} \right\rangle} \sqrt{\left\langle \boldsymbol{E}'^\dagger \boldsymbol{E}' \right\rangle}} \right|^2 . \tag{3.3}$$

The quantity inside the absolute square will be denoted as the *field's correlation*. Here we conserve the term *correlation* in order to make it more distinct and use the letter C, reading $S = |C|^2$, that we shall use again many times.

This can be simplified assuming that the average intensity does not change after

transformation, giving

$$S = \left| \frac{\left\langle \boldsymbol{E}^\dagger \boldsymbol{E}' \right\rangle}{\left\langle \boldsymbol{E}^\dagger \boldsymbol{E} \right\rangle} \right|^2 . \tag{3.4}$$

We can now decompose $\boldsymbol{E}$ by modelling the journey of the light between the illuminated region and the observation plane. For simplicity of the algebra, we make a discrete model of the system where the inner surface is described as an assembly of M surface elements. As light is diffused in every direction when hitting an element of the inner surface, the field on the observation plane is the sum of the fields coming from all possible paths inside the sphere. This can be expressed as

$$\boldsymbol{E} = \sum_p \boldsymbol{E}_p. \tag{3.5}$$

with $\boldsymbol{E}_p$ the contribution of the light going through path p. Each path is a succession of surface elements between which light propagates in straight lines before reaching the observation plane. The total number of paths that light can take is of course infinite, one can think for example of an arbitrarily long alternation between the two same elements. This decomposition assumes that the coherence length of the light is large compared to the spread of the path-length distribution in the sphere (equal to $4R/(3|\ln\rho|)$), so that the different contributions $\boldsymbol{E}_p$ add coherently. The path-length distribution was derived in [43], and an alternative derivation is given in Appendix B. Inserting this decomposition in (3.4), we have

$$S = \left| \frac{\sum_p \left\langle \boldsymbol{E}_p^\dagger \boldsymbol{E}'_p \right\rangle}{\sum_p \left\langle \boldsymbol{E}_p^\dagger \boldsymbol{E}_p \right\rangle} \right|^2 , \tag{3.6}$$

using the fact that the fields coming from different paths are uncorrelated. We can now express $\boldsymbol{E}_p$ as the product of an amplitude, phase, and polarisation term, of the form

$$\boldsymbol{E}_p = \sqrt{I_p}\, e^{i\varphi_p} \boldsymbol{u}_p, \tag{3.7}$$

where I_p, φ_p, and $\boldsymbol{u}_p$ are respectively the intensity, phase, and Jones vector[3] of the light coming from p onto the observation plane. For the field after transformation, $\boldsymbol{E}'_p$, the change could happen in any of the three terms. However we will (for the

[3]The Jones vector, sometimes called the polarisation vector, is a 3D (or 2D in a paraxial description) complex vector describing the state of polarisation. It can be simply defined as "what is left" once the modulus and the phase of the electric field are factored out.

moment) focus on transformations that affect the field in the phase term only, as this covers most of the phenomena addressed in this thesis. The reason for this will become clear when we will look at particular examples. We can then write $\boldsymbol{E}'_p = \boldsymbol{E}_p e^{i\phi_p}$, with ϕ_p the phase shift[4] introduced by the transformation. Inserting those expressions for $\boldsymbol{E}_p$ and $\boldsymbol{E}'_p$ in (3.6), we have

$$S = \left| \frac{\sum_p \left\langle \left(\sqrt{I_p} e^{-i\varphi_p} \boldsymbol{u}_p^\dagger \right) \left(\sqrt{I_p} e^{i\varphi_p} \boldsymbol{u}_p e^{i\phi_p} \right) \right\rangle}{\sum_p \left\langle \left(\sqrt{I_p} e^{-i\varphi_p} \boldsymbol{u}_p^\dagger \right) \left(\sqrt{I_p} e^{i\varphi_p} \boldsymbol{u}_p \right) \right\rangle} \right|^2 , \tag{3.8}$$

and using the fact the the Jones vector has unit norm ($\boldsymbol{u}_p^\dagger \boldsymbol{u}_p = 1$), we find

$$S = \left| \frac{\sum_p P_p e^{i\phi_p}}{\sum_p P_p} \right|^2 , \tag{3.9}$$

where intensity I_p is converted into power P_p (the total power coming from path p onto the observation region) via the space averaging. We can recognise in (3.9) a weighted average of the phase factors, where the weights are given by the power. This lends itself to a visual interpretation in the complex plane (see Fig. 3.2). Plotting each phase factor as a point in the complex plane (one for each path) forms an infinite cluster lying on the unit circle. The similarity is the square of the distance between the barycentre[5] of this cluster and the origin. When no transformation is applied ($\phi_p = 0$ for all paths), all the points are at $1 + 0i$ and the similarity is therefore 1 (no speckle change). As the effect of a transformation increases, the points spread out on the unit circle and the barycentre approaches the origin (hence a decreasing value of the similarity) until the points are uniformly spread, where the similarity is close to zero.

Eq. (3.9) is general but not readily usable as it is. We can recast it in a more explicit form by a series of manipulations. We first invoke the spherical geometry and the Lambertian reflectance, which both conspire in such a way that P_p decreases by a constant factor at every reflection along the path. To see this, consider one surface element emitting a power P in the volume of the sphere, and another element receiving a fraction of this power. By definition of the Lambertian reflectance, the

[4] As we will refer to this phase shift a lot in the following, we will sometimes call it simply *phase* for concision.

[5] The barycentre is an extension of the notion of centre of mass, where the weighting is not given by mass but any other quantity.

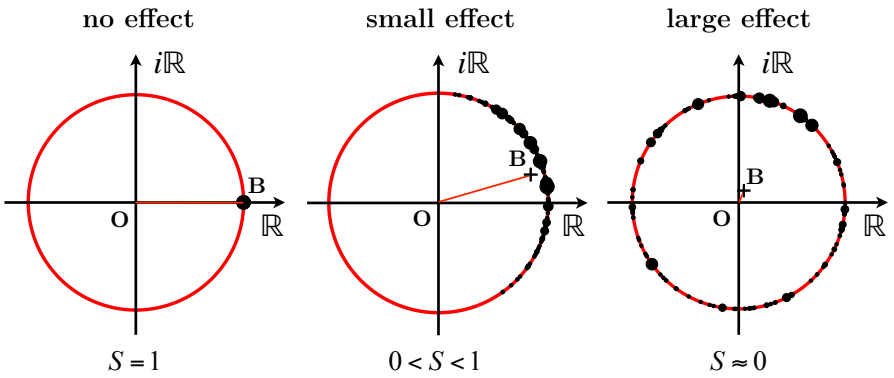

Figure 3.2: Visual representation of equation (3.9). Each possible path is represented by a black dot, which together form an infinite cluster on the unit circle of the complex plane. The size and azimuthal position represent respectively the power carried through the path (P_p) and the phase shift induced by the transformation on the path (ϕ_p). The similarity (S) is equal to the square of the distance between the origin (O) and the barycentre of the cluster (B). We show three stages where the effect of the transformation increases from zero to large.

received power is $P' = P\rho\,\delta S\cos\theta_1\cos\theta_2/(\pi d^2)$ [44], with d the distance between the elements, θ_1 and θ_2 the angles between their normal and the line joining them, and δS their area. Now the spherical geometry imposes a relation between these quantities, namely $d = 2R\cos\theta$, with $\theta = \theta_1 = \theta_2$. Inserting this in the expression of P', and considering a total number M of surface elements (which gives $\delta S = 4\pi R^2/M$), we are left with $P' = P\rho/M$. We can see in this factor the combined effects of the absorption (ρ) and the distribution of the power among all surface elements ($1/M$). This distribution is simplest in the case of Lambertian reflectance as the power is equally distributed among the surface elements. It follows that the power decreases by a factor $(\rho/M)^N$ after N reflections, independently of the details of the path, which is a great simplification of the problem.

Inserting this in (3.9), and splitting the sums into groups of paths that contain the same number N of reflections, we have

$$S = \left| \frac{\sum_N \sum_{p_N} \left(\frac{\rho}{M}\right)^N e^{i\phi_{p_N}}}{\sum_N \sum_{p_N} \left(\frac{\rho}{M}\right)^N} \right|^2 , \tag{3.10}$$

where p_N designates the set of paths containing N reflections. Rearranging the

terms gives

$$S = \left| \frac{\sum_N \rho^N \left(\frac{\sum_{p_N} e^{i\phi_{p_N}}}{M^N} \right)}{\sum_N \sum_{p_N} \left(\frac{\rho}{M} \right)^N} \right|^2 , \tag{3.11}$$

which reveals (in parenthesis) the average value of $e^{i\phi_{p_N}}$ in the set p_N (as M^N also happens to be the total number of paths in p_N). We can express this average explicitly using the following approximation. Assuming each reflection is a linear process[6], the phase ϕ_{p_N} acquired on a full path is the sum of the phases acquired on every successive single pass (or chord)[7], so that we can approximate ϕ_{p_N} by a Gaussian random variable, as a consequence of the central limit theorem. Additionally, for a Gaussian random variable $G(\mu, \sigma^2)$ with mean μ and variance σ^2, statistics tell us that the complex exponential of $G(\mu, \sigma^2)$ has mean $\langle e^{iG(\mu,\sigma^2)} \rangle = e^{i\mu - \sigma^2/2}$ [45, section 7.2.7]. Therefore, the average phase term can be expressed as $\sum_{p_N} e^{i\phi_{p_N}}/M^N = e^{iN\mu - N\sigma^2/2}$, with μ and σ^2 the mean and variance of the phase induced by the transformation on a chord. Inserting this we have

$$S = \left| \frac{\sum_N \rho^N \left(e^{iN\mu - N\sigma^2/2} \right)}{\sum_N \rho^N} \right|^2 . \tag{3.12}$$

Now we could solve this exactly using geometrical series, however this leads to a cumbersome expression. We can instead approximate[8] the sums by integrals:

$$S = \left| \frac{\int_0^\infty \left(\rho e^{i\mu - \sigma^2/2} \right)^N \mathrm{d}N}{\int_0^\infty \rho^N \mathrm{d}N} \right|^2 , \tag{3.13}$$

where we set the lower limit to $N = 0$, which has the advantage of giving a simpler

[6] Which means that the field diffused by a surface element is a linear transformation of the incident field.

[7] We define a single pass or chord as a straight line joining two surface elements of the sphere. A path is a succession of single passes / chords.

[8] This approximation consists in treating N as a continuous variable. This works if the summand is sufficiently spread out over many values of N, which is the case when ρ is high. There is then a certain value of ρ below which this approximation starts to fail. The difference between the two solutions is of the order of $(1-\rho)^2$ (see Appendix C), which is 0.01 for $\rho = 0.9$, which we shall set as our critical value below which Eq. (3.12) should be solved using geometric series.

form without altering significantly the solution. Performing the integrals finally gives

$$S = \frac{1}{\left(1 - \dfrac{\sigma^2}{2\ln\rho}\right)^2 + \left(\dfrac{\mu}{\ln\rho}\right)^2} \,. \tag{3.14}$$

This expression is valid for any transformation that applies a phase shift of average μ and variance σ^2 to the field on a chord. Note that μ is the average phase shift modulo 2π. Any effect for which the μ term dominates leads to a Lorentzian profile in μ, and any effect for which the σ^2 term dominates leads to the square of a Lorentzian in σ^2 (if we recall that $\ln \rho$ is negative). Note that a consequence of performing the integral approximation is that μ in (3.14) is actually the average phase modulo 2π (while σ can take any value). We shall however keep the same symbol for simplicity, as in practice μ never exceeds 2π. We list here the different assumptions made throughout this model:

1. The input light has a coherence length large compared to the spread of the path-length distribution

2. The inner surface has a Lambertian reflectance with uniform reflectivity

3. The transformation changes only the phase of the light

4. The diffusion is linear

5. $\rho \gtrsim 0.9$

Other assumptions used in the model are consequences of these, for example the monochromaticity is implied in assumption 1, the fact that the speckle is fully developed is implied in assumption 2, and the fact that the total intensity of the speckle does not change after transformation is implied in assumption 3.

To conclude, it is essential to note that a statement such as "average phase" is ambiguous if we do not specify the random process by which a random chord is defined. This is directly analogous to the Bertrand paradox, quite known in the mathematical culture, where different answers are obtained when different random processes are used to define a random chord in a circle. Contrary to the Bertrand paradox, we are in the context of a physical problem, and therefore only one answer must be correct. The correct random process here is that of a chord whose endpoints are chosen with a uniform probability density across the inner surface. This definition will be used implicitly in the rest of this thesis whenever averages are computed. The reason why this random process is the correct one is hidden in Eq. (3.11). Indeed, the notion of average arose there because we summed over all possible paths between discrete surface elements, and those surface elements uniformly cover the inner surface by design.

3.3 Examples of transformation

As until now the notion of transformation was purposely kept abstract, if not mysterious, let us see a few examples. A list of possible transformations which are all consistent with the assumptions of our model is given in Table 3.2. We give the phase shift ϕ applied to a given chord in the sphere, its mean $\mu = \overline{\phi}$, and standard deviation $\sigma = \sqrt{\overline{\phi^2} - \overline{\phi}^2}$, where the bar designates averaging over the random chords in the sphere. The expressions of μ and σ found in this way are what needs to be inserted in (3.14) to find the similarity profile of the corresponding physical effect. Table 3.2 provides by the same occasion a summary of the different effects studied in this thesis.

Transformation	Phase shift on a chord	μ	σ
Isotropic expansion	$k\,z\,\Delta R/R$	$\frac{4}{3}\,k\,\Delta R$	$\frac{\sqrt{2}}{3}\,k\Delta R$
Displacement (axial)	$k\,\boldsymbol{u}\cdot\boldsymbol{x}\,s = k\,x\,\cos\theta\,s$	$\frac{1}{3}\,k\,x$	$\frac{\sqrt{5}}{6}\,k\,x$
Displacement (transverse)	$k\,\boldsymbol{u}\cdot\boldsymbol{x}\,s = k\,x\,\sin\theta\cos\varphi\,s$	0	$\frac{1}{\sqrt{8}}\,k\,x$
Wavelength variation	$\Delta k\,z$	$\frac{4}{3}\,\Delta k\,R$	$\frac{\sqrt{2}}{3}\,\Delta k\,R$
Refractive index variation	$\Delta n\,k\,z$	$\frac{4}{3}\,\Delta n\,k\,R$	$\frac{\sqrt{2}}{3}\,\Delta n\,k\,R$

Table 3.2: Summary of the transformations studied in the different chapters of this thesis. The columns give: the transformation, the resulting phase shift on a given chord, and the corresponding average and standard deviation of the phase.

The effects mentioned in Table 3.2 refer to the following. *Isotropic expansion*: the material of the sphere expands isotropically, such as under the effect of a uniform thermal expansion. *Displacement*: the sphere is split into two independent hemispheres, one of which is fixed and the other one is free to move. Displacement refers to the motion of the free hemisphere, either away from the other hemisphere (axial) or sideways (transverse). *Wavelength variation*: the wavelength of the input light is changed. *Refractive index variation*: the refractive index of the medium filling the sphere is changed. In this table, k is the wavenumber, z is the length of

the chord considered, R is the radius of the sphere, ΔR is the radius variation, $\boldsymbol{u}$ is a unit vector parallel to the chord, $\boldsymbol{x}$ is the displacement vector, s is a variable determining if the chord does or does not change in length, θ and φ are the spherical coordinates of $\boldsymbol{u}$, Δn is the refractive index variation.

The full details of the derivations will be given in their dedicated chapters. For illustrative purposes however, let us detail one of the effects of Table 3.2, the simplest, which is wavelength variation. When light propagates in the sphere along a certain path, it acquires a phase proportional to the length of this path. More precisely, along a path of length z, it acquires a phase $k\,z$, assuming the refractive index of the medium in the sphere is close to 1. When the wavelength varies, the phase varies accordingly by $\Delta k\,z$, with Δk the corresponding wavenumber change. This phase variation is the ϕ we used in the model described above. In order to apply (3.14) and find the similarity profile, we need to consider ϕ on a given chord in the sphere, and compute its average μ and variance σ^2. If the phase change on a chord is $\phi = \Delta k\,z$, the average phase is $\mu = \overline{\phi} = \Delta k\,\overline{z}$, with $\overline{z}$ the average chord length is a sphere. This is given by geometry to be $4R/3$ [46–48][9]. Likewise, the standard deviation of chord length is $\sqrt{2}R/3$ [47, 48].

When inserting the values of μ and σ given in Table 3.2 into 3.14, we find in most cases that the μ term dominates, and that we can neglect the σ term, which leaves us with a Lorentzian profile (see Appendix D). The Lorentzian profile is a quite general feature of the integrating sphere, and we might in fact wonder what physical effect does *not* produce a Lorentzian profile. For this we need an effect such that the average phase shift μ is zero. Two effects studied in this thesis have this property: transverse displacement and the Aharonov-Bohm effect, where the resulting profile is a squared Lorentzian.

A parameter of importance that will be used extensively throughout this thesis is the Half Width at Half Maximum (HWHM) of the similarity profile. This is a useful quantity as it describes the sensitivity of the speckle to the parameter of interest.

3.4 Path-dependent vs path-independent effects

As will be shown in the next chapters, a distinctive feature of integrating spheres is that they produce speckles with a high sensitivity to various transformations, as compared to speckles produced by reflection on a rough surface. However, we can

[9] A very beautiful result of geometry shows that the average chord length of an arbitrary convex solid is equal to $4V/S$, with V the volume of the solid and S its surface area. This was originally proven by Dirac in [49] in the context of nuclear physics, on the topic of neutron absorption in a solid.

ask, is this the case for all possible transformations? The answer is no, it does so only for path-dependent ones, that is, effects that affect light differently depending on its path. All the effects mentioned in the previous section are such path-dependent effects.

Let us see an example of path-independent effect, which is a change in the input beam profile. In this case, the sensitivity is independent on the scattering process, and the multiple-scattering does not increase it. This can be shown in the following way. Assuming a fully developed speckle, the similarity is given by the absolute square of the field's correlation (see Eq. (3.3)):

$$S = \left| \frac{\left\langle \boldsymbol{E}^\dagger \boldsymbol{E}' \right\rangle}{\sqrt{\left\langle \boldsymbol{E}^\dagger \boldsymbol{E} \right\rangle} \sqrt{\left\langle \boldsymbol{E}'^\dagger \boldsymbol{E}' \right\rangle}} \right|^2 ,$$

with $\boldsymbol{E}$ and $\boldsymbol{E}'$ the field received on the observation plane before and after the change. As everywhere in this thesis, we assume a linear diffusion process, which means that the output field is a linear transformation of the incident field. We can express this as $\boldsymbol{E} = T\boldsymbol{E}_0$, where $\boldsymbol{E}_0$ is the field of the incident beam and T is a linear operator describing the transformation. Here we are modelling a change in the input field, therefore the output field is given by $\boldsymbol{E}' = T\boldsymbol{E}'_0$, where only the input field changes and not T, as the diffusing medium is fixed. Inserting this in eq. (3.3), we have

$$S = \left| \frac{\left\langle \boldsymbol{E}_0^\dagger T^\dagger T \boldsymbol{E}'_0 \right\rangle}{\sqrt{\left\langle \boldsymbol{E}_0^\dagger T^\dagger T \boldsymbol{E}_0 \right\rangle} \sqrt{\left\langle \boldsymbol{E}_0'^\dagger T^\dagger T \boldsymbol{E}'_0 \right\rangle}} \right|^2 . \tag{3.15}$$

We see that the effect of the linear transformation comes in the form of the operator $T^\dagger T$. This operator is approximately proportional to the identity operator under quite general assumptions. We can show this in two extreme cases:

1. First, consider an ideal geometry where the speckle is produced by a single reflection on a rough surface and collected in the Fraunhofer region. We can write $T \propto \mathcal{F} e^{i\phi}$, where ϕ is the phase mask applied by the rough surface and $\mathcal{F}$ is the Fourier transform operator. The $T^\dagger T$ term becomes $(\mathcal{F} e^{i\phi})^\dagger (\mathcal{F} e^{i\phi}) = e^{-i\phi} \mathcal{F}^\dagger \mathcal{F} e^{i\phi} = e^{-i\phi} \mathbb{1} e^{i\phi} = \mathbb{1}$, with $\mathbb{1}$ the identity operator, where we used the fact that the Fourier transform is a unitary transformation ($\mathcal{F}^\dagger \mathcal{F} = \mathbb{1}$).

2. Second, consider a more complex geometry where light is highly randomised (such as with an integrating sphere). In this case it is more convenient to

adopt a discrete description o the system, that is to express $\boldsymbol{E}_0$ and $\boldsymbol{E}$ not as continuous functions of space, but as vectors containing the values of the field at given points of space (this is what we have in practice, one value for each pixel). In this description T is now a matrix[10], and each element of $T^\dagger T$ can be seen as the covariance between two columns of T. If the geometry is complex enough, we expect T to be a complex random matrix with uncorrelated columns, such that $T^\dagger T$ is approximately proportional to $\mathbb{1}$ (now representing the identity matrix).

In any case laying somewhere in between those two extremes, the argument is less clear and care must be taken. Assuming $T^\dagger T \propto \mathbb{1}$ we have

$$S = \left| \frac{\left\langle \boldsymbol{E}_0^\dagger \boldsymbol{E}_0' \right\rangle}{\sqrt{\left\langle \boldsymbol{E}_0^\dagger \boldsymbol{E}_0 \right\rangle} \sqrt{\left\langle \boldsymbol{E}_0^\dagger \boldsymbol{E}_0' \right\rangle}} \right|^2 , \tag{3.16}$$

which is the absolute square of the incident field's correlation. In other words, the similarity becomes independent on the properties of the scattering medium. It follows that the width of the similarity curve (i.e. the sensitivity of the speckle) cannot be changed by a careful choice of diffusing geometry, such as multiple scattering.

At this point it is worth highlighting a few non-trivial connections that exists between the speckle similarity and the field's correlation (in this particular case of a change in the input beam). These can be summarised into four points:

- The speckle similarity (S) is equal to the square modulus of the speckle field's correlation (C) when the speckle is fully developed.
- C is equal to the correlation of the incident field C_0, if the diffusion is such that we can assume $T^\dagger T \propto \mathbb{1}$.
- the square modulus of C_0 however is not equal to the similarity of the incident intensity profile S_0, as the incident field is not fully developed in general.
- S_0 is not equal to the similarity of the speckle intensity S. This is because the line of equalities has been broken in the previous point, but also because no direct explicit relation exists between the two.

These points are illustrated in Fig. 3.3. Note that assuming a fully developed speckle might also imply $T^\dagger T \propto \mathbb{1}$ (as well as the reciprocal). This would be an

[10] This is commonly known as the transmission matrix, and is widely used in speckle analysis. We will come back to this notion in Chapter 8.

interesting point to investigate in the future, but for the moment we assume those two conditions separately.

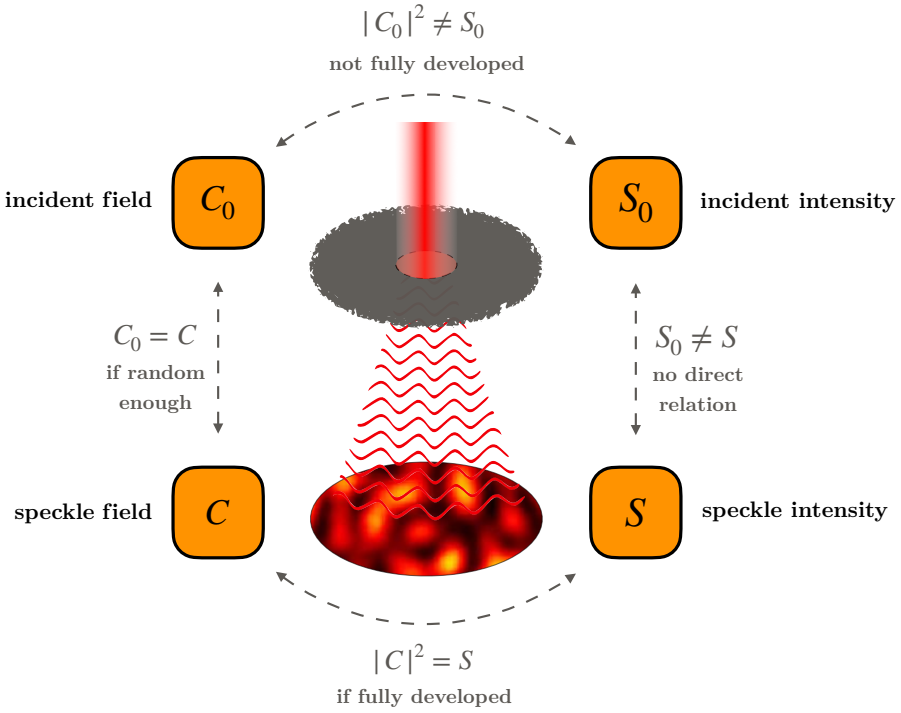

Figure 3.3: Diagrammatic summary of the relations between the incident beam and the resulting speckle. After a change in the incident beam, C_0 is the correlation of the incident field, S_0 the similarity of the incident intensity profile, C the correlation of the speckle field, and S the similarity of the speckle intensity profile.

The connections shown above have one interesting consequence, which is $S = |C_0|^2$. This implies that we can access information about the change in the input field by looking only at the resulting speckle intensity. This is notable as we can imagine situations where changes in the input field would be undetectable by looking at its intensity profile only. For example, if the phase profile or the polarisation profile of the input beam is changed, the intensity profile remains the same. Scrambling the input beam allows such phase and polarisation changes to be converted to intensity changes in the speckle, through interference. We can get a better idea of this by expressing Eq. (3.16) in more familiar terms. Writing the incident field as a function of space $\boldsymbol{E}_0(\boldsymbol{r})$, with $\boldsymbol{r}$ the position in the plane perpendicular to the direction of

propagation of the incident beam, we have

$$S = \left| \frac{\int \boldsymbol{E}_0^*(\boldsymbol{r}) \cdot \boldsymbol{E}_0'(\boldsymbol{r}) \, \mathrm{d}s}{\sqrt{\int |\boldsymbol{E}_0|^2 \, \mathrm{d}s} \sqrt{\int \left|\boldsymbol{E}_0'\right|^2 \, \mathrm{d}s}} \right|^2 , \tag{3.17}$$

where $*$ is the complex conjugate, $\mathrm{d}s$ the surface element, and $\cdot$ is the good old dot product. $\boldsymbol{E}_0(\boldsymbol{r})$ contains the amplitude, phase, and polarisation profile of the incident beam $\boldsymbol{E}_0(\boldsymbol{r}) = \rho(\boldsymbol{r}) e^{i\phi(\boldsymbol{r})} \boldsymbol{u}(\boldsymbol{r})$. For example, if we consider a change in polarisation only, with a spatially constant polarisation, we simply have

$$S = \left| \boldsymbol{u}^* \cdot \boldsymbol{u}' \right|^2 .$$

For a linear polarisation rotated by an angle α, this is $\cos^2(\alpha)$. This last example shows most strikingly how the similarity is independent of the scattering process, and we cannot hope to increase the speckle sensitivity by any choice of scattering geometry.

Another interesting consequence of Eq. (3.16) is that we can access the spatial autocorrelation of the input field in a very simple way. Indeed a global translation of the input beam can also be treated as a change of the input field. When a displacement $\boldsymbol{x}$ is applied to the input beam, the similarity is given by

$$S = \left| \frac{\int \boldsymbol{E}_0^*(\boldsymbol{r}) \cdot \boldsymbol{E}_0(\boldsymbol{r} + \boldsymbol{x}) \, \mathrm{d}s}{\int |\boldsymbol{E}_0|^2 \, \mathrm{d}s} \right|^2 , \tag{3.18}$$

which is the same as the spatial autocorrelation of a complex valued signal. We have $S = \left| R_{\boldsymbol{E}_0 \boldsymbol{E}_0}(\boldsymbol{x}) \right|^2$, with $R_{\boldsymbol{E}_0 \boldsymbol{E}_0}(\boldsymbol{x})$ the autocorrelation of $\boldsymbol{E}_0$.

3.5 Analogy with a Fabry-Pérot interferometer

There is a strong analogy between the integrating sphere and a standard Fabry-Pérot interferometer. At first approximation, which is sufficient for the present point, a Fabry-Pérot interferometer is an arrangement where a light beam is set to bounce indefinitely between two parallel mirrors, one of which is slightly transmissive (see Fig. 3.4).

After each round trip, a small portion of the light goes through the transmissive

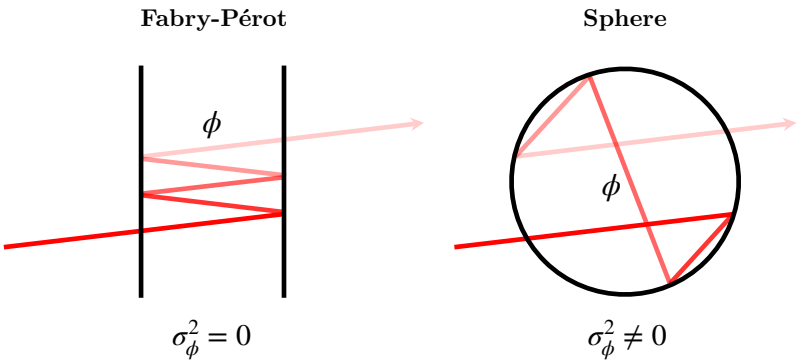

Figure 3.4: Schematic comparison between a Frabry-Pérot interferometer and an integrating sphere. In each case, light acquires a phase ϕ after each single pass. The variance of the phase is zero in the Fabry-Pérot, as light is confined to one path only, and is non zero in the sphere, as light has many paths accessible.

mirror and reaches a detector. We thus obtain on the detector the superposition of an infinite number of beams, each with an ever decreasing amplitude and increasing phase. In this simple model, the field on the detector can be expressed as

$$E \propto \sum_{N=0}^{\infty} \rho^N e^{iN\mu} \approx \int_{N=0}^{\infty} (\rho e^{i\mu})^N dN = \frac{-1}{\ln \rho + i\mu}, \tag{3.19}$$

with μ the phase[11] acquired on a round trip between the two mirrors, and ρ the reflectivity of the mirrors. The amplitude of the wave is reduced by $\sqrt{\rho}$ after each reflection, and two reflections are involved, hence the factor of ρ for each component.

The corresponding intensity $I(\mu)$, proportional to $|E|^2$, is maximal for $\mu = 0$. Let us call this maximal intensity I_{max}. If we normalise $I(\mu)$ to I_{max}, we have

$$\frac{I(\mu)}{I_{max}} = \frac{1}{1 + \left(\dfrac{\mu}{\ln \rho}\right)^2}. \tag{3.20}$$

This is a Lorentzian profile, of the same form as what we found in (3.14) for a negligible σ term. The analogy then stands between the normalised intensity of the Fabry-Pérot, and the similarity of the speckle patterns produced by an integrating sphere. This relatively simple derivation shines new light[12] on the more tedious one we carried out in section 3.2. Indeed, we saw that the combination of the Lambertian reflectance and the spherical geometry reduces the intensity of light

[11] μ is actually the phase modulo 2π, just as in (3.14). The modulo introduces a discontinuity, but this discontinuity occurs at $\mu = 2\pi$, which is far beyond the width of the intensity profile $I(\mu)$ (at least for a high reflectivity, which is already assumed).

[12] Pun unintended.

rays by a constant factor after each reflection, independently of their actual path. This property is identical to what we have here with the Fabry-Pérot. This simple observation could have led us to expect some similarity[12] between the two functional forms. The difference between the two situations is that, in the sphere, each ray can take different paths in a volume, while in the Fabry-Pérot each ray is constrained to only one, which is the round trip between the two mirrors. This introduces variability in the phase carried by the rays, which is represented by the σ term in Eq. (3.14). The Fabry-Pérot acts as a sphere with $\sigma = 0$.

Another interesting fact is that the Fabry-Pérot shows a periodic output intensity, while the sphere does not show a periodic similarity. This periodicity appears if we solve exactly the first step of (3.19) using geometrical series, instead of using an integral approximation. In this case we find $E \propto 1/(1-\rho e^{i\mu})$, which is very close to $-1/(\ln\rho + i\mu)$ for a high reflectivity, but repeats[13] every multiple of 2π. Both forms are very close for μ of the order of the HWHM of $I(\mu)$, that is for $\mu \approx \ln\rho$. The exact solution of the Fabry-Pérot keeps the memory of the phase, so to speak, and shows a revival for every integer multiple of 2π.

We may wonder however, could the similarity not also be periodic? After all, we also used the integral approximation in the derivation of (3.14). If we used geometric series instead, would we obtain a periodic similarity? It is not immediately clear which would dominate between the return of μ to zero and the effect of the σ term. We can easily answer this with the following argument. We start by solving (3.12) by geometric series, which gives

$$S = \left| \frac{1-\rho}{1-\rho e^{i\mu-\sigma^2/2}} \right|^2 . \tag{3.21}$$

In most of the effects studied in this thesis, the ratio σ/μ is a constant of the order of unity. Assuming this and setting $\mu = 2\pi$ (where we expect the revival of similarity) and $\sigma \approx 2\pi$, we find

$$S \approx \left| \frac{1-\rho}{1-\rho e^{-2\pi^2}} \right|^2 . \tag{3.22}$$

The factor $e^{-2\pi^2}$ is about 10^{-9}, so for a reflectivity close to 1 such that $1-\rho = A << 1$, we have $S \approx A^2$. This shows that no significant revival of similarity is found at $\mu = 2\pi$. The σ term does indeed dominate, and the similarity is not periodic.

[13] Note that this periodicity is already present in the integral approximation of (3.19) because of the modulo, although somehow in an artefactual way as it comes with a discontinuity.

3.6 Other exotic effects

In the derivation of (3.14), we considered only effects that change the phase of light along propagation. This, in fact, allows us to model all of the phenomena addressed in this thesis. Here we consider effects that produce a change in the two other properties of light: amplitude and polarisation. These turn out to be more "exotic" in the sense that they would be more difficult to investigate experimentally, and we treat them here for the sake of curiosity.

1. **A change in reflectivity**

One effect that would change the amplitude of a ray in the sphere is a change in reflectivity. This breaks assumption 3 and we have to work back from (3.3). Applying the path decomposition (3.5) to (3.3), we find

$$S = \left| \frac{\sum_p \left\langle \boldsymbol{E}_p^\dagger \boldsymbol{E}'_p \right\rangle}{\sqrt{\left(\sum_p \left\langle \boldsymbol{E}_p^\dagger \boldsymbol{E}_p \right\rangle \right) \left(\sum_p \left\langle \boldsymbol{E}_p'^\dagger \boldsymbol{E}'_p \right\rangle \right)}} \right|^2, \tag{3.23}$$

which is the assumption-3-free version of (3.6). As a reflectivity change would only affect the final intensity of a ray, we use $\boldsymbol{E}_p = \sqrt{I_p}\, e^{i\varphi_p} \boldsymbol{u}_p$ and $\boldsymbol{E}'_p = \sqrt{I'_p}\, e^{i\varphi_p} \boldsymbol{u}_p$. Inserting this in Eq. (3.23) and using $I \propto \rho^N$ we have

$$S = \left| \frac{\sum_N \sqrt{\rho^N \rho'^N}}{\sqrt{\left(\sum_N \rho^N \right) \left(\sum_N \rho'^N \right)}} \right|^2 \tag{3.24}$$

$$\approx \left| \frac{-1/\ln \sqrt{\rho\rho'}}{\sqrt{\left(\frac{-1}{\ln \rho} \right) \left(\frac{-1}{\ln \rho'} \right)}} \right|^2 \tag{3.25}$$

$$= \left| \frac{\sqrt{\ln \rho \, \ln \rho'}}{\ln \sqrt{\rho\rho'}} \right|^2 \tag{3.26}$$

$$= \frac{4 \ln \rho \ln \rho'}{\left(\ln \rho + \ln \rho' \right)^2}, \tag{3.27}$$

where similar decompositions as in (3.10-3.11) are used. Ideally we would like to have the similarity expressed in terms of some measure of change in the variable of interest, rather than the start and end value as it is the case here. This is more subtle to achieve with reflectivity than it was with phase, but it can be done in the following way. If we define $A = 1 - \rho$ (sometimes called the absorptance), we have $A \approx -\ln \rho$ for a high reflectivity (low absorptance). Expressed in terms of A, the similarity is

$$S = \frac{4AA'}{(A + A')^2}. \tag{3.28}$$

If the reflectivity change taking place is such that $A' = rA$ (while remaining within the approximation of low absorptance), the similarity becomes a function of r only:

$$S = \frac{4r}{(1 + r)^2}. \tag{3.29}$$

This function is shown in Fig. 3.5. This is a quite heavy-tailed function, and we have $S = 1/2$ for $r = 3 \pm \sqrt{8}$, that is for $r \approx 6$ and $r \approx 0.17$. That means that the absorptance must be multiplied by 6 or 0.17 to obtain a significant speckle change. Note that the asymmetry of the function around 1 is misleading. Indeed we can observe that multiplying by $3 + \sqrt{8}$ is equal to dividing by $3 - \sqrt{8}$. This fact is found for any value of r: multiplying the absorptance by r gives the same similarity as dividing it by r. This is reflected by the fact that (3.29) is invariant under the transformation $r \to 1/r$ (this is left as a very joyful exercise to the interested reader). With this in mind, (3.29) may also be plotted between 1 and infinity, with r being defined as either a multiplicative or dividing factor.

However, it is difficult to imagine a physical process by which we could modify the reflectivity without also changing the microscopic profile of the inner surface. If the microscopic profile were to change, the effect on the phase would greatly dominate the effect of the reflectivity change.

There is however an effect that can produce an effective change in reflectivity without altering the surface, which is gas absorption. If the gas present in the integrating sphere absorbs light, the intensity of a light ray will decrease along its propagation path, in addition to the absorption that comes with each reflection. According to the Beer-Lambert law, the absorption would take the form of a factor $\exp(-\alpha z)$, with α the absorption coefficient. Using this, we find that the effect of absorption is equivalent to taking $\rho' = \rho \exp(-\alpha \overline{z})$ in (3.27), with $\overline{z}$ the average

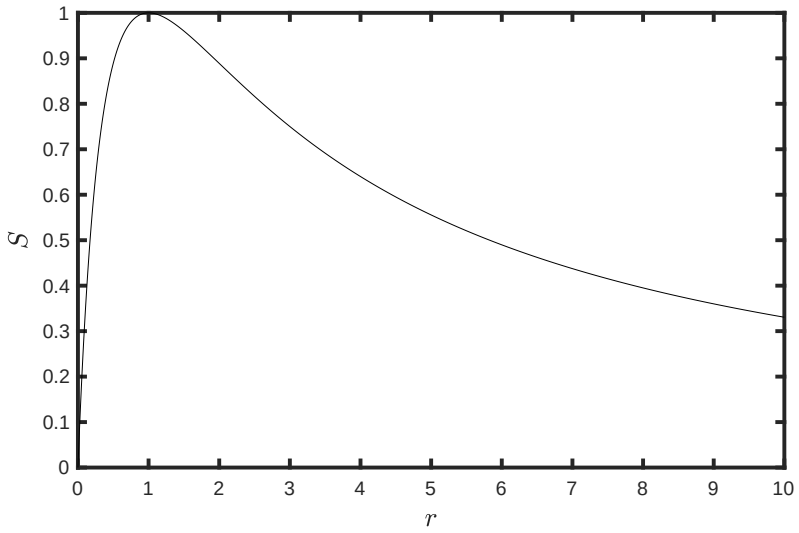

Figure 3.5: Similarity as a function of reflectivity change, as a function of a multiplicative (or dividing) factor r applied to the absorptance.

distance in the sphere, neglecting the variance of z. The similarity is then

$$S = \frac{1 - \dfrac{\alpha\overline{z}}{\log\rho}}{\left(1 - \dfrac{\alpha\overline{z}}{2\log\rho}\right)^2}. \tag{3.30}$$

The effect of absorption in integrating spheres was studied in [43], where the change in output power was measured, instead of a change in the speckle. The ratio of the power before (P_0) and after (P) introducing an absorbent gas in the sphere was found to be

$$\frac{P}{P_0} = \frac{1}{1 - \dfrac{\alpha\overline{z}}{\log\rho}}. \tag{3.31}$$

The graphs of (3.30) and (3.31) are shown in Fig. 3.6 for comparison. We can see that the output power varies more strongly than the similarity, and presents a non-zero gradient at zero. This indicates that, in a metrological perspective, output power may be a better tool for measuring small absorption variations than speckle similarity. This is mainly for the fact that for small absorption variations, the response of the output power is linear, while the similarity only varies at second order. The presence of a zero derivative at zero is an intrinsic feature of the similarity, that we will encounter again at several occasions.

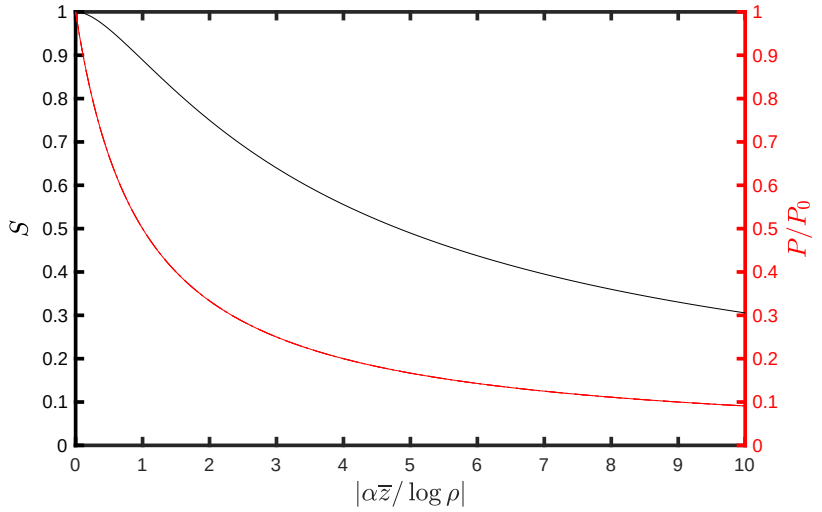

Figure 3.6: Comparison of the similarity change and fractional output power change as a function of gas absorption in the sphere.

2. A change in polarisation

Consider a hypothetical experiment where a speckle would be recorded before and after a transformation that changes the polarisation of light along its propagation in the sphere. The field coming from path p before and after the transformation would be $\boldsymbol{E}_p = \sqrt{I_p}\, e^{i\varphi_p}\boldsymbol{u}_p$ and $\boldsymbol{E}'_p = \sqrt{I_p}\, e^{i\varphi_p}\boldsymbol{u}'_p$, with the change happening only in the Jones vector. Inserting this in (3.6) we have

$$S = \left| \frac{\sum_p P_p \boldsymbol{u}_p^\dagger \boldsymbol{u}'_p}{\sum_p P_p} \right|^2 , \tag{3.32}$$

which is the polarisation version of Eq. (3.9). Now we need to describe the evolution of the Jones vector along the propagation from that of the incident beam ($\boldsymbol{u}$) to its final state ($\boldsymbol{u}_p$ and $\boldsymbol{u}'_p$). The first thing that affects the Jones vector is the reflections along the path. We can describe the effect of each reflection with an operator $\mathcal{R}$ (for reflection). When the transformation is applied, an additional polarisation change takes place along propagation, between each reflection. We can describe this effect with an operator $\mathbb{J}$ (for Jones). With this, we can express the Jones vectors as

$$\boldsymbol{u}_p = \mathcal{R}_N \ldots \mathcal{R}_2 \mathcal{R}_1 \boldsymbol{u} \tag{3.33}$$

$$\boldsymbol{u}'_p = \mathbb{J}_N \mathcal{R}_N \ldots \mathbb{J}_2 \mathcal{R}_2 \mathbb{J}_1 \mathcal{R}_1 \boldsymbol{u}. \tag{3.34}$$

The Jones vector after transformation $\boldsymbol{u}'_p$ is obtained by inserting one $\mathbb{J}$ operator between each pair of reflections (the choice of inserting one at the end or at the start matters little). The $\mathcal{R}$ and $\mathbb{J}$ operators also have a p dependence but we omit it for clarity. Using the same decomposition as in Eq. (3.11), we have

$$S = \left| \frac{\sum_N \rho^N \boldsymbol{u}^\dagger \left(\overline{\mathcal{R}_1^\dagger \mathcal{R}_2^\dagger \dots \mathcal{R}_N^\dagger \mathbb{J}_N \mathcal{R}_N \dots \mathbb{J}_2 \mathcal{R}_2 \mathbb{J}_1 \mathcal{R}_1} \right) \boldsymbol{u}}{\sum_N \rho^N} \right|^2, \tag{3.35}$$

where the bar denotes averaging over all paths containing N reflections. How can we simplify this? Both the $\mathcal{R}$ and $\mathbb{J}$ operators are unitary, as they do not change the amplitude of the light, therefore we have $\mathcal{R}^\dagger \mathcal{R} = \mathbb{1}$ and $\mathbb{J}^\dagger \mathbb{J} = \mathbb{1}$. We can be very tempted to rearrange the operators so as to annihilate all the $\mathcal{R}$ operators by pairs, but this is not possible, as they do not commute. However, the final result for S should not depend on the $\mathcal{R}$ operators neither on the initial Jones vector $\boldsymbol{u}$, but only on the properties of $\mathbb{J}$. One step towards a possible solution is to notice that averaging over all paths containing N reflections can be split into averaging over each successive chord, as all chords are independent. The term in parenthesis can be recast as

$$\left(\overline{\mathcal{R}_1^\dagger \dots \overline{\mathcal{R}_{N-1}^\dagger \overline{\mathcal{R}_N^\dagger \mathbb{J}_N \mathcal{R}_N} \mathbb{J}_{N-1} \mathcal{R}_{N-1}} \dots \mathbb{J}_1 \mathcal{R}_1} \right), \tag{3.36}$$

where each bar denotes averaging over one chord. From this we see that if the central block can be simplified to a matrix proportional to $\mathbb{1}$, with a proportionality constant depending on the statistics of $\mathbb{J}$, then the whole edifice would collapse iteratively and give an expression depending only on the statistics of $\mathbb{J}$. Whether this is the case or not however must depend on the particular transformation considered, and we cannot make any general statement at this point.

An example of such transformation is the Faraday effect. The Faraday effect is a rotation of the polarisation occurring when light propagates in a medium in the presence of a magnetic field. This rotation is proportional to the length of propagation, and to the component of the magnetic field along the direction of propagation. We could not investigate however if the Jones matrix of the Faraday effect has the property $\overline{\mathcal{R}^\dagger \mathbb{J} \mathcal{R}} \propto \mathbb{1}$, by lack of time.

3. The Aharonov-Bohm effect

To finish this section, we return to the case of phase change, but this time we consider a very peculiar sort of phase, the one found in the Aharonov-Bohm effect. This is a quantum mechanical effect encountered in electron waves [50, Section 15.5]. Here we leave the realm of light to explore a different kind of wave, which is permissible as the model we developed in section 3.2 is independent of the nature of the wave, and we are free to consider any effect found in other types of waves.

Let us give a short review of the Aharonov-Bohm effect before turning to its speckle version. Consider an electron wave propagating along a certain path p and ending its journey with a certain arrival phase. If we now turn on electric currents such that a vector potential $\boldsymbol{A}$ is produced, the wave acquires an additional phase given by

$$\phi_p = \frac{q}{\hbar} \int_p \boldsymbol{A} \cdot \mathrm{d}\boldsymbol{l}, \tag{3.37}$$

where q is the electron's charge, $\hbar$ the reduced Planck's constant, and $\mathrm{d}\boldsymbol{l}$ the elementary displacement vector along path p.

The Aharonov-Bohm effect arises when considering this phase in the arrangement shown in Fig. 3.7. An electron wave is shone on a screen with two narrow slits, producing a familiar interference pattern in the far field. We now add a source of vector potential, which is a thin solenoid placed between the slits after the screen. When the solenoid is turned on, the wave acquires the additional phase (3.37). One way to determine the effect this has on the final interference pattern is to compute the difference between the phase acquired by the wave coming from the top slit (path p_1) and the bottom slit (path p_2). This difference is given by

$$\phi_{p_2} - \phi_{p_1} = \frac{q}{\hbar} \int_{p_2} \boldsymbol{A} \cdot \mathrm{d}\boldsymbol{l} - \frac{q}{\hbar} \int_{p_1} \boldsymbol{A} \cdot \mathrm{d}\boldsymbol{l} \tag{3.38}$$

$$= \frac{q}{\hbar} \oint \boldsymbol{A} \cdot \mathrm{d}\boldsymbol{l}. \tag{3.39}$$

Taking the difference has the advantage of "closing the integral" of the vector potential, which can be simplified using the Stokes theorem:

$$\phi_{p_2} - \phi_{p_1} = \frac{q}{\hbar} \Phi, \tag{3.40}$$

with Φ the flux of the magnetic field through the loop formed by the two paths. It follows that the resulting effect is a global shifting of the interference fringes, because the relative phase between the two paths is changed by the amount given by (3.40), which is constant across the observation screen.

The peculiarity of this effect is that the magnetic field outside a solenoid is zero (or at least can be made arbitrarily small), while the vector potential is non-zero. This means that the electrons are influenced by the vector potential, and not the magnetic field. This is often cited to discuss what is most physically fundamental between the magnetic field and the vector potential. Quantum mechanics tells us that the vector potential is more fundamental, as particles can feel it even where there is no magnetic field, while in classical electromagnetism the vector potential is considered as a mathematical convenience with no physical reality. The same discussion exists between the electric field and the electric potential.

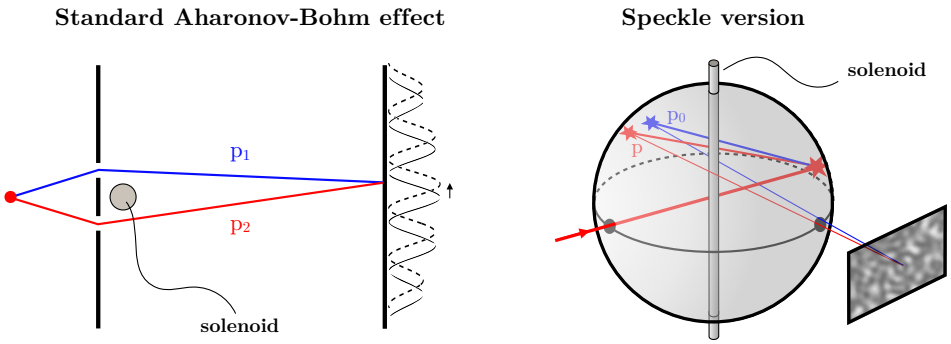

Figure 3.7: Left: in the Aharonov-Bohm effect, an electron wave is shone on two narrow slits, which produces an interference pattern. A thin solenoid is placed between the two slits, which generates a vector potential around it, although the magnetic field outside the solenoid is zero. This introduces a phase shift to the different wave paths and results in a shift of the interference fringes. Right: we imagine a speckle version where an electron wave speckle is produced after multiple reflection in a spherical cavity, with a thin solenoid along one diameter of the sphere (its orientation is arbitrary). The effect of the vector potential is now a structural change of the (electron wave) speckle.

Let us now imagine a speckle version of this arrangement, as shown in Fig. 3.7. We consider the geometry of the integrating sphere, which is now made of a surface that reflects electron waves with a Lambertian reflectance. We also introduce a thin solenoid along one diameter of the sphere. We ask now: what is the similarity profile of the resulting electron wave speckle pattern as a function of the magnetic flux Φ? To answer this, we might want to use directly Eq. (3.37), and find its mean and variance, as we did in section 3.3. However, this promises to be a dreadful exercise. Instead, we can use again the trick of "closing the integral", by subtracting the phase of a reference path p_0. This is allowed as, looking back at Eq. (3.9), we see that S in invariant under a constant phase shift applied to all the paths. We can

write this formally as:

$$S = \left| \frac{\sum_p P_p e^{i\phi_p}}{\sum_p P_p} \right|^2 = \left| \frac{\sum_p P_p e^{i(\phi_p - \phi_{p_0})}}{\sum_p P_p} \right|^2 , \tag{3.41}$$

with ϕ_{p_0} the phase on the reference path p_0. As ϕ_{p_0} is a constant, this is equivalent to multiplying the whole numerator by a phase factor $\exp(-i\phi_{p_0})$, which does not change S because of the absolute square. By taking p_0 as a path that does not make any winding around the solenoid (say, the shortest path), we have

$$\phi_p - \phi_{p_0} = m\frac{q}{\hbar}\Phi, \tag{3.42}$$

with m the number of windings of path p around the solenoid. We can model m by expressing the total angle formed by the path around the solenoid as $\sum_{n=1}^{N} \theta_n$, with N the number of reflections in the path, and θ_n the nth angular step around the solenoid. Each θ_n is uniformly distributed on $[-\pi, \pi]$ by symmetry. We can then approximate m by

$$m = \frac{1}{2\pi} \sum_{n=1}^{N} \theta_n, \tag{3.43}$$

which has mean 0 and variance $N/12$. The mean and variance of the phase associated with one single pass are then given by

$$\mu = 0 \qquad \sigma^2 = \frac{q^2}{12\hbar^2}\Phi^2. \tag{3.44}$$

Inserting this in (3.14), we find the similarity profile

$$S = \frac{1}{\left(1 - \dfrac{q^2}{24\,\hbar^2 \ln \rho}\Phi^2\right)^2} . \tag{3.45}$$

We find again a square Lorentzian, as in the case of transverse displacement (see section 3.3 and Chapter 3), which is another effect with $\mu = 0$.

Beyond the mere curiosity, this thought experiment might find some use in the investigation of the Aharonov-Bohm effect. Indeed the Aharonov-Bohm effect is notoriously difficult to measure, given the short wavelength of electron waves, which imposes very close slits and therefore very small solenoids. The setup imagined here might relax this constraint. Note that the similarity profile is independent of the size of the sphere, therefore miniaturised versions of this arrangement are possible,

which might mitigate against the possibly limited coherence length of the electron wave. A gain in sensitivity could also be obtained if high values of ρ are achievable. The feasibility of a spherical cavity with a Lambertian reflectance to electron waves should also be explored.

3.7 Heating effect

We finish this chapter with a particular effect encountered in practice when using integrating spheres. When the speckle pattern produced by an integrating sphere is recorded on a long period of time, without applying any transformation and using a continuous illumination at a fixed power, we observe a slow change of the speckle. When quantifying this change using the similarity, we obtain a curve which is very well fitted by a Lorentzian profile of the form

$$S(t) = \frac{1}{1 + \left(\frac{t}{t_0}\right)^2}, \tag{3.46}$$

with t_0 an empirical parameter corresponding to the HWHM of the curve. An example of obtained similarity profile is shown in Fig. 3.8, with the experimental parameters of section 2.4.

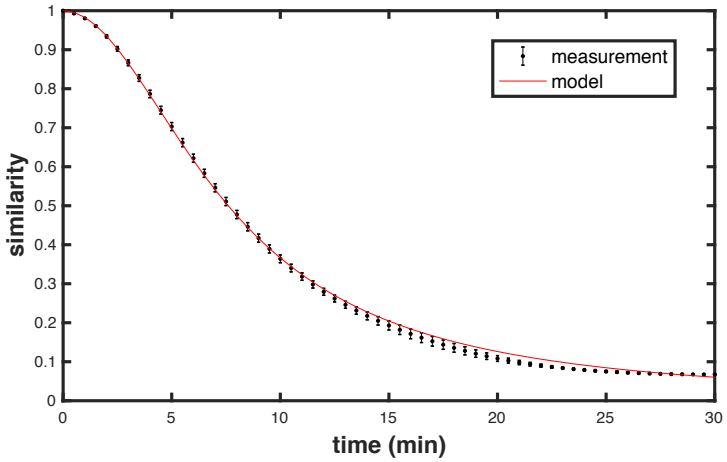

Figure 3.8: Similarity of the speckle pattern produced by an integrating sphere over time, with no transformation applied. Black: measured similarity. Red: Lorentzian fit with a HWHM of 7.6 min.

The fact that the similarity profile can be fitted by a Lorentzian suggests that this effect is not due to random perturbations but follows from a simple underlying process. One hypothesis that may explain this observation is heating due to the input laser power. Let us explore this idea.

When the laser first hits the inner surface of the sphere, a power $(1-\rho)P$ is absorbed in the region of the laser spot (with P the power of the laser), and the remaining power ρP is absorbed uniformly on the rest of the inner surface. With the sphere most commonly used in this thesis, this represents 8% of power absorbed on the laser spot and 92% on the rest of the inner surface. The resulting temperature increase, in the surface coating, can then either diffuse to the sphere's material or to the air contained inside the sphere.

In the case of the material, an order of magnitude estimation shows that the temperature diffusion time is very short (of the order of seconds). We can then neglect the non uniformity of the heating and make the assumption that the temperature increase is uniform throughout the material. A uniform temperature increase implies an isotropic thermal expansion of the sphere. The effect of such an expansion can be found analytically. The phase acquired by light on a given path of length z is kz, with k the wavenumber (assuming that the refractive index of the medium in the sphere is close to 1). The effect of an isotropic expansion is to increase all lengths by the same factor which, when expressed in terms of the sphere's radius R, is given by $\Delta R/R$, with ΔR the variation of radius resulting from the expansion. The average phase shift on a chord is then $\mu = 4k\Delta R/3$. Assuming in a first approximation that the heat remains stored in the sphere's material, the temperature increases linearly with time, and so does the radius of the sphere. We then have $\mu \propto t$, which inserted in (3.14) leads indeed to a Lorentzian profile in time.

We could expect that the increase in temperature of the sphere's material in turn induces a heat flux from the sphere to the surrounding air, leading to thermal equilibrium and stopping the thermal expansion. However we observed that t_0 does not change significantly in a period of 80 minutes, meaning that no thermal equilibrium is reached in that time. This indicates that the approximation of the heat remaining in the sphere's material is valid in that time scale.

From the value of t_0 in Fig. 3.8, we can infer the rate of change of the radius. After a time equal to t_0, we have the relation $\mu = \ln \rho$. Using $\mu = 4k\Delta R/3$, we can infer that the radius of the sphere increases by 8.1 nm every 7.6 minutes by thermal expansion, which corresponds to a speed of 1.1 nm.min^{-1} or 18 pm.s^{-1}. From these values of thermal expansion we can infer the temperature increase via the coefficient of thermal expansion of aluminium $\Delta T = \Delta R/(R\alpha)$. We find that the temperature increases by 30 mK after a time t_0, or 4 mK per minute, and 70 µK per second.

In the case of heating of the air, we cannot infer a simple law for the similarity, as the temperature increase would most certainly not be uniform throughout the volume of the sphere, and the corresponding phase could not be expressed in a

simple way. However, as we do observe a Lorentzian, the fraction of heat going into the air must be small compared to that going into the material. This fraction must depend on the properties of the material constituting the sphere, in particular its thermal conductivity. As the thermal conductivity of aluminium is about 4 orders of magnitude higher than that of air, it is reasonable to think that most of the heat is transferred to the material.

In order to further confirm the hypothesis that the slow change in the speckle is due to heating from the laser, we measure t_0 for different powers of the input beam. Assuming again that the heat remains stored in the sphere's material, we expect the inverse of t_0 to be proportional to the input power. For each value of power, we record the speckle patterns for 5 minutes, and extract t_0 by fitting with a Lorentzian profile. The result is shown in Fig. 3.9, where the uncertainty on the estimation of $1/t_0$ is also shown as an error bar. We find an approximately linear relation reading $1/t_0 = 0.012P$, with t_0 in minutes and P in milliwatts. From this we can infer the rate of change of the radius to be $0.1\,\mathrm{nm\,min^{-1}\,mW^{-1}}$

We can compare the value of the coefficient found in Fig. 3.9 to what we would expect based on the knowledge of the physical properties of the sphere. We find that $1/t_0$ is related to the input power P via

$$\frac{1}{t_0} = \left(\frac{4k\alpha R}{3C\ln\rho}\right) P, \tag{3.47}$$

with α the coefficient of thermal expansion of the sphere, and C its heat capacity (the other quantities have been defined above). This is found by inserting $\mu = 4k\Delta R/3$ in Eq. 3.14, assuming $\Delta R/R = \alpha\Delta T$ and $Pt = C\Delta T$, and identifying t_0 when expressing the result in the form of Eq. 3.46. The quantity in parenthesis corresponds to the coefficient found in Fig. 3.9. Using the thermal expansion coefficient of aluminium ($\alpha = 23 \times 10^{-6}\mathrm{K}^{-1}$) and estimating the heat capacity of the sphere from its mass (50.8 g) and the specific heat capacity of aluminium ($0.89\,\mathrm{J\,K^{-1}\,g^{-1}}$), we find the value $0.048\ \mathrm{min^{-1}\,mW^{-1}}$, which is 4 times higher than the observed value. This means that the sphere expands 4 times less than expected based on our calculation. This may be due to the fact that the sphere is in direct contact with its support, which must absorb some of the heat and result in a higher effective heat capacity.

This effect is of importance when using the integrating sphere as a measurement tool. It introduces a constant drift in the signal, and we will see in Chapters 5 and 6 how to mitigate for this, either via data processing, or by physically compensating the effect in real time. On the other hand, the observed high sensitivity brings

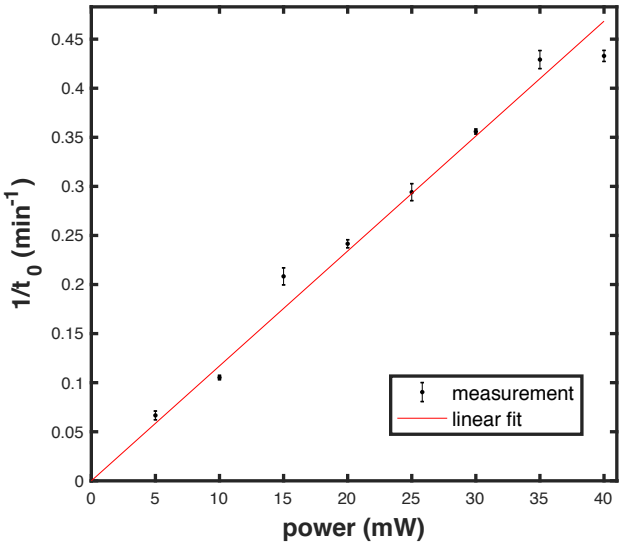

Figure 3.9: Effect of laser power on the rate of change of the speckle pattern. The inverse of the decay time is shown as a function of the input power. We find an approximately linear relation with a proportionality constant of $0.012\,\mathrm{min}^{-1}\,\mathrm{mW}^{-1}$, which supports the heating-related origin of the effect.

promises for the measurement of small temperature measurements, although this is not explored in this thesis.

3.8 Conclusion

In this chapter, we performed a theoretical study of the speckle patterns produced by an integrating sphere. We developed a model that predicts the change in the speckle pattern, quantified by the similarity (3.1), resulting from an arbitrary transformation. A transformation is any effect that can change either the intensity, phase, or polarisation of light along its propagation in the sphere. We paid particular attention to the case of the phase, which happens to describe all the effects that are experimentally studied in this thesis. In this particular case, we found a general expression (Eq. (3.14)) that predicts the resulting similarity. This expression depends on the reflectivity of the sphere, and two statistical quantities characterising the transformation: the average and variance of the phase shift that the transformation applies to the light on a given chord.

We also considered effects that change the two other properties of light, intensity and polarisation. We could solve the case of intensity (Eq. (3.27)), however the polarisation case was found to be more subtle and case-dependent, and we could not arrive at an equivalent general result, although we can comfort ourselves with the pleasing mathematics that we encountered on the way. The derivations outlined

there may serve as a basis for future work on this topic.

We also discussed experimental aspects involved in the use of integrating spheres, in particular the heating effect. The different approaches taken to tackle this effect will be discussed in Chapters 5 and 6.

Chapter 4

Speckle and wavelength variation

The work presented in this chapter was published in [32].

List of symbols and abbreviations

S	speckle similarity (Pearson correlation coefficient of intensity)
μ	average phase variation of the field on a chord
σ	standard deviation of the phase variation of the field on a chord
k	wavenumber
z	length of a path
HWHM	half width at half maximum
R, ρ	radius and reflectivity of the integrating sphere
λ	wavelength of light
L	fibre length
NA	numerical aperture

4.1 Introduction

In this chapter, we shall use the case of wavelength variation as a first validation of our model developed in Chapter 3.

When the wavelength of laser light incident in an integrating sphere varies by a small amount, the resulting speckle pattern changes, and in a remarkably sensitive way. To build an intuition of why speckle depends on wavelength, consider a set of light rays taking different paths through the sphere. Wavelength determines the distance between two points of equal phase (modulo 2π) along the propagation of a light ray. If we mentally place a dot at every repeating value of the phase, a light ray is a succession of dots separated by one wavelength. If we now change the

wavelength, we apply a global dilation of the dots along the ray paths. This dilation affects each ray differently, depending on its length, and therefore the interference of the different rays (i.e. the speckle pattern) changes.

This principle can be exploited in a metrological perspective to measure wavelength variations. The ability to measure small wavelength variations is essential in areas of science and engineering where wavelength stability is required, such as laser cooling of atoms and ions [51]. A number of speckle-based methods have been developed in that purpose for their low cost, simplicity of implementation, and their possibility of miniaturisation. These method use either a rough surface or optical fibres, reaching a resolution at the picometer level [52, 53], femtometer level [39,40,42,54,55], and even attometer level [41,56]. The most common methods used either rely on the similarity between the speckle pattern before and after the wavelength change, Principal Component Analysis, or machine learning.

The similarity as a function of wavelength change is known in the case of a rough surface [57], and its HWHM can be estimated analytically in the case of a multimode fibre [58]. However, such a theoretical description is missing for the integrating sphere, which has only recently been introduced in this field [39–42].

The sensitivity of speckle patterns to wavelength is also important in a different but related topic, which is speckle-based spectrometry [24, 25, 54, 59–63], where the spectral resolution is limited to the HWHM of the similarity profile.

Here we will focus on validating our model in the case of wavelength variation, which by the same occasion will give us the explicit relationship between the width of the similarity profile and the relevant experimental parameters, which is currently missing in the literature.

4.2 Similarity profile

Let us first determine the similarity profile by applying Eq. (3.14). To that purpose, we need to compute the phase shift ϕ introduced on a given chord by the wavelength change. We then compute the average and variance of ϕ to deduce μ and σ^2 respectively. We find ϕ in the following way. On a given path of length z, light acquires a phase $k\,z$, with k the wavenumber (assuming a refractive index equal to one). After a wavelength change, the phase changes by an amount $\Delta k\,z$. It follows that the average phase change on a chord is $\mu = \Delta k\,\overline{z}$, with $\overline{z}$ the average chord length in the sphere, which is given by geometry to be $4R/3$ (with R the sphere's radius) [46–48]. Likewise, the standard deviation of chord length is $\sqrt{2}R/3$ [47, 48].

This gives

$$\mu = \frac{4}{3} R\Delta k \qquad \sigma = \frac{\sqrt{2}}{3} R\Delta k. \tag{4.1}$$

Inserting these expressions in (3.14), and using $\Delta k = -k\Delta\lambda/\lambda$ (as $k = 2\pi/\lambda$ and Δk small), we have

$$S = \frac{1}{1 + \left(\dfrac{\Delta\lambda}{\Delta\lambda_0}\right)^2}, \tag{4.2}$$

where we neglected the σ term (see Appendix D), with $\Delta\lambda_0$ given by

$$\Delta\lambda_0 = \frac{3\lambda^2 \left|\ln \rho\right|}{8\pi R}. \tag{4.3}$$

A natural measure of sensitivity, widely used in this thesis, is the HWHM (Half Width at Half Maximum) of the similarity profile, which in the present case is equal to $\Delta\lambda_0$. This short calculation therefore reveals the essential parameters determining sensitivity: the reflectivity, the radius, and secondarily the wavelength. For modest parameters such as $R = 1$ cm, $\rho = 0.9$, and $\lambda = 780$ nm, this gives already a fairly high sensitivity with an HWHM of about 0.8 pm.

4.3 Experimental verification

In order to verify (4.2), we implement the experimental setup shown in Fig. 4.1. Laser light enters an integrating sphere and the resulting speckle pattern is recorded on a camera. The sphere-camera distance is 20 cm, with a laser power of 10 mW (see complementary experimental details in section 2.4). We then apply a linear wavelength variation by applying a triangular modulation to tune the cavity length of the laser. The amplitude of the wavelength variation is 2.9 ± 0.1 pm and is measured using a fibre coupled Fizeau-based wavemeter (HighFinesse WS7). One similarity profile can be extracted by computing the similarity between one reference image and the subsequent images. By using different reference images across the modulation period, we extract several similarity profiles, whose average and standard deviation (displayed as an error bar) is shown in Fig. 4.2(a). As a first sanity check, we fit the resulting profile using (4.2) with ρ as a free parameter, and find the best fit for $\rho = 0.922 \pm 0.002$. The uncertainty comes in equal amount from that of

the wavelength modulation amplitude and the fitting. Note that the heating effect discussed in section 3.7 is not an issue here as the applied wavelength variation takes place in a much shorter interval than the heating time scale.

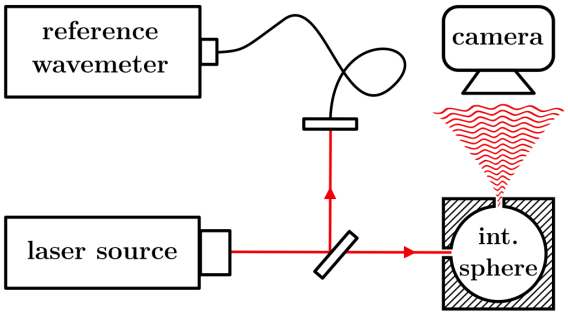

Figure 4.1: Experimental setup. Laser light enters an integrating sphere and produces a speckle pattern recorded on a camera. The wavelength of the laser is then changed in a linear manner, while the resulting speckle change is recorded. The wavelength variation is monitored via a fibre-coupled wavemeter.

To compare to the fitted value, we perform an independent measurement of ρ using a method based on the measurement of the output power at different distances from the sphere, knowing the input power, port size, port-detector distance, detector area, and integrating sphere radius [44]. We find a value of $\rho = 0.918 \pm 0.008$, which is in accordance with our value from fitting the similarity curve of $\rho = 0.922 \pm 0.002$. Here the main sources of uncertainty are the machine precision limit on the output port diameter and the power meter measurement (fractional uncertainties of 3% and 7% respectively). Other sources of systematic error, not taken into account, are the alignment of the detector with the port and the orientation of the detector (both lead to an underestimation of ρ).

The fit in Fig. 4.2(a) confirms the predicted functional form of the similarity profile. Now in order to confirm the expression of the HWHM of the profile (4.3), as a function of reflectivity and radius, we measure the HWHM of four different spheres whose radii are known and reflectivities are measured using the method described above. We show in Fig. 4.2(b) the measured HWHM as a function of the ratio $|\ln \rho| / R$. A linear fit gives a coefficient of $(7.3 \pm 0.3) \times 10^{-14}$ m^2, which is in agreement with the model predicting a value of $3\lambda^2/(8\pi) = 7.26 \times 10^{-14}$ m^2. This is now a complete verification of the model where both the functional form and the parameters of the similarity profile have been confirmed. The properties of the spheres used are given in Table 4.1. Spheres 1 to 3 are custom-made aluminium spheres, manually coated with Spectraflect paint, and sphere 4 is a commercial Spectralon sphere (Thorlabs IS200).

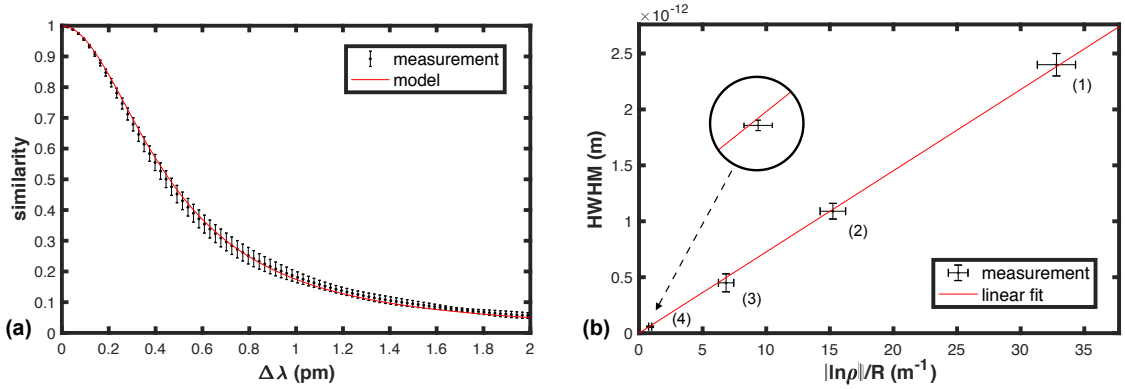

Figure 4.2: (a) Similarity as a function of wavelength change, experimental (black) and Lorentzian profile predicted by model (red), fitted for a reflectivity $\rho = 0.922$. The HWHM is 0.45 pm. (b) HWHM as a function of the ratio $|\ln \rho| / R$ for different spheres, experimental (black) and linear fit (red). Each sphere is labelled and described in Table 4.1.

Sphere number	Radius (mm)	Reflectivity	HWHM (pm)
1	4	0.877±0.005	2.4±0.1
2	7.5	0.892±0.007	1.09±0.07
3	12.5	0.918±0.008	0.45±0.08
4	25.4	0.978±0.003	0.058±0.004

Table 4.1: Properties of the spheres used in Fig. 4.2(b).

We note in passing that the fit of the similarity curve can serve as a means of measuring the reflectivity, with an accuracy only limited by the knowledge of the applied wavelength variation and the sphere's radius.

4.4 Comparison with multimode fibres

Shining laser light through multimode fibres is one of the most widely used way of producing speckles. In this section we compare the sensitivity to wavelength change of the speckles produced in this way to those produced by a sphere. The similarity profile of a multimode fibre is not Lorentzian, but we know the dependence of its HWHM on the relevant fibre parameters, namely $\Delta\lambda_0 \propto \lambda^2/(L\,(NA)^2)$, with λ the wavelength, L the fibre's length, and NA its numerical aperture [24, 58]. It is independent of the core size above a critical diameter of about 100 μm [24]. For a step-index fibre, the relationship was empirically found to be $\Delta\lambda_0 \approx 2.4\,\lambda^2/(L\,(NA)^2)$ [22]. Equating this HWHM to that found above for the integrating sphere, we find a direct proportionality between the fibre's length and the radius of the equivalent integrating sphere. With a standard value of $NA = 0.22$, and the reflectivity of our

commercial sphere $\rho = 0.978$, we have

$$L \approx 19000\, R, \tag{4.4}$$

which means that a sphere of radius R shows the same sensitivity as a fibre of length $19000R$. For example, our sphere of radius 2.54 cm is equivalent to a 500 m long fibre.

This demonstrates that an integrating sphere can offer a very compact alternative to an optical fibre, as the effective space occupied by a fibre is much larger than that of the equivalent integrating sphere (even though its intrinsic volume is smaller) for similar performance. Another advantage of the sphere is that the sensitivity to wavelength change is independent of the way in which light is coupled into the sphere. In contrast, it was shown that the sensitivity of multimode fibres depends strongly on the number of spatial modes excited in the fibre and therefore on the coupling of light at the fibre input [24, 64]. Moreover, an integrating sphere offers the additional advantage of being more robust to mechanical perturbations, as they are monolithic and have no moving parts, which can be a serious difficulty when using fibres.

4.5 Comparison to a Fabry-Pérot interferometer

Fabry-Pérot interferometers are another tool used to measure wavelength variation. Here we discuss their differences with integrating spheres.

As discussed in section 3.5, a strong analogy exists between the Fabry-Pérot interferometer and the integrating sphere. For a Fabry-Pérot of reflectivity ρ and length L, the HWHM of the output intensity as a function of wavelength detuning is $\lambda^2 |\ln \rho| / (4\pi L)$ [65]. For an integrating sphere of reflectivity ρ and diameter equal to L ($L = 2R$), we found that the HWHM of the similarity profile as a function of wavelength change is $3\lambda^2 \left|\ln \rho\right| / (8\pi R)$. The HWHM of the Fabry-Pérot is exactly 3 times smaller. This factor of 3 comes down to the different average path-length in each case, which is actually shorter in the sphere (there is only one path in the Fabry-Pérot, which is the round-trip between the two mirrors).

In terms of sensitivity to wavelength variation, both approaches are comparable, although larger sizes and higher reflectivities may be more easily achievable in the case of the Fabry-Pérot. On the other hand, the integrating sphere benefits from a simpler implementation, as it does not require any alignment and is only made of inexpensive components. In terms of data acquisition, the Fabry-Pérot benefits from a lower noise as it usually implies a photodiode, as opposed to a camera for the

integrating sphere. However in the latter case the implementation is again simpler, as the camera can be placed anywhere in the region illuminated by the output light.

4.6 Conclusion

We applied the model developed in Chapter 3 to the particular case of wavelength variation and predicted the Lorentzian profile (4.2). By doing so, we proved that the relevant parameters that determine the sensitivity of the resulting speckle pattern (defined as the HWHM of the similarity profile) are the surface reflectivity, the radius of the sphere, and the wavelength. We experimentally verified the functional form of the similarity profile, and found very good agreement. We also verified the dependency of the profile on the above-mentioned parameters, which were all independently measured, and found again a very good agreement. This constitutes a complete verification of the model with no free parameter, in the particular case of wavelength variation.

We found that the approach taken here can be used in reverse, to measure the reflectivity of the inner surface by measuring the HWHM of the similarity curve, knowing the radius and wavelength. The uncertainty on the reflectivity in that case is mainly limited by that of the applied wavelength variation. This provides a simple and accurate way of measuring reflectivity, although limited to the particular wavelength of the laser used.

Beyond the original purpose of verifying our model, the explicit expression of the HWHM as a function of the relevant parameters is of importance for the field of speckle-based measurement of wavelength variations and spectra. For the former, because resolution depends directly on the speckle's sensitivity to wavelength variation. For the latter, because the HWHM of the similarity profile gives the spectral resolution.

We also proved that an integrating sphere of radius R gives the same sensitivity to wavelength change as a fibre of length $\approx 19000R$, with standard parameters. This suggests that the importance of the integrating sphere in the context of wavelength measurement may have been overlooked, as it offers significant advantages over more common alternative methods.

Chapter 5

Measurement of refractive index variations

The work presented in this chapter was published in [66].

List of symbols and abbreviations

n	refractive index
n'	refractivity $(n-1)$
k	wavenumber
z	length of a path in the sphere
λ	wavelength of light
R, ρ	radius and reflectivity of an integrating sphere
S	speckle similarity (Pearson correlation coefficient of intensity)
μ	average phase variation of the field on a chord
σ	standard deviation of the phase variation of the field on a chord
HWHM	half width at half maximum
ρ_{air}	mas density of air
V	volume of the chamber
$\delta n, \sigma_n$	random fluctuation of refractive index and its standard deviation
$\delta\lambda, \sigma_\lambda$	random fluctuation of wavelength and its standard deviation
N	number of pixels in speckle image
t_0	HWHM in time of the similarity profile
T	temperature

5.1 Introduction

In the integrating sphere arrangement, when the refractive index of the medium contained in the sphere varies slightly, a change in the resulting speckle pattern in observed. To build an intuitive picture of why this happens, remember that the refractive index characterises the speed of light in a medium. When it varies, light changes speed, which results in a relative delay between the different paths that reach the camera, depending on the distance they had to travel through the medium. This delay takes the form of a phase, which changes the resulting speckle pattern. This is very analogous to what we had with a wavelength change, even formally, as we shall see in the next section.

Refractive index is a parameter of importance across many areas of optics. For example, high-precision measurements of refractive index have been proposed as a route to a more accurate definition of the Pascal [67]. In optical tweezers experiments exploring the motion of RNA polymerase during transcription [68], the effect of air currents (which typically modulate the refractive index at the order of 10^{-7}) [69,70] caused sufficient position instability of the optical trapping and measurement beams to mask the angstrom-level motion, even in a sealed environment. Also, interferometric measurements of length and displacement in gaseous environments [71] are limited in their accuracy by uncertainties in the refractive index of the environment.

There are many methods to measure refractive index using lasers, including hollow-core [72], photonic crystal [73, 74] or evanescent optical fibre refractometers [75] (fibre-based devices have been recently reviewed in [76]), and metasurface-based refractometers [77]. The most sensitive measurements of refractive index in the literature are variants of double-channel Fabry-Perot cavities [70], with which refractive index uncertainties of 10^{-12} have recently been demonstrated [67].

The first application of speckle in refractometry was presented half a century ago [78,79], and most subsequent work has adopted a similar scheme. A laser beam impinges on a random phase screen to produce a speckle field, which then traverses a medium under investigation, and the changes in the speckle pattern can be used to quantify changes in the refractive index. Speckle has been applied to measurements of the refractive indices of air [80], glass [81], and liquids [82]. The best performance to date reached a 10^{-6} resolution in refractive index variation [83]. This was obtained using the same quantitative tool that we have been using thus-far (the similarity), however the diffusion geometry was three consecutive planar diffusers placed inside a medium of interest.

How might one further optimise the sensitivity of a speckle refractometer? A

speckle pattern is the result of the interference of many different wave paths. When light propagates in a medium of refractive index n, the phase acquired on a given path of length z is $n\,k\,z$, with k the wavenumber. A change in refractive index therefore applies a phase shift $\Delta n\,k\,z$ on that path. Now any change occurring in the speckle pattern results from relative phase changes between paths. It follows that what maximises the sensitivity of the speckle pattern is not path-length itself, as intuition might suggest, but the *spread* in path-length distribution within the medium of interest. In a simple illustrative case where we consider only two given paths, their relative phase changes by $k\Delta n\Delta z$, where we see that the maximal effect is obtained for a maximal path-length difference. This analysis is consistent with what is found in [83], where the succession of planar diffusers inside the medium increases the number of paths and their length differences. However, that approach is still limited by the globally paraxial geometry of the diffusion.

In this chapter, we further increase the speckle sensitivity by using the integrating sphere, which naturally presents a broad distribution of path-length. This offers orders of magnitude improvement in sensitivity compared with previous speckle-based techniques. The method relies on the measurement of the similarity, from which the refractive index change is inferred using an explicit relation, that we derive analytically and verify experimentally. By varying the pressure of air inside an integrating sphere, we resolve changes in refractive index as low as 4.5×10^{-9} with an uncertainty of 7×10^{-10}. We also discuss the role of the heating effect and identify strategies for its compensation.

5.2 Similarity profile

We first want to determine the similarity profile as a function of refractive index change by applying Eq. (3.14). In that purpose, we first need to express the phase shift on a given chord. On a given chord of length z, light acquires a phase $n\,k\,z$, with n the refractive index and k the wavenumber. After a refractive index change, the phase changes by an amount $\Delta n\,k\,z$. It follows that the average phase change on a chord is $\mu = \Delta n\,k\,\overline{z}$, with $\overline{z}$ the average chord length in the sphere, which is given by geometry to be $4R/3$ (with R the sphere's radius) [46–48]. Likewise, the standard deviation of chord length is $\sqrt{2}R/3$ [47, 48].

This gives

$$\mu = \frac{4}{3}\Delta n\, k\, R \qquad \sigma = \frac{\sqrt{2}}{3}\Delta n\, k\, R. \tag{5.1}$$

Inserting this in Eq. (3.14), we have

$$S = \frac{1}{1 + \left(\dfrac{\Delta n}{\Delta n_0}\right)^2}, \tag{5.2}$$

where the σ term is neglected (see Appendix D), with Δn_0 is given by

$$\Delta n_0 = \frac{3\lambda\,|\ln \rho|}{8\pi R}, \tag{5.3}$$

which also corresponds to the HWHM of the Lorentzian. For modest parameters such as $R = 1$ cm, $\rho = 0.9$, and $\lambda = 780$ nm, this gives $\Delta n_0 \approx 10^{-6}$.

The knowledge of the similarity profile allows us to infer the refractive index variation between two given times, by simply applying the reciprocal function of Eq. (5.2) and using the value of the similarity between the two corresponding speckles. This gives

$$\Delta n = \Delta n_0 \sqrt{1/S - 1}, \tag{5.4}$$

with S the similarity between the two corresponding speckles.

5.3 Experimental implementation

In this section we experimentally verify relation (5.2) with the setup described in Fig. 5.1. Laser light enters an integrating sphere and the resulting speckle pattern is recorded on a camera. The sphere-camera distance is 20 cm, with a laser power of 10 mW (see complementary experimental details in section 2.4). The sphere is placed in a 2490 ± 50 ml stainless steel chamber which is hermetically sealed using ConFlat flanges and copper gaskets (these are standard vacuum technology). A refractive index variation is then applied by slightly compressing the air inside the chamber using a 100 ml syringe connected to the chamber via a needle valve. The compression changes the density of the air, which increases its refractive index in the same proportion. The syringe is compressed at a constant rate of 4.0 $\mathrm{ml\,s^{-1}}$ using a motorised translating stage while the changing speckle is recorded. From

this we extract the similarity profile as a function of refractive index change shown in Fig. 5.2. The variability of the profile, given by the error bars, is found in the same way as described in section 4.3.

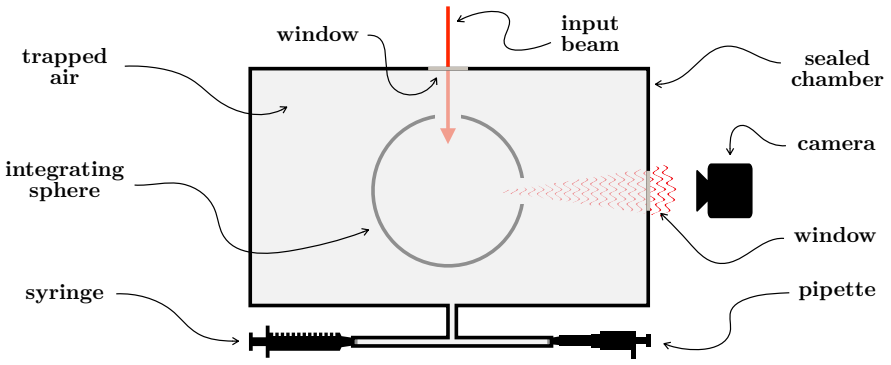

Figure 5.1: Experimental setup. An integrating sphere is placed in a sealed chamber, which light can enter and exit via two glass windows. The air inside the chamber is slightly compressed by pushing a syringe (for the verification of Eq. (5.2)) or a pipette (for the measurement of small variations). The resulting change in refractive index of the air induces a change in the speckle pattern which is recorded on a camera.

The value of the refractive index change is inferred from the volume change by the following. The fact that the chamber is sealed implies $\Delta n/n' = \Delta\rho_{\text{air}}/\rho_{\text{air}} \approx -\Delta V/V$, with $n = 1 + n'$ the refractive index of the air inside the chamber, ρ_{air} its density, and V the chamber's volume, assuming $n' \propto \rho_{\text{air}}$ (this is called the Gladstone-Dale law [84]) and $\Delta V \ll V$. It follows that the refractive index change is given by $\Delta n = -n'\Delta V/V$, with $n' = 2.7 \times 10^{-4}$ for our values of $\lambda = 780$ nm, 20°C, and 100.5 kPa [85]. The main source of uncertainty is the volume of the chamber (2%). By fitting the resulting profile using (5.2) with the reflectivity as a free parameter, we find best agreement for $\rho = 0.916 \pm 0.002$, which is consistent with our previous estimate $\rho = 0.918 \pm 0.008$ in section 4.3. The measured HWHM is $\Delta n_0 = 6.5 \times 10^{-7}$, corresponding to a volume variation of only 6.0 ml, or a fractional volume change of 0.24%. This can be done very easily by hand without feeling any pressure resistance, which offers a very hands-on demonstration of speckle sensitivity.

5.4 Measurement of small refractive index changes

How can we measure refractive index variations much smaller than Δn_0? We could simply apply (5.4), however this is not ideal, as for $\Delta n \approx 0$ we have $dS/d\Delta n \approx 0$. A variation much smaller than Δn_0 would take place "at the top of the hill", where S varies only at second order in Δn. This problem would be solved if instead

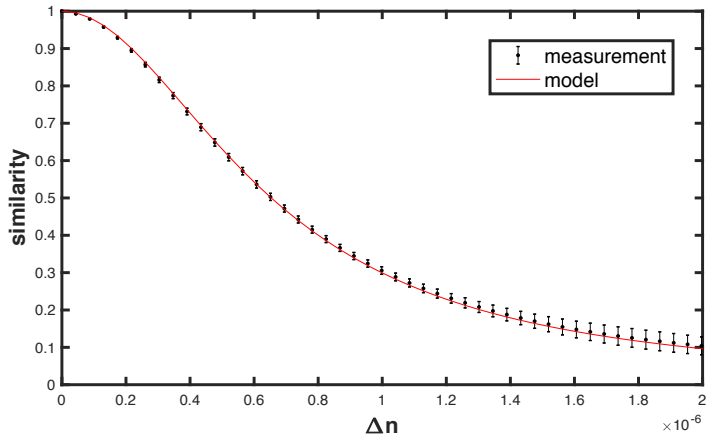

Figure 5.2: Speckle similarity as a function of refractive index change, experimental (black dots) and Lorentzian profile predicted by model (red line), fitted for a reflectivity $\rho = 0.916$. The centre and span of the error bars respectively give the mean and standard deviation of a set of curves extracted from the data set. The HWHM is 6.5×10^{-7}.

we could look at small variations of the similarity around a point of higher slope, anywhere along the profile other than $\Delta n = 0$. This in fact can be done by purposely applying an initial variation prior to the measurement, for example equal to Δn_0. In this way the similarity, taken between a speckle before and after the initial Δn_0 leap using (5.4), varies around a value of 0.5 with a high sensitivity. In our setup, this initial variation could be applied by changing the volume of the chamber by 6.0 ml. However, a simpler way is to make use of the equivalence that exists between refractive index change and wavelength change, and use a wavelength change instead. Indeed, all the effects that are dominated by the μ term in Table 3.2 can be used interchangeably to produce the same change in the final speckle pattern. Let us see that in the case of refractive index change and wavelength change. The phase shift resulting from a wavelength change on a path of length z is $n\,\Delta k\,z$, which is of the same form as what we found for a refractive index change ($\Delta n\,k\,z$). As both phase shifts are proportional to z, equating them on one path equates them on all paths, and the two effects are physically equivalent when $\Delta n = n\Delta k/k \approx -\Delta\lambda/\lambda$ (with $n \approx 1$ and $\Delta\lambda$ small). This means that the same change in a speckle pattern occurs after a refractive index change Δn or after a wavelength change $\Delta\lambda = -\lambda\Delta n$. We can therefore bring the similarity to a point of higher slope by applying an appropriate wavelength offset (of the order of 0.5 pm). Note that the actual value of the initial offset needs not be known, it can we seen as an arbitrary parameter that we tweak such that the similarity is close to 0.5. In our setup, this corresponds to about 0.5 pm.

We proceed in the following way. A reference speckle pattern is first recorded

at an initial wavelength, and the initial wavelength offset is applied. Thereafter, small refractive index changes are applied using a pipette, which can apply much smaller volume changes than a syringe. We press and release the pipette in a square wave manner with a period of about a second, with a 40 μl volume load. This corresponds to a fractional volume change of $(1.61 \pm 0.03) \times 10^{-5}$, from which we infer an expected refractive index change of $(4.3 \pm 0.1) \times 10^{-9}$. We compute the similarity between the reference speckle and the speckles undergoing change, which is then converted to refractive index difference using (5.4). The resulting curve is shown in Fig. 5.3. The first value of the time series is subtracted, so that what is displayed is the refractive index variation applied by the pipette. We find steps of amplitude $(4.5 \pm 0.7) \times 10^{-9}$, which is consistent with the expected value.

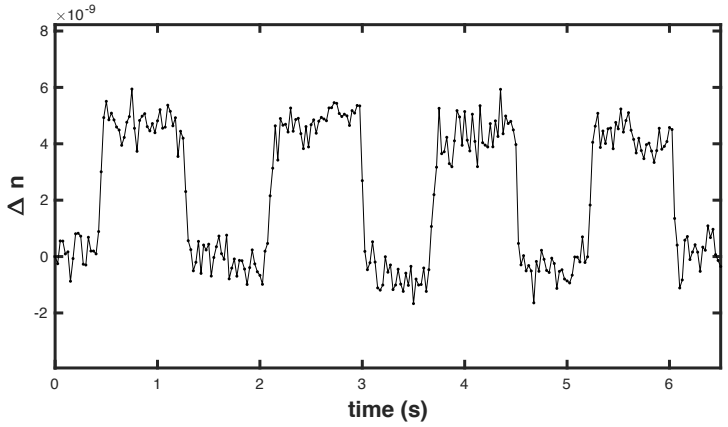

Figure 5.3: Measurement of small periodic steps in refractive index, applied by changing the volume of the chamber by 40 μl using a pipette, corresponding to a fractional volume change of $(1.61 \pm 0.03) \times 10^{-5}$. We find a step amplitude of $(4.5 \pm 0.7) \times 10^{-9}$, in accord with the expected value of $(4.3 \pm 0.1) \times 10^{-9}$.

5.5 Uncertainty

As the slope of the similarity profile at $\Delta n = \Delta n_0$ is $1/(2\Delta n_0)$, we can express any small refractive index variation around Δn_0 as $\delta n = 2\Delta n_0 \delta S$. For estimating our measurement uncertainty, we also include laser wavelength fluctuations, as this sets a fundamental limit to performance. We now have

$$\delta n = 2\Delta n_0 \delta S - \frac{\delta \lambda}{\lambda}, \tag{5.5}$$

where we used the fact described above that a refractive index variation contributes to speckle change in the same way as a wavelength variation, with the equivalence

given by $\Delta n = -\Delta\lambda/\lambda$. From this we infer the uncertainty relation

$$\sigma_n^2 = (2\Delta n_0 \sigma_S)^2 + \left(\frac{\sigma_\lambda}{\lambda}\right)^2, \tag{5.6}$$

where σ denotes the uncertainty (standard deviation of the noise) on each quantity. σ_S is dominated by the photon shot noise on each individual pixel which propagates to the estimation of the similarity, and σ_λ is a property of the laser source used. Fluctuations in the input beam polarisation, position or angle produce only negligible contributions to the noise, as the similarity of speckle from an integrating sphere is largely insensitive to path-independent effects (as shown in section 3.4). We are then facing two possible cases, where either the σ_S or the σ_λ term dominates.

When σ_S dominates, which is the case of our experiment, we have $\sigma_n = 2\Delta n_0 \sigma_S$. In principle, σ_S could be determined analytically knowing the probability law of the noise on each pixel and the explicit expression of the similarity, but this turns out to be a very difficult problem. Instead, we find an empirical law[1] for σ_S, approximately given by $0.1/\sqrt{N}$ for our camera and illumination conditions, with N the number of pixels (for our image size, 200×200, this gives $\sigma_S \approx 5 \times 10^{-4}$). Inserting the expressions of Δn_0 and σ_S we find

$$\sigma_n \approx \frac{3\lambda\,|\ln\rho|}{40\pi R\sqrt{N}}. \tag{5.7}$$

With our parameters, this gives $\sigma_n = 7 \times 10^{-10}$, which is in accord with the level of noise found in Fig. 5.3.

As σ_S is reduced by increasing image size, the σ_λ term may become dominant, which sets a lower limit to performance with an uncertainty $\sigma_n = \sigma_\lambda/\lambda$. Note that estimating the similarity noise as a function of image size can serve as a way of measuring σ_λ. Indeed, if a plateau is reached as image size is increased, σ_λ can be inferred from the value of that plateau.

In this work, we use a laser with low wavelength drift (less than 0.1 fm) and a standard CMOS camera. Therefore we are in the first case described above where camera noise dominates[2]. However this cannot be the only reason for our lower uncertainty compared to other reported works. Indeed, the best performance found in the literature uses a HeNe laser [83], and if the reported uncertainty (2×10^{-6}) were to be attributed to wavelength noise, we would have $\sigma_\lambda = 3$ pm, which is much

[1] This is found by applying the same protocol, without any refractive index variation, and extracting the standard deviation of the resulting signal.

[2] For this reason the uncertainty associated with wavelength fluctuations is not taken into account in the rest of this thesis.

higher than the typical fm-level noise of a wavelength-stabilised HeNe laser. As the effect of camera noise increases with the HWHM (Δn_0 is in factor of σ_s in Eq. (5.6)), this is probably the dominant source of uncertainty in most other works reported in the literature.

5.6 Tackling the heating effect via volume change

As we saw in section 3.7, using an integrating sphere exposes us to an intrinsic heating effect, which is unavoidable and gives the same signal as a refractive index variation. Among the different ways to mitigate against this effect that we mentioned, one is through a direct physical compensation. This is the route we take here.

As thermal expansion is equivalent to a refractive index variation or a wavelength variation, we can use either of these to physically compensate the expansion. As here we need to apply a small and steady variation, this time changing the refractive index is simpler to implement. This is because it can be done by changing the volume of the chamber with a syringe mounted on a commercial syringe pump (WPI AL2000), just like we did for the measurement of the similarity profile in Fig. 5.2. The equivalent procedure using wavelength was not possible in the setup. This is not the most elegant approach, as we modulate the same variable as that we want to measure. However the compensation is constant in time and independent on the measured variation. Denoting t_0 the measured HWHM of the Lorentzian profile in time, and using the equivalence $\Delta n \Leftrightarrow \Delta R/R$, we find that the volume rate that must be applied to compensate the expansion is $\dot{V} = -3V \ln \rho/(4n'kRt_0)$. For $t_0 = 7.6$ min as found in Fig. 3.8, and with the same parameters as above, we have $\dot{V} = 0.79$ ml min^{-1}. The volume of the chamber was continuously increased at this rate in the measurement of Fig. 5.3 to compensate for the thermal expansion.

In future developments, compensation of the expansion could also be accomplished via a steady wavelength increase, or via a direct temperature stabilisation of the sphere. One might also take the route of signal processing. For example, Fourier filtering could be applied to remove low frequency components, or the signal could be analysed directly in the Fourier domain (as is done in Chapter 6) depending on the application.

In any case, reducing the sensitivity to temperature variations would be beneficial. We can be more quantitative on this by computing the temperature variation that is equivalent to a certain refractive index variation that we want to measure. For a temperature change ΔT, we have $\mu = nk\Delta\overline{z}$, with $\Delta\overline{z} = \alpha\overline{z}\Delta T$, where α is

the thermal expansion coefficient. Equating this to the μ obtained for a refractive index variation, we find the simple equivalence $\Delta T = \Delta n/\alpha$. This means that if we want to measure Δn, we want temperature to vary much less than $\Delta T = \Delta n/\alpha$ in the time scale of the measurement. We then want the lowest possible value for α. For example, for measuring the value of our resolution ($\Delta n = 4.5 \times 10^{-9}$) with a sphere made of aluminium ($\alpha = 23 \times 10^{-6}\mathrm{K}^{-1}$), we find $\Delta T = 0.2$ mK. For a sphere made of zerodur[3] ($\alpha = 0.05 \times 10^{-6}\mathrm{K}^{-1}$), we find $\Delta T = 0.1$ K, which shows that zerodur could be a good alternative for stability.

5.7 Conclusion

In summary, we proposed a route to optimise speckle-based measurements of refractive index. While intuition suggests that the correct strategy is to maximise the path-length of light in the medium of interest, we find that it is more important to maximise the *spread* in path-length distribution within the medium. In particular, we have demonstrated that an integrating sphere, in which light has a broad path-length distribution, offers a simple yet sensitive probe of refractive index change of the medium it encloses. We quantified the change in the speckle pattern using the similarity, analytically demonstrated that this takes a simple Lorentzian form as a function of refractive index change (5.2), and verified it experimentally. We gave a general expression for the HWHM of the similarity curve, and found that it depends mainly on the radius and surface reflectivity of the sphere, which paves the way for possible optimisations. In our setup, we found the HWHM to be 6.5×10^{-7}.

We exploited this high sensitivity to measure small refractive index variations of amplitude 4.5×10^{-9} with an uncertainty of 7×10^{-10}. Our method allows a level of uncertainty comparable to current state of the art techniques, but with a significantly simpler implementation. On the other hand, it allows the measurement of variations (instead of absolute values) in refractive index and requires some care regarding heating effects due to the input laser light. This however can be compensated by applying either an appropriate volume or wavelength change, and could also be reduced in future devices by a more judicious choice of the material from which the integrating sphere is constructed.

Importantly, the measurements presented here are three orders of magnitude more sensitive than previous implementations based on laser speckle. We identified that the use of shorter laser wavelength, larger image arrays and especially higher-

[3]Zerodur is a type of glass that has the lowest thermal expansion coefficient of all known materials.

reflectivity coating inside the sphere offer significant opportunities to measure even smaller refractive index changes (with a limit ultimately determined by wavelength stability). This work is most likely to find applications in chemical sensing, in particular the detection of trace gases or small concentrations of chemicals in liquids. The study of the heating effect also suggests applications in the measurement of small temperature variations.

Chapter 6

Displacement measurement

The work presented in this chapter was submitted for publication and is currently under review. A preprint can be found at [86].

List of symbols and abbreviations

ϕ	phase variation applied to the field
k	wavenumber
$\boldsymbol{u}$	unit vector parallel to a chord
x	displacement
s	variable determining if a chord changes length or not
S	speckle similarity (Pearson correlation coefficient of intensity)
μ	average phase variation of the field on a chord
σ	standard deviation of the phase variation of the field on a chord
ρ	reflectivity of the integrating sphere
HWHM	half width at half maximum
θ, ϕ	polar angles of a chord in a spherical coordinate system
β,	angle between the direction of displacement and the z axis
f	probability density function

6.1 Introduction

Measuring small displacements is a classical metrology task. From the Vernier scales used in the early experiments of Cavendish and Coulomb to LIGO, many methods have been developed with various degrees of resolution and complexity [87, 88]. Optical techniques are dominated by classic interferometric schemes such as the Michelson interferometer, even though more original techniques keep being devel-

oped. Examples of these are the use of strong phase variations of the superoscillatory field produced by a metasurface to resolve nanometre-level displacements [89], or the encoding of displacement into polarisation using g-plates allowing sub-nanometric resolution [90].

A number of speckle-based techniques have also been developed. When laser light is reflected on a rough surface, the resulting speckle acts as if it was "attached" to it, translating and rotating when the surface is translated and rotated by a small amount. This property (which is a special case of optical memory effect [91] and sometimes called as such) is at the basis of most applications of speckle in this field. It allows the measurement of the translation [92], and rotation [93] of a test surface, or even the spatial mapping of displacement [94]. Many improvements and variations of these have since been made [95]. The current most accurate speckle-based method for displacement measurement tracks singularities in the pseudo phase of a moving speckle pattern to reach nanometric precision [96, 97].

In this chapter, we improve the previous speckle-based techniques by using a fundamentally different approach. Instead of using speckle patterns produced by a single reflection, displaying the optical memory effect, we use ones resulting from multiple reflections in an integrating sphere. This produces much more sensitive speckles, where displacement manifests itself as a structural change, rather than a translation. While measuring translation is a simple task, we now need to interpret a structural change to relate it to displacement. We will achieve this by using the similarity, that we relate to displacement with the model we developed in Chapter 3. In the Fourier domain, this allows a noise floor of 5 pm/$\sqrt{\text{Hz}}$ ($\lambda/160,000$) above 30 Hz in a facile implementation, which we use to measure oscillations of 17 pm amplitude with a signal to noise ratio of 3.

6.2 Similarity profiles

We consider a special arrangement where the integrating sphere used to produce the speckle pattern is made of two independent hemispheres, such as the one shown in Fig. 2.1. One of the hemispheres is allowed to move by a small amount. Two particular directions of motion are considered: the axial motion (away or towards the other hemisphere, z axis on Fig. 6.1), and transverse motion (sideways, $x-y$ plane on Fig. 6.1). We want to derive the expression of the similarity profiles for the axial and transverse motion, starting from Eq. (3.14). The first step is to express the phase shift on a chord resulting from the displacement of the hemisphere. The effect of the displacement is to change the lengths of the chords, and therefore the

length of propagation of light, which is why the effect takes the form of a phase shift. Along a chord of length z, light acquires a phase kz, with k the wavenumber. When the hemisphere is displaced, this phase varies by $k\Delta z$, with Δz the change in length (the ends of the chords are "attached" to the sphere and move with it). For small displacements, Δz is given by $\boldsymbol{u} \cdot \boldsymbol{x}$, with $\boldsymbol{u}$ a unit vector parallel to the chord (oriented from the fixed to the moving end of the chord), and $\boldsymbol{x}$ the displacement vector of the moving hemisphere. Moreover, no phase shift occurs if the chord starts and ends on the same hemisphere. This can be modelled by a variable s, that takes a value of 0 when both ends of the chord belong to the same hemisphere, and 1 otherwise. It follows that the phase shift induced by the displacement on a chord can be expressed as

$$\phi = k\, \boldsymbol{u} \cdot \boldsymbol{x}\, s. \tag{6.1}$$

The terms μ and σ^2 in Eq. (3.14) are the mean and variance of ϕ. We therefore seek to express the following quantities

$$\mu = \overline{\phi} \qquad \sigma^2 = \overline{\phi^2} - \overline{\phi}^2, \tag{6.2}$$

where the bar indicates averaging over random chords in the sphere[1].

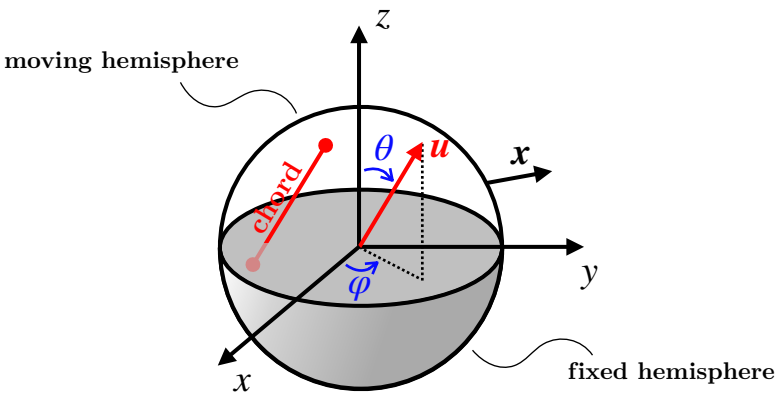

Figure 6.1: Notations. $\boldsymbol{x}$ is the displacement vector of the moving hemisphere. For a given chord, $\boldsymbol{u}$ is a unit vector parallel to the chord and pointing in the upper half-space. $\boldsymbol{u}$ is expressed in a spherical coordinate system centred on the sphere and oriented as shown. In this figure the sphere is presented as a unit sphere, such that the $\boldsymbol{u}$ vector lies on its surface, but the relative sizes of the sphere and $\boldsymbol{u}$ are arbitrary.

Let us express ϕ in more explicit terms before computing the averages. We express $\boldsymbol{u}$ in a spherical coordinate system, with the origin at the centre of the

[1] As discussed in 3.3, a random chord is a chord whose endpoints are chosen with a uniform probability density across the sphere's surface.

sphere and the z-axis oriented such that it points perpendicularly to the separation between the two hemispheres, with the moving hemisphere being on the positive side (see Fig. 6.1). In this system we use the spherical angles $\theta \in [0\ \pi/2]$ and $\varphi \in [0\ 2\pi]$. The restricted range of θ is chosen to guarantee that $\boldsymbol{u}$ is uniquely defined for a given chord, and points from the fixed to the moving hemisphere. In the axial case, we have $\boldsymbol{x} = x\hat{\boldsymbol{z}}$, and therefore $\phi = kx\cos\theta\, s$, with θ the angle between the chord and the z-axis. With this we can express μ as

$$\mu = \iint kx\cos\theta\, s\, f(\theta, s)\mathrm{d}\theta\mathrm{d}s, \tag{6.3}$$

with $f(\theta, s)$ the joint probability density of θ and s. As s is a discrete variable, this can be recast as

$$\mu = \int_0^{\pi/2} kx\cos\theta\, s\, P(s=1|\theta) f(\theta)\mathrm{d}\theta, \tag{6.4}$$

with $P(s=1|\theta)$ the probability of s being 1 for a given θ, and $f(\theta)$ the probability density of θ.

We can find $f(\theta)$ in the following way. By symmetry, the distribution of random chords is isotropic. The set of all possible $\boldsymbol{u}$ vectors then forms a uniform unit hemisphere. The number of chords contained around a certain θ is then proportional to the surface element in our spherical system, which is proportional to $\sin\theta$. After normalisation, we simply have $f(\theta) = \sin\theta$. $P(s=1|\theta)$, on the other hand, can be shown to be $\cos\theta$. The derivation is more subtle and is shown in Appendix E.

We have now everything in hand to to compute the integrals:

$$\begin{aligned} \mu &= \int_0^{\pi/2} kx\cos\theta\cos\theta\sin\theta\mathrm{d}\theta \\ \mu &= \frac{kx}{3}. \end{aligned} \tag{6.5}$$

Similarly for σ^2:

$$\begin{aligned} \sigma^2 &= \int_0^{\pi/2} (kx\cos\theta)^2\cos\theta\sin\theta\mathrm{d}\theta - \mu^2 \\ \sigma^2 &= \frac{(kx)^2}{4} - \frac{(kx)^2}{9} = \frac{5}{36}(kx)^2. \end{aligned} \tag{6.6}$$

In the transverse case, we have $\boldsymbol{x} = x\hat{\boldsymbol{x}}$ (or any direction in the xy plane), and therefore $\phi = kx\sin\theta\cos\varphi\, s$, with θ the angle between the chord and the z-axis, and φ the azimuthal angle of the chord with respect to the x-axis. This invokes the probability density of the azimuthal angle $f(\varphi)$, which by symmetry is uniform,

giving $f(\varphi) = 1/2\pi$. This leads to

$$\begin{aligned} \mu &= \int_0^{2\pi} \int_0^{\pi/2} kx \sin\theta \cos\varphi \cos\theta \sin\theta \frac{1}{2\pi} \mathrm{d}\theta \mathrm{d}\varphi \\ \mu &= 0 \end{aligned} \tag{6.7}$$

$$\begin{aligned} \sigma^2 &= \int_0^{2\pi} \int_0^{\pi/2} (kx \sin\theta \cos\varphi)^2 \cos\theta \sin\theta \frac{1}{2\pi} \mathrm{d}\theta \mathrm{d}\varphi \\ \sigma^2 &= \frac{(kx)^2}{8}. \end{aligned} \tag{6.8}$$

We can also perform the calculation for an arbitrary direction of displacement forming an angle β with the z-axis, in which case we find

$$\begin{aligned} \mu &= \frac{kx}{3} \cos^2\beta \\ \sigma^2 &= (kx)^2 \left(\frac{1}{8} \sin^2\beta + \frac{5}{36} \cos^2\beta \right), \end{aligned} \tag{6.9}$$

yielding the axial and transverse results from $\beta = 0$ and $\beta = \pi/2$ respectively.

Results (6.5) to (6.8) were verified numerically by generating a set of random points uniformly distributed across the unit sphere. The points belonging to one hemisphere were translated in either the axial or transverse direction, and the statistics of the chord length variations were computed, using 10000 points and 50000 chords between them. We found very good agreement to 1 part in 1000, the limitation being the number of chords generated.

With the values of μ and σ^2, we can now compute the similarity profiles:

1. For an axial displacement, we find $\mu = kx/3$ and $\sigma = kx\sqrt{5}/6$. Inserting this in Eq. (3.14), and neglecting the σ term (see Appendix D), we obtain

$$S = \frac{1}{1 + \left(\dfrac{kx}{3 \ln\rho} \right)^2}, \tag{6.10}$$

which is a Lorentzian with an HWHM given by $3\lambda \left|\ln\rho\right| / 2\pi \approx 0.5\lambda \left|\ln\rho\right|$.

2. For a transverse displacement, we have $\mu = 0$ and $\sigma = kx/\sqrt{8}$, leading to

$$S = \frac{1}{\left(1 - \frac{(kx)^2}{16 \ln \rho}\right)^2}, \tag{6.11}$$

which is a squared-Lorentzian with an HWHM of $\sqrt{16(\sqrt{2}-1)}/2\pi\lambda\sqrt{|\ln\rho|} \approx 0.4\lambda\sqrt{|\ln\rho|}$.

The axial motion imparts a greater change to the speckle pattern than the transverse one. This can be understood qualitatively. In the axial case, all chord that change in length increase in length. In the transverses case, half of the chords that change in length increase and half decrease in length. In the transverse case, some chords can then compensate each other, leading to small change.

For modest parameters such as $\lambda = 780$ nm and $\rho = 0.9$, the HWHM is 39 nm in the axial case, and 104 nm in the transverse case. Those numbers are consistent with our empirical observation of the very high speckle sensitivity. Note that the sensitivity of the speckle pattern to displacement is independent of the size of the sphere.

Just as in Chapter 5, the knowledge of the similarity profiles allows us to infer the displacement between two given times, by simply applying the reciprocal function of the appropriate profile and using the value of the similarity of the two corresponding speckles. For example, for the axial profile, using (6.10) we have:

$$x = x_0\sqrt{1/S - 1}, \tag{6.12}$$

with x_0 the HWHM.

6.3 Experimental implementation

In this section we experimentally verify the relations (6.10) and (6.11) with the setup described in Fig. 6.2. Laser light enters the integrating sphere and the resulting speckle pattern is recorded on a camera. The sphere-camera distance is 20 cm, with a laser power of 10 mW (see complementary experimental details in section 2.4). The sphere is made of a fixed and a moving hemisphere. The fixed hemisphere rests on a manual translation stage, for coarse alignment of the two halves, and the moving hemisphere rests on a 3D precision stage capable of nanometer precision (PI P-733.3DD).

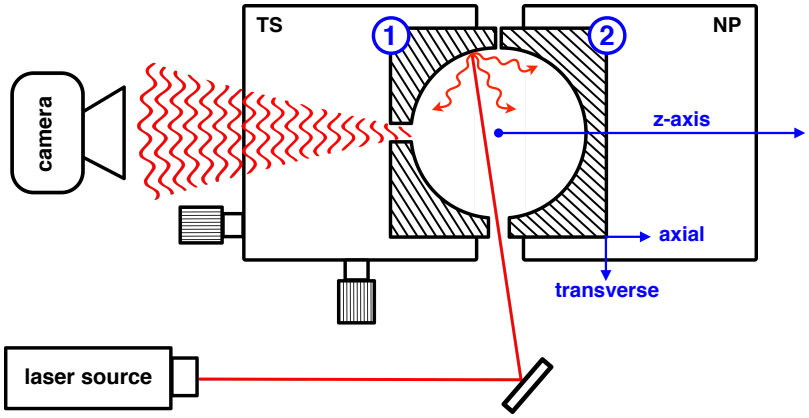

Figure 6.2: Experimental setup. Laser light enters the integrating sphere and produces a speckle pattern recorded on a camera. Hemisphere (1) rests atop a manual 3D translation stage (TS) for coarse alignment with hemisphere (2), which rests atop a motorised nanopositioner (NP). The latter is moved at a constant speed while the changing speckle pattern is recorded. The z-axis, the axial and transverse directions are shown.

We displace the moving hemisphere in the axial and transverse (horizontal) direction at a constant speed of 0.1 $\mu\mathrm{m\,s}^{-1}$ while the changing speckle is recorded, and extract the similarity profiles by applying expression (3.1) between one reference and subsequent images. The resulting profiles are shown in Fig. 6.3. We find a good agreement for the axial profile, while the transverse profile shows a small deviation. This difference was found to be systematic and independent of the experimental conditions (such as the incidence angle of the laser, or the initial position of the moving hemisphere). In section 6.4, we show how this can be explained by a small deviation from the assumptions of our model, in particular the Lambertian reflectance and the uniformity of the reflectivity across the inner surface. The variability of the profiles, given by the error bars, is found in the same way as described in section 4.3. We also plot the theoretical profiles (6.10) and (6.11).

Note that the coherence length of the laser does not need to be as high as that used in this study. The standard deviation of the path length distribution of the sphere is $4R/(3\,|\ln\rho|)$ (derived from the path length distribution given in [43]), which is equal to 19.5 cm with our parameters. The coherence length only needs to be large compared to the standard deviation of path length, therefore more standard laser sources with coherence lengths of the order of meters should be suitable.

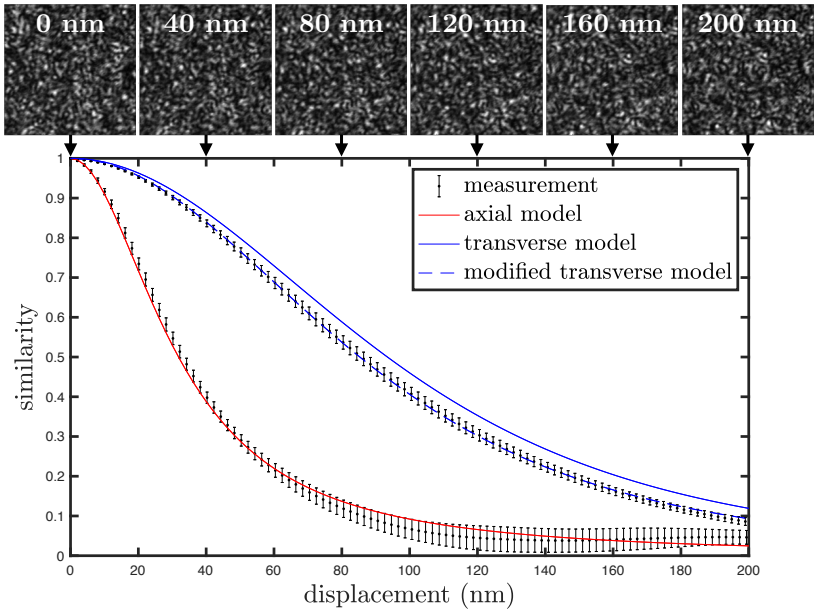

Figure 6.3: Speckle similarity profiles as a function of displacement. Experimental data (black), axial theoretical profile (red), and transverse theoretical profile (blue). The HWHM is 32 nm in the axial case and 85 nm in the transverse case. The observed transverse profile shows a small systematic deviation from the model, which can be explained by an imperfect Lambertian reflectance and/or a non uniform reflectivity. This is taken into account in the modified model (dashed blue). The images show the speckle pattern in the transverse case.

6.4 Hypotheses on the systematic deviation of the transverse profile

In the measurement of the transverse profile, we found a small but systematic deviation from the model's prediction (see Fig. 6.3). Here we show that this can be explained by a deviation from some of the assumptions of the model, in particular the Lambertian reflectance and uniform reflectivity (assumption 2). When such deviations are introduced in the model, we find that it does not change the prediction of the axial profile in first approximation, but does change that of the transverse profile. The obtained modified model can be empirically adjusted to reproduce the observed profile.

In Chapter 3, we derived the general expression of the similarity for an arbitrary transformation (eq. (3.14)). The last step of the derivation, Eq. (3.13), can be expressed as follows

$$S = \left| \int_0^\infty -\ln\rho \, \left(\rho \overline{e^{i\phi}}\right)^N dN \right|^2 , \tag{6.13}$$

where ϕ, the phase shift on a chord, is Gaussian with mean μ and variance σ^2, and the overline designates averaging over random chords. We saw that the combination of the Lambertian reflectance, uniform reflectivity, and spherical geometry conspire in such a way that the intensity of a light ray always decreases by the same factor after each reflection. For this reason, only the phase term is in the chord-averaging and the reflectivity ρ is outside.

We can describe any deviation from the Lambertian reflectance or the uniform reflectivity by a dimensionless function g, which we include in the chord-averaging. This function can contain a direction dependence to model an excess of power in the specular direction for example, or a position dependence to model a non uniform reflectivity. We have $g = 1$ for a Lambertian reflectance and uniform reflectivity, and $\overline{g} = 1$ in any case[2]. With this definition, the previous $\rho\overline{e^{i\phi}}$ term becomes $\rho\overline{ge^{i\phi}}$. The actual expression of this term would be difficult to derive in any particular case, but we can still infer the effect of g on the final similarity profile. We start by expressing $\overline{ge^{i\phi}}$ as differing from $\overline{e^{i\phi}}$ by a complex number ae^{ib}, reading

$$\overline{ge^{i\phi}} = ae^{ib}\overline{e^{i\phi}}, \tag{6.14}$$

with a and b unknown dimensionless functions of kx.

We can be more specific on the behaviour of a and b. First, for no displacement ($x = 0$), we have $a = 1$ and $b = 0$, as $\overline{g} = 1$. Also, as kx is relatively small in our range of measurement (0.26 for $x =$ HWHM), we can Taylor expand a and b around zero. By keeping only the first non-zero terms of the Taylor expansions, we have $a = 1 + \alpha(kx)^2/2$ and $b = \beta kx$, with α and β small dimensionless numbers. Indeed, it can be shown (by expanding the derivative with respect to x of eq. (6.14)) that the derivative of a is zero at $kx = 0$. Using these expansions, we can insert (6.14) in place of $\overline{e^{i\phi}}$ in (6.13), perform the integral and see the impact this has on the final form. We find the modified profile

$$S = \frac{1}{\left(1 - \dfrac{\sigma^2 + \alpha(kx)^2}{2\ln\rho}\right)^2 + \left(\dfrac{\mu + \beta kx}{\ln\rho}\right)^2}. \tag{6.15}$$

In the axial case, we see that the modification is negligible, as the sigma term was already negligible in the original profile, and $\mu \gg \beta kx$. Therefore, the axial

[2] As g redistributes power in direction and position but does not change the total amount of power.

profile is unchanged. In the transverse case, we have

$$S = \frac{1}{\left(1 - (1+8\alpha)\dfrac{(kx)^2}{16\ln\rho}\right)^2 + \left(\dfrac{\beta kx}{\ln\rho}\right)^2}, \tag{6.16}$$

where we see that the modification is no longer negligible. This modified profile has two free parameters α and β, and gives an excellent fit of the data for $\alpha = 0.027$ and $\beta = 0$, which is an argument in favour of our hypothesis.

The modified profile is shown in Fig. 6.3. Note that this modification acts as a scaling of the original profile (6.11) in the x direction by 10%. This suggest the possibility of a calibration issue of the nanopositioner. However the amplitude of displacement was verified independently using a Michelson interferometer and this possibility was excluded. An imperfect Lambertian reflectance is more likely, as it was shown [98] that even in the case of spectralon, significant deviations from the ideal Lambertian reflectance are observed. In particular, an excess of power in the specular direction (specular reflection), as well as in the incident direction (backscattering), and polarisation dependence were found.

6.5 Variation with a virtual hemisphere

We can apply a small modification to the experimental setup, where the moving hemisphere is replaced by a flat mirror (Thorlabs BB1-E03) with reflectivity > 0.99. In this arrangement, we find that the speckle becomes more sensitive to axial motion and insensitive to transverse motion. The similarity profile obtained for the axial motion is shown in Fig. (6.4).

Although the geometry of the problem seems very different from the previous experiment, we find again a Lorentzian profile, with a HWHM precisely twice smaller (the same factor of two was found with other spheres of different reflectivities and radii). This curious result can be understood in a simple way if we think of the image of the fixed hemisphere. The real and the virtual hemispheres form together a complete sphere, in which we can apply our previous model as if the whole sphere was real. The motion of the mirror implies an axial motion of the virtual hemisphere, just like we had in the previous setup. The virtual hemisphere however, by its very nature, moves twice as much as the mirror, which explains the factor of two. Also, transverse motion does not change the position of the virtual hemisphere, which is consistent with the absence of speckle change in that case.

In this interpretation we neglect the effect of the mirror's own reflectivity (>0.99

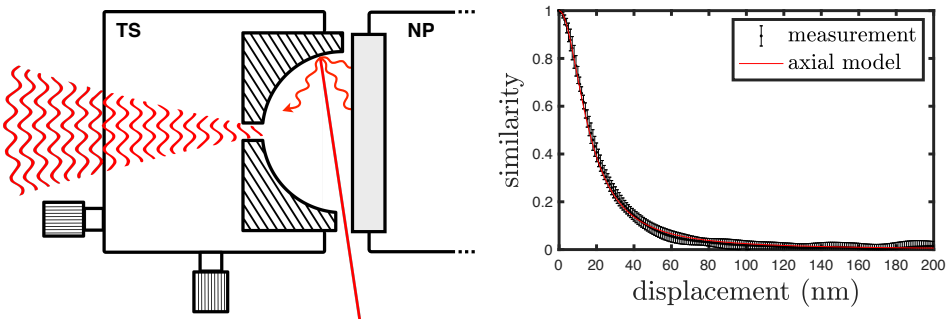

Figure 6.4: Left: a modified version of the experimental setup of Fig. 6.2, where the moving hemisphere is replaced by a flat mirror. Right: Axial similarity profile obtained in the modified setup. The profile is also Lorentzian, with a HWHM of 16 nm, precisely half that found in the previous setup. This factor of two finds a simple explanation in terms of the moving virtual image of the hemisphere. Here the axial model is obtained by multiplying x by 2 in Eq. (6.10).

at 6° and 45° angle of incidence), as it is much higher than that of the sphere (0.918). If both reflectivities were closer together, the result would be less trivial. In fact, as any path reaching the virtual hemisphere has to undergo a reflection on the mirror, the similarity profile would be that of a real sphere divided in two regions of different reflectivities, one ρ and one $\rho'\rho$ (with ρ' the mirror's reflectivity), which would surely result in a similarity profile implying a non-trivial combination of ρ and ρ'.

6.6 Measurement of small axial displacements

In this section we use the hemisphere-mirror configuration to measure small displacements. For displacements much smaller than the HWHM, using directly Eq. (6.12) is not ideal, as around $x = 0$ the similarity only changes at second order. We are exactly in the same situation as in the previous chapter (section 5.4). To solve this, we use the same method of applying an initial wavelength offset, to reach a point of non-zero gradient of the similarity profile. This time however, we make an improvement to this method by using the point of maximal gradient. For a Lorentzian profile of HWHM noted x_0, the point of maximal slope (or inflexion point) is found at $x = x_0/\sqrt{3}$, which corresponds to $S = 3/4$. Again, we make use of the fact that transformations that are dominated by the μ term in Table (3.2) can be used interchangeably to produce the same change in the final speckle pattern. We then use a wavelength variation instead of a displacement, which has the same physical effect and can be controlled independently. This initial wavelength variation is applied

by varying the diode current of the laser[3], and chosen so that the similarity drops to a value close to 3/4. The speckle before and after the variation are recorded, the similarity between them is computed (denoted S_λ), from which an equivalent displacement is extracted $x_\lambda = x_0\sqrt{1/S_\lambda - 1}$. Subsequent measurements of S correspond to a displacement $x = x_0\sqrt{1/S - 1} = x_\lambda + \delta x$, with δx any subsequent displacement. It follows that δx is given by

$$\delta x = x_0\sqrt{1/S - 1} - x_\lambda. \tag{6.17}$$

We apply this approach in the hemisphere-mirror configuration described in the previous section, so that only the axial component is probed. A gap of about 0.5 mm is left between the hemisphere and the mirror, and the mirror is attached to a piezoelectric crystal (APC 70-2221) to apply controlled sinusoidal displacements. We start by applying a 25 Hz modulation with 2.3 nm amplitude. The displacement is found using Eq. (6.17) and shown in Fig. 6.5(a). We see that the measured displacement is made of a sinusoidal component superposed to a linear component. This linear component comes from the heating effect, described in section 3.7. Here, instead of physically compensating the effect as in Chapter 5, we take the route of analysing the signal in the Fourier domain, which allows us to disentangle the heating from displacement. The Fourier spectrum is shown in Fig. 6.5(b), where a very distinct 2.3 nm peak at 25 Hz is found. The heating effect manifests itself as a linear increase in the time domain, which translates into a peak at 0 Hz in the frequency domain, resulting in the monotonically decreasing component found in 6.5. Small random fluctuations are also observed in the Fourier transform, which comes form the random fluctuations of the original signal in the time domain.

We want to determine the resolution limit of the method. To that aim, we decrease the modulation amplitude until the peak in the Fourier spectrum is about 3 times larger than the noise floor. Still operating at 25 Hz, we reach a modulation amplitude of 17 pm. The measured displacement is shown in Fig. 6.5(c) and its Fourier spectrum in Fig. 6.5(d). We also show in red in Fig. 6.5(d) the Fourier spectrum of displacement when no modulation is applied, which gives the fundamental noise level. This is below 14 pm/$\sqrt{\text{Hz}}$ above 10 Hz, and reaches a plateau of 5 pm/$\sqrt{\text{Hz}}$ above 30 Hz. In each case of Fig. 6.5, we record 4 s at a sampling frequency of 100 Hz, and the Fourier spectrum is found by taking the absolute value of the Fast Fourier Transform (FFT) with a 10 fold zero padding. With the displace-

[3]Note that the precise value of the initial wavelength shift need not be known, as it does not come into play at any stage of the calculations. We only need the similarity to be brought close to 3/4.

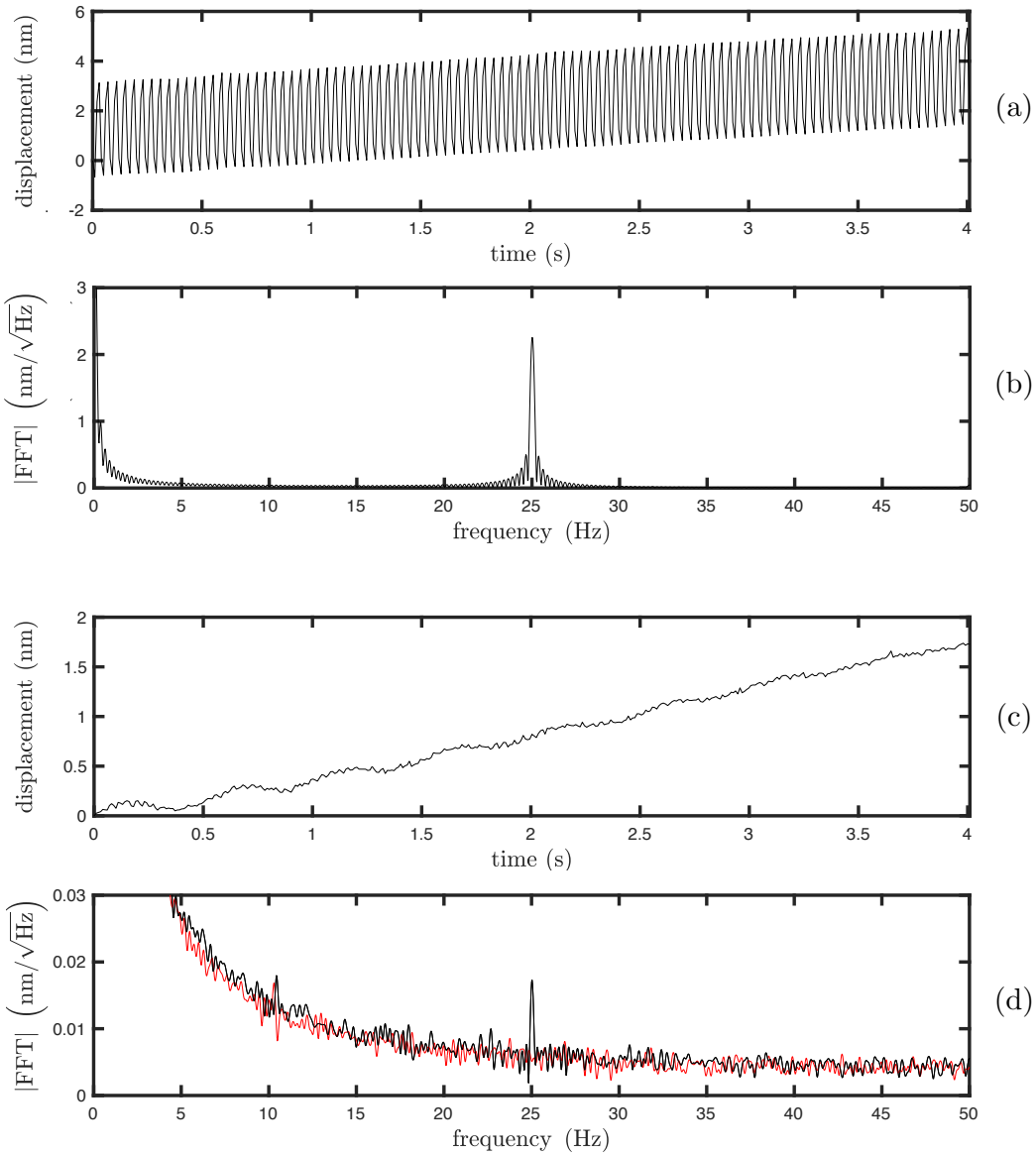

Figure 6.5: (a) and (b): measured displacement as a function of time and its Fourier spectrum when a 25 Hz modulation of 2.3 nm amplitude is applied. (c) and (d): measured displacement as a function of time and its Fourier spectrum when a 25 Hz modulation of 17 pm amplitude is applied. In panel (d) is also shown the Fourier spectrum of displacement when no modulation is applied (red). In each case, we record 4 s at a sampling frequency of 100 Hz.

ment signal in nanometers and time in seconds, the units of the absolute value of the Fourier transform is $\mathrm{nm}/\sqrt{\mathrm{Hz}}$, following the properties of the Fourier transform (this is most easily seen through the Parseval theorem). Its interpretation is that when the absolute value of the FFT is properly normalised (multiplied by two and divided by the number of time steps in the original signal) the height of a peak in the frequency domain is equal to the amplitude of the corresponding sinusoid in the time domain.

The performance of the method can be improved mainly via three parameters: the wavelength, the sphere's reflectivity, and the number of pixels in the image. On one hand, the smallest detectable displacement scales with the width of the similarity profile, which depends directly on the wavelength and the sphere's reflectivity, as shown by Eqs. (6.10) and (6.11). Cone, et al, have demonstrated diffusely reflecting surfaces with reflectivity up to 0.99919 at 532 nm [99]. With these parameters, the combined effect of the higher reflectivity and shorter wavelength would give an axial HWHM of 206 pm (or 155 times smaller). Finally, as the main source of noise is photon shot noise on the camera, its effect can be reduced by increasing the number of pixels in the image. Note that increasing laser power does not necessarily help decreasing camera noise as the camera parameters must be such that the pixels do not saturate. If the exposure time is already such that the dark signal is negligible, then increasing laser power does not decrease camera noise.

6.7 Conclusion

In this chapter, we considered a special arrangement where an integrating sphere is split into two hemispheres, where one is fixed and one is free to move in any direction. We empirically found that the resulting speckle is remarkably sensitive to the relative displacement of the two hemispheres. We characterised this sensitivity using our model of Chapter 3, and experimentally verified its predictions. We also demonstrated that, by replacing one hemisphere with a highly-reflective mirror, the displacement sensitivity is enhanced by a factor of 2 in the axial direction while vanishing in the transverse direction, which gives an elegant method to selectively probe one direction of motion. Using this hemisphere-mirror configuration, we found a noise floor of 5 pm/$\sqrt{\text{Hz}}$ above 30 Hz, and measured a sinusoidal displacement of 17 pm amplitude (or 6 times smaller than a hydrogen atom) with a signal to noise ratio of 3.

Displacement measurement in itself is not new, as many techniques have been developed for a very long time. The elegance of this particular technique lies mainly in its simplicity of implementation. It may indeed consist of the simplest possible interferometric displacement measurement, as it requires no fine alignment, and contains only 3 simple elements: a laser, an integrating sphere, and a camera. The fact that such a simple arrangement allows the detection of displacements smaller than the dimension of the smallest atom is quite remarkable.

Along our investigations we came across a very particular type of transformation where the average phase in Eq. (3.14) is zero, which is the transverse motion. In all

other effects studied in this thesis (apart from the Aharonov-Bohm effect), the similarity profile is dominated by the average phase, and the effect of its variance plays a negligible role. The transverse motion is a special case where *only* the variance plays a role. We proved that this situation is that where the similarity profile is most sensitive to the validity of the assumptions behind Eq. (3.14), and indeed we found a small deviation, which we suspect comes from an imperfect Lambertian reflectance. Future analytical developments may exploit this feature of the transverse profile to extract reflectance properties of a test surface.

Chapter 7

Speckle and polarisation

The work presented in this chapter was published in [100].

List of symbols and abbreviations

$\boldsymbol{E}$	complex field
ω	angular frequency of light
t	time
$\boldsymbol{u}$	Jones vector
C	coherency matrix
S_n	nth Stokes parameter
$\boldsymbol{S}$	Stokes vector
S	matrix containing N realisations of $\boldsymbol{S}$ in columns
σ_n	nth Pauli matrix
Tr	trace operator
J	Jones matrix (transforming the Jones vector)
M	Mueller matrix (transforming the Stokes vector)
$\boldsymbol{I}$	vector containing the values of intensity at each pixel
I	matrix containing N realisations of $\boldsymbol{I}$ in columns
T	transformation matrix between the Stokes vector of the input beam and the resulting intensity profile
L	number of pixels in one speckle image
N	number of polarisation states
k	number of laser beams

7.1 Introduction

When the polarisation state of a laser beam incident on a complex medium is changed, a change is observed in the resulting speckle pattern. As we discussed in section 3.4, this change cannot be increased by the multiple scattering of light, because it is a path-independent transformation. This is in contrast to what we had with refractive index and displacement, where the multiple scattering of light dramatically increased the sensitivity of the speckle pattern. We therefore cannot hope to measure very small changes in polarisation in this way. However, this is balanced by the fact that the speckle is a very simple function of polarisation.

A previous study derived an explicit expression for estimating the Stokes parameters (which described the polarisation) of a laser beam, in terms of the cross-correlations between the speckle pattern it produces and four particular speckle patterns corresponding to the four classical polarisation filters [101]. Later studies included a generalised approach using Jones-like transmission matrices [102], and Mueller-like transmission matrices allowing spatially resolved polarimetry [103], and spectropolarimetry [104].

In this chapter we will derive the linear relationship between polarisation and speckle and verify it experimentally. We will then exploit it in a metrological perspective, and develop a new method which allows one to use an arbitrary number of reference polarisation states. We will quantitatively study the uncertainty on the retrieval as a function of key experimental parameters, and show that the Stokes parameters can be measured with an uncertainty of 0.05 using speckle images of 150×150 pixels and 17 reference polarisation states states.

We will also extend the method to show that the polarisation state of multiple beams can be measured simultaneously from one single speckle pattern. This will be demonstrated experimentally for the case of two beams.

7.2 Polarisation

Let us begin with some background that will be necessary for the rest of this chapter. Polarisation is a general property of vector waves. Light is such a wave: the oscillating physical quantity, the electric field, is a vector oscillating in the plane perpendicular to the direction of propagation. There are many ways to oscillate in a plane. If we look at one point of space in an electromagnetic wave, and if the wave is monochromatic, the extremity of the electric field at that point describes a closed trajectory in time. The shape of this trajectory defines the polarisation. We can express the field as the sum of two fields along two perpendicular directions (in

the plane of oscillation), each being a sinusoid of a given amplitude and phase. We have

$$\boldsymbol{E} = \begin{pmatrix} a_x \cos(\omega t + \phi_x) \\ a_y \cos(\omega t + \phi_y) \end{pmatrix}. \tag{7.1}$$

This defines a parametric equation for $\boldsymbol{E}$ in the plane, whose parameter is time, and the resulting trajectory is an ellipse. Any ellipse can be obtained by tweaking the values of a_x, a_y, ϕ_x, and ϕ_y. The orientation and eccentricity of the ellipse (function of those parameters) are one way to quantitatively characterise polarisation. This is a convenient picture to keep in the back of our mind, where we consider the electric field as a real vector oscillating in space. However, remember that light is most often described as a complex quantity (see Appendix A). Using complex numbers, another formalism exists to describe polarisation which is more convenient mathematically, although we completely lose the simple picture of a real oscillating field.

Using the complex form of the electric field, the time dependence can be factored out, and by also factoring out the norm of the vector $\rho = \sqrt{a_x^2 + a_y^2}$ we have

$$\boldsymbol{E} = e^{i\omega t} \begin{pmatrix} a_x e^{i\phi_x} \\ a_y e^{i\phi_y} \end{pmatrix} = \rho e^{i\omega t} \boldsymbol{u}, \tag{7.2}$$

where $\boldsymbol{u}$ is now a unit complex vector, called the Jones vector. The Jones vector is essentially "what is left" once we factor out the amplitude and time dependence[1]. We now have a new way to uniquely describe polarisation, which consists of a set of two complex numbers.

However, the Jones vector is not directly observable, because the electric field itself is not directly observable[2], only quadratic functions of the field are. We need to find a way to describe polarisation which only implies quadratic quantities. The four possible quadratic quantities that can be constructed from the two components of the field appear naturally in the coherency matrix, which is the covariance matrix of the field defined as

$$C = \left\langle \boldsymbol{E}\boldsymbol{E}^\dagger \right\rangle = \begin{pmatrix} \langle E_x E_x^* \rangle & \langle E_x E_y^* \rangle \\ \langle E_y E_x^* \rangle & \langle E_y E_y^* \rangle \end{pmatrix}, \tag{7.3}$$

where the brackets denote time averaging. For monochromatic light, we can express the coherency matrix directly from the the Jones vector, which takes the simpler form

[1] A global phase can also be factored out, the Jones vector is defined within a phase.

[2] At least in the optical domain, see Appendix A.

$C = \rho^2 \boldsymbol{u}\boldsymbol{u}^\dagger$. Sometimes the coherency matrix can be normalised to the intensity, in which case we have $C = \boldsymbol{u}\boldsymbol{u}^\dagger$ (this one will be used in the next section).

The coherency matrix is still complex, we need to convert it to more experimentally accessible quantities. This happens to be the case when decomposing C onto the basis of the four Pauli matrices, which form a complete basis for any hermitian complex 2×2 matrix. We then have the two following central relations

$$C = \sum_{n=0}^{3} \frac{1}{2} S_n \sigma_n \qquad S_n = \mathrm{Tr}(C\sigma_n), \tag{7.4}$$

where σ_n is the nth Pauli matrix, and Tr designates the trace. The first relation expresses the fact that C is a linear combination of the the Pauli matrices, with coefficients S_n (the $\frac{1}{2}$ is there by convention). The second relation gives the nth coefficient S_n by "projecting" C onto the corresponding Pauli matrix[3]. The coefficients form together a 4-vector $\boldsymbol{S}$ called the Stokes vector. Experimentally, S_0 is the intensity, and S_1 to S_3 are found by measuring the intensity after the appropriate combinations of polarisers and birefringent elements. This is the quadratic description of polarisation[4] that we shall use in this chapter. For fully polarised light, the norm of (S_1, S_2, S_3) is equal to S_0. It follows that $(S_1, S_2, S_3)/S_0$ can be represented geometrically as a point on the surface of the unit sphere, called the Poincaré sphere. Note that when the normalised coherency matrix is decomposed into the Pauli basis, S_0 is 1, and (S_1, S_2, S_3) directly gives the coordinates on the Poincaré sphere.

7.3 How does speckle depend on polarisation?

Consider a beam of monochromatic light with spatially constant polarisation of Jones vector $\boldsymbol{u}$. This beam is incident on a complex medium, and the diffused field is collected on a camera. Assuming the diffusion is linear, the Jones vector $\boldsymbol{u'}$ of the field at each point of the camera is a linear transformation of the original Jones vector

$$\boldsymbol{u'} = J\boldsymbol{u}, \tag{7.5}$$

where J is a 2×2 complex matrix, called a Jones matrix. We know how the Jones

[3]This unusual looking trace form follows from the properties of the Pauli matrices.

[4]Here I presented the Stokes vector as the result of a somewhat arbitrary construction. However there are deeper justifications for this particular decomposition of the coherency matrix. For example, $\boldsymbol{S}$ is a 4-vector of special relativity.

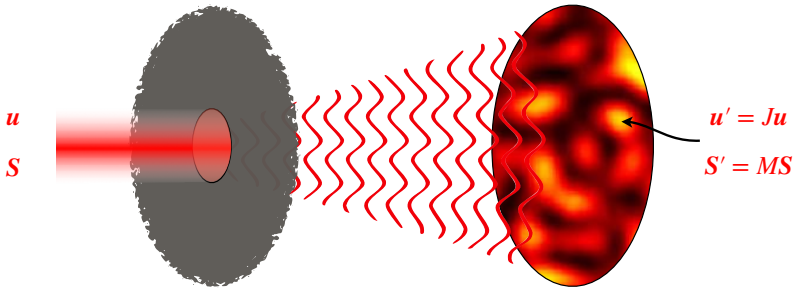

Figure 7.1: The input beam of Jones vector $\boldsymbol{u}$ and Stokes vector $\boldsymbol{S}$ is incident on a complex medium. The field observed at any given point of the observation plane has a transformed Jones vector $\boldsymbol{u'} = J\boldsymbol{u}$ and a transformed Stokes vector $\boldsymbol{S'} = M\boldsymbol{S}$, where J is a Jones matrix and M a Mueller matrix, which are both different for each point of the observation plane.

vector transforms, but how does the Stokes vector transform? Quite remarkably, it also transforms in a linear way, although the Stokes vector is a non-linear function of the Jones vector. This can be shown in the following way. The coherency matrix at a given point of the camera C' is

$$\begin{aligned} C' &= \boldsymbol{u'}\boldsymbol{u'}^{\dagger} && (7.6)\\ &= (J\boldsymbol{u})\,(J\boldsymbol{u})^{\dagger} && (7.7)\\ &= J\boldsymbol{u}\boldsymbol{u}^{\dagger}J^{\dagger} && (7.8)\\ &= JCJ^{\dagger}, && (7.9) \end{aligned}$$

where we use the normalised coherency matrix. Inserting (7.9) in the projection relation (7.4), and expanding C in terms of the initial Stokes vector $\boldsymbol{S}$, we have

$$\begin{aligned} S'_n &= \mathrm{Tr}\left(C'\sigma_n\right) && (7.10)\\ &= \mathrm{Tr}\left(JCJ^{\dagger}\sigma_n\right) && (7.11)\\ &= \mathrm{Tr}\left(J\sum_{m=0}^{3}\frac{1}{2}S_m\sigma_m J^{\dagger}\sigma_n\right) && (7.12)\\ &= \sum_{m=0}^{3}\frac{1}{2}\mathrm{Tr}\left(J\sigma_m J^{\dagger}\sigma_n\right)S_m && (7.13)\\ S'_n &= \sum_{m=0}^{3}M_{nm}S_m && (7.14)\\ \boldsymbol{S'} &= M\boldsymbol{S}, && (7.15) \end{aligned}$$

where M is called a Mueller matrix. When the Jones vector transforms via a matrix

product, the Stokes vector also transforms via a matrix product. This is a fairly widely known fact, any optical element (polarising, birefringent, or reflective) has its associated Jones and Mueller matrix, although the precise relation between the two as shown here is less known. Here we simply apply this to the case of our complex medium, between the input beam and any point of the camera, where each point of the camera has its own Jones and Mueller matrix. Remember that a camera only sees intensity, that is, the first component of $\boldsymbol{S'}$. Therefore most of the content of M is useless in our case, and we can just discard it. The intensity at one pixel is then simply the dot product of $\boldsymbol{S}$ with a vector (the first line of M), different for each pixel. Stacking the values of the intensity at different pixels in a column vector $\boldsymbol{I}$, we can write

$$\boldsymbol{I} = T\boldsymbol{S}, \tag{7.16}$$

where T is a transformation matrix. If we consider L pixels on the camera, $\boldsymbol{I}$ is a $L \times 1$ vector, T a $L \times 4$ matrix, and $\boldsymbol{S}$ a 4×1 vector. We now know how speckle depends on polarisation: the resulting speckle is a linear combination of four speckles, contained in the columns of T. The rest of this chapter is devoted to experimentally verify this linear relation, and exploit it as a way to measure the polarisation of the input beam.

7.4 Method

A first step in verifying Eq. (7.16) is to determine T. This can be done by applying many different polarisation states $\boldsymbol{S}$ and record the corresponding intensity pattern $\boldsymbol{I}$. If we stack all the different input Stokes vectors in a matrix S, one column for each state, T will apply separately on each column and give a matrix I that contains the output intensity patterns in columns. With N different states, we can write

$$I = TS, \tag{7.17}$$

where I is $L \times N$, T is still $L \times 4$, and S is $4 \times N$. The system written in this form contains $N \times L$ equations, while T contains $4 \times L$ unknowns. We therefore need at least $N = 4$ different states. We can then estimate T via a matrix inversion

$$T = IS^{-1}, \tag{7.18}$$

were S^{-1} is the pseudo-inverse of S. The pseudo-inverse has to be used as S is not square. In principle we could use only 4 states to determine T, but in practice a better estimation is found by using more states, due to the presence of noise (this is shown in section 7.6). With $N > 4$, Eq. (7.17) becomes an over-determined system, and solving by (7.18) is mathematically equivalent to find the solution for T that minimises the L2 norm $\|I - TS\|^2$, defined as $\|A\|^2 = \sum_{ij} A_{ij}^2$.

7.5 Verification of the linear relationship between polarisation and speckle

We verify the linear relationship (7.16) with the experimental setup described in Fig. 7.2. In order to find the T matrix, we need to be able to prepare a laser beam in different arbitrary polarisation states. An indirect way to achieve this is to make the polarisation state randomly varying in time and measure it using a commercial polarimeter. The random time variation is obtained by passing the beam through 3 successive waveplates (in order: quarter, half, and quarter-wave) and rotate the waveplates with sufficiently incommensurate speeds (respectively $5.77^\circ\,\mathrm{s}^{-1}$, $10.77^\circ\,\mathrm{s}^{-1}$, and $20.77^\circ\,\mathrm{s}^{-1}$) using motorised rotation stages (Thorlabs PRM1/MZ8). This ensures that the beam uniformly explores the Poincaré sphere over time and does not stay trapped in a period cycle. The beam is then split into two paths using a non-polarising beam splitter, one path goes to the commercial polarimeter (Thorlabs PAX1000IR1/M), the other path goes onto a rough surface (Thorlabs SM05CP2C) and the resulting speckle pattern is recorded on a camera (see full experimental details in section 2.4).

At regular intervals of 2 s, the reading of the polarimeter and the camera are recorded simultaneously. Using a total of 100 states, we make up our I and S matrices and find T by applying Eq. (7.18). The 100 states are shown on the Poincaré sphere in Fig. 7.3. So far this operation could be made even if the relation between I and S was nonlinear. To verify that it is indeed linear, we plot the value of the expected intensity TS vs the true value I, for every pixel of every images. This plot does show a cluster centred around the line $y = x$. The R^2 of the fit $y = x$ is 0.97, which means that the model explains 97% of the variance in the data. Eq. (7.16) is then a very good model of the process. To better visualise the distribution of the data points in the plane measured intensity vs expected intensity, a 2D histogram is shown in Fig. 7.3, as well as the fit with the identify function $y = x$.

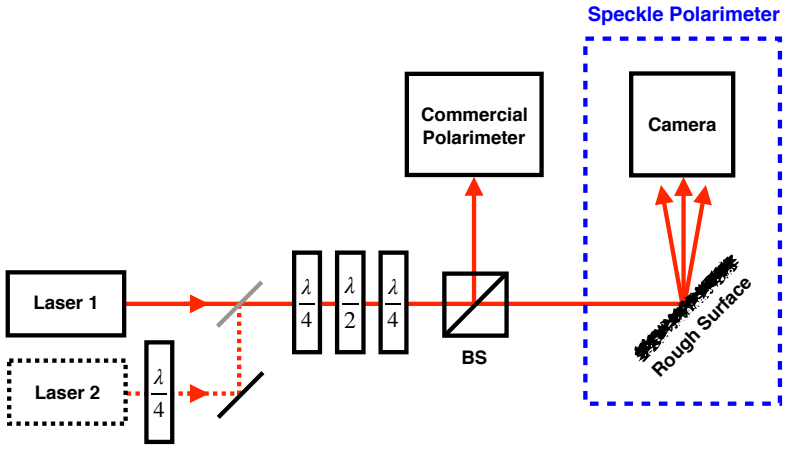

Figure 7.2: Experimental setup. A laser beam of randomly time-varying polarisation state is split into two paths, one goes to a commercial polarimeter, one goes onto a rough surface. The measurement of the polarimeter and the speckle pattern are recorded simultaneously. A second laser is introduced to test the ability to measure the polarisation state of two beams simultaneously.

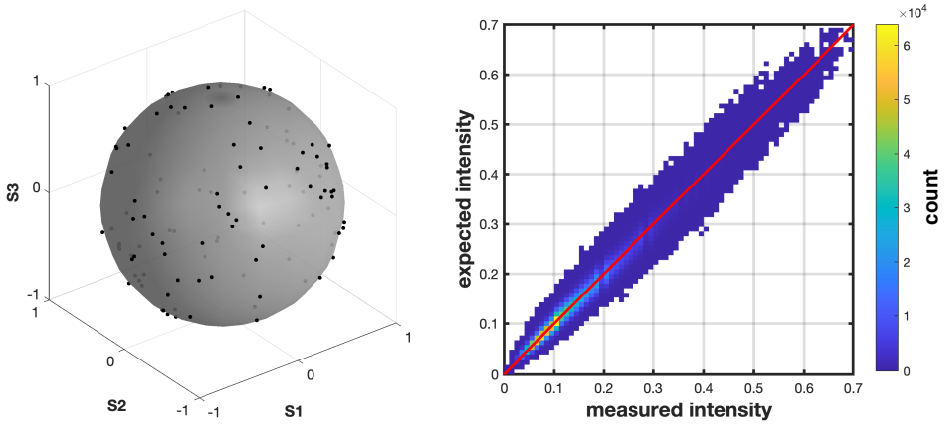

Figure 7.3: Left: the 100 polarisation states used to verify relation (7.16), represented on the Poincaré sphere. Right: 2D histogram of the measured intensity vs expected intensity, for all the pixels of all the images. The identity function $y = x$ (red) fits the data with an R^2 of 0.97.

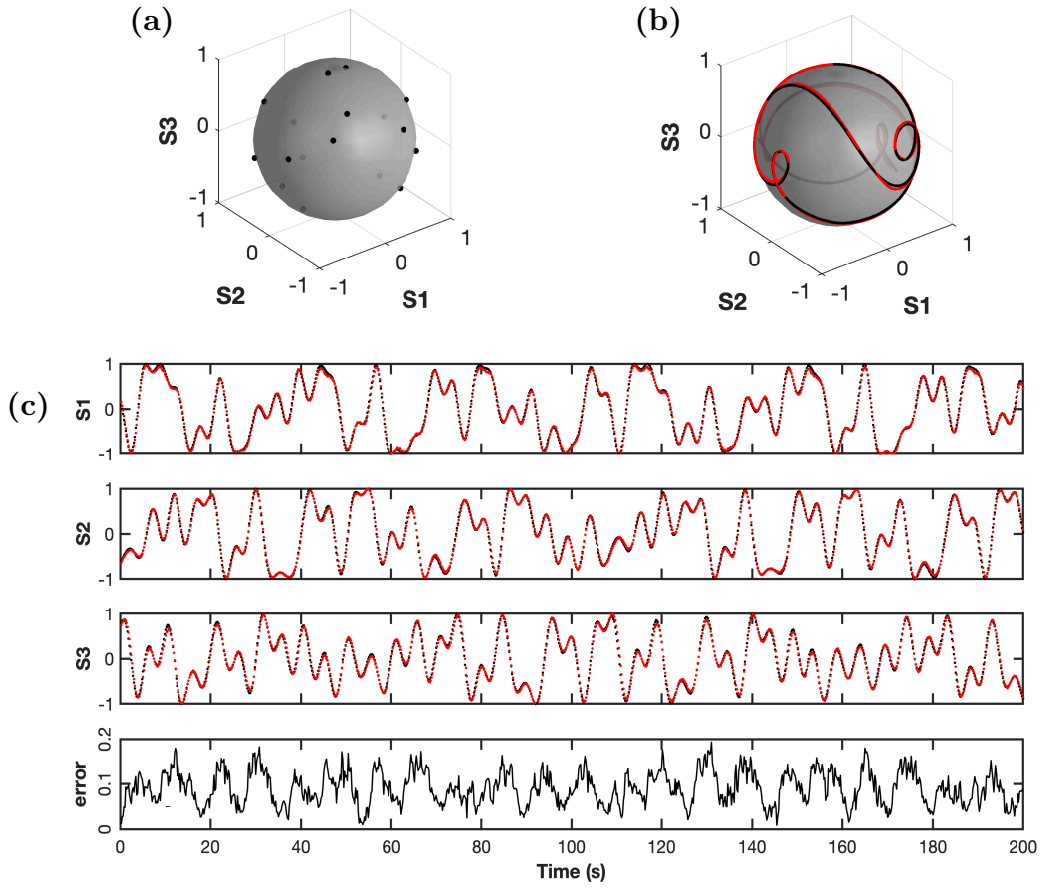

Figure 7.4: (a) The 17 training polarisation states, plotted on the Poincaré sphere. (b) Portion of the trajectory of the test beam on the Poincaré sphere, measured using the polarimeter (black), and retrieved using speckle patterns (red). (c) Time series of the Stokes parameters, measured using the polarimeter (black), and retrieved using speckle patterns (red). The error is also shown, expressed as the Euclidean distance between ground truth and estimation in (S_1, S_2, S_3)-space.

7.6 Using the linearity as a measurement tool

Once T is determined, we can use relation (7.16) in reverse, that is, determine the polarisation state $\boldsymbol{S}$ from the speckle image $\boldsymbol{I}$, via $\boldsymbol{S} = T^{-1}\boldsymbol{I}$. To verify this, we first find T using only 17 training states, with the same procedure as described above. Then, the randomly varying polarisation state and corresponding speckle is recorded every 0.2 s, in order to have more continuous measurements in time. For each speckle pattern, the Stokes vector is estimated and compared to measurement of the polarimeter. The results are shown in Fig. 7.4.

The error of the retrieval in Fig. 7.4 is shown as the Euclidean distance in (S_1, S_2, S_3)-space, between the data point measured by the polarimeter and that retrieved from the speckle. To extract an uncertainty on each individual Stokes pa-

rameter, we compute the standard deviation of the residuals, given by the difference between the measurement of the polarimeter and the estimation from the speckles. In the 200 s measurement of Fig. 7.4, the standard deviation is 0.05. For comparison, the resolution of the commercial polarimeter is 0.01. Note that the average value of the Euclidean distance plotted in Fig. 7.4 is larger than the uncertainty on each individual Stokes parameter as a quadratic sum is involved.

Two parameters determine the value of the uncertainty: image size, and the number of training states. We can investigate the influence of these parameters by repeating the same procedure with varying image size and number of training states. This is shown in Fig. 7.5. We see that, for a given image size, the uncertainty converges to its minimum value after about 15 training states. We also see that, for a given number of training states, the uncertainty converges to its minimum value after an image size of about 100×100. For that reason the measurements were made using 17 training states and a 100×100 image size, where the uncertainty is 0.05. The main sources of noise are camera noise, which is dominated by the effect of photon shot noise, and lack of synchronisation between the camera and the polarimeter.

Note that the observed error is of an interesting kind here, that we could qualify as globally random but locally systematic. Indeed, looking at panel (c) of Fig. 7.4, we see that the estimated stokes parameters show a small deviation from the true ones, which is relatively constant at short time scales, and can then be seen as a local systematic error. However this deviation itself varies around zero in time, such that it can also be considered globally random. In fact, the plot of the error in Fig. 7.4 seems to be made of a smooth component superposed to a random component. The smooth component is most likely the drifting local deviation just discussed (related to the imperfect camera-polarimeter synchronisation) and the random component most likely reflects camera noise. This is consistent with the fact that the uncertainty converged to a finite value: increasing image size reduced the random component, but a lower limit is imposed by the smooth component.

It is worth pointing out that what is retrieved from the speckle patterns is the polarisation of the light that is incident upon the polarimeter, which is not necessarily the same as that of the light incident upon the diffuser. These may differ due to the reflection in the beam splitter, and are linearly related by the Mueller matrix associated with the reflection in the beam splitter. For any unknown beam, the polarisation retrieved from the speckle patterns is the one that would be measured by the polarimeter. If this is of any importance in a given application, for example if we need to determine the polarisation of the light incident upon the diffuser, we

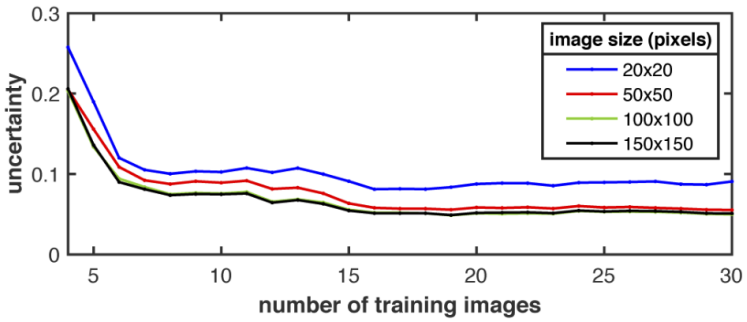

Figure 7.5: Measurement uncertainty. The uncertainty on the Stokes parameters is given by the standard deviation of the residuals. It is shown as a function of the number of training images (four being the minimum required), for different image sizes. We see that the uncertainty reaches a minimum of 0.05 after about 15 training images and an image size of 100×100 pixels.

would have to determine the Mueller matrix of the beam splitter. That task would be strictly analogous to what is done in the method section, where the unknown matrix T would be the Mueller matrix of the beam splitter, and the two linearly related vectors would be the polarisation states of the two paths.

7.7 Multiplexing

An advantage of speckle patterns is that they allow multiplexing, that is, measuring the polarisation state of multiple laser beams from one single image. In this section we investigate this idea and implement it experimentally. Consider k laser beams originating from different sources, incident on a rough surface. The k corresponding speckle patterns superpose additively (without interference) on the camera. As the polarisation state of each individual beam is linearly related to its corresponding speckle pattern, the sum of all the speckle patterns is linearly related to the Stokes parameters of each laser beam taken together in a single vector. This can be described by a generalised form of (7.16), where $\boldsymbol{S}$ is now a $4k \times 1$ vector containing the Stokes vectors of each beam. The image vector $\boldsymbol{I}$ is still $L \times 1$ and T is now a $L \times 4k$ matrix. We implement this in the case of two laser beams. We add a second laser (of same wavelength and power), which joins the path before passing through the 3 waveplates (see Fig. 7.2). This second laser beam undergoes the same transformation as the first beam, however we ensure that it starts with a different initial polarisation state, so that the two output polarisations are different. We then have two laser beams of different randomly varying polarisation state impinging on the rough surface. From this we apply the same procedure as described above for one beam, where we also use 17 training states, and use subsequent states to compare

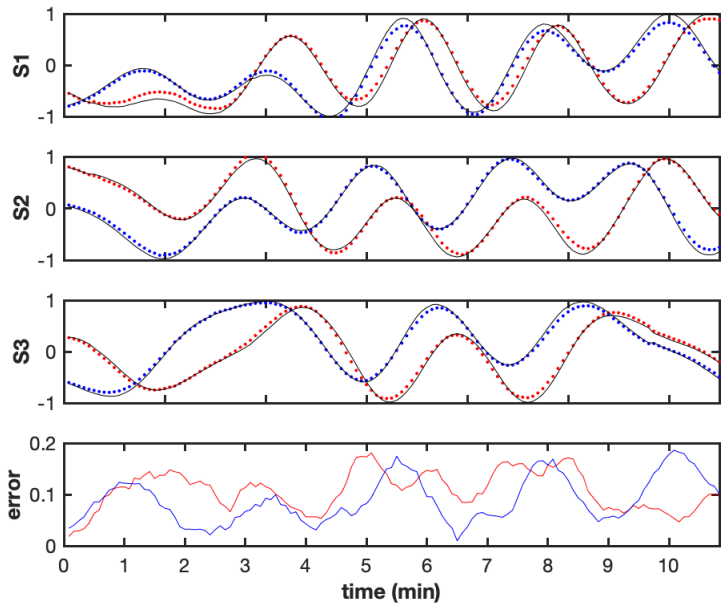

Figure 7.6: Two-beam polarisation measurement. The Stokes parameters S_1 to S_3 are given as a function of time, measured by the commercial polarimeter (black) and retrieved from the speckle patterns (red and blue, one for each beam). The estimation was performed using 150×150-pixel images and 17 training states. The error on the estimation is also shown as the Euclidean distance in (S_1, S_2, S_3)-space for each beam.

the estimation and the polarimeter's measurement. The results are shown in Fig. 7.6. We also determine the uncertainty as a function of image size and number of training states. We find again that the uncertainty converges to a minimum after an image size of 100×100 and 15 training states. Note that in this setup, in order to measure both polarisation states with the commercial polarimeter, the beams had to be blocked sequentially so as to have only one beam entering the polarimeter at once. This was done using home-made voltage controlled shutters. This slowed down the process, this is why the measurement period is longer in Fig. 7.6 and contains fewer oscillations on a longer time.

7.8 Conclusion

In this chapter, we analytically proved and experimentally verified the linearity that exists between the Stokes vector of laser light and the speckle pattern it produces. Through this linearity, the Stokes parameters formalism proves to be more fundamental than the other descriptions of polarisation (in a very analogous way to what is found in Mueller calculus).

We exploited this linearity as a metrological tool to measure the polarisation of a

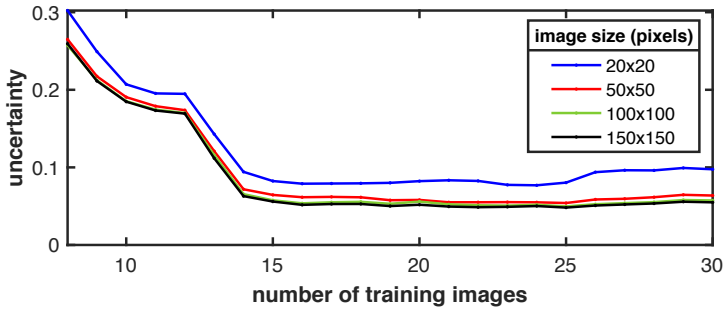

Figure 7.7: Measurement uncertainty for two beams. The uncertainty is given by the standard deviation of the residuals. It is shown as a function of the number of training images (eight being the minimum required), for different image sizes ranging from 20×20 to 150×150 pixels. Here the uncertainty also reaches a minimum of 0.05 after about 15 training images.

single laser beam, and two laser beams simultaneously (multiplexing). The method relies on a set of training speckle images obtained for known polarisation states, which are then used to infer any unknown polarisation state via simple linear algebra. It is important to note that the method is not one based on first principles, and needs a training stage involving a pre-calibrated instrument. The metrological prospects of such a method may be limited, but may still have some value in particular situations. The end result of the procedure is the transfer of the measurement process from the polarimeter to the camera, the knowledge being passed on during the determination of the matrix T. By doing so, we benefit from the advantages of the camera that the polarimeter might not possess. Such advantages are higher acquisition speed, regular sampling, and multiplexing. For example, the polarimeter used in this particular study can theoretically achieve a sampling rate of 400 Hz, but is limited to 110 Hz in practice, with an irregular sampling. In the same conditions, our camera could record at a sampling rate of 5000 Hz at regular sampling.

The camera has clear advantages over the commercial polarimeter, but this has to be compared to other standard polarimetry methods. Standard polarimetry methods for monochromatic laser beams involve measuring the intensity of the test beam after going through 4 controlled modifications of polarisation, using birefringent and polarising elements [105]. Each element applies its own Mueller matrix, and a number of 4 measurements closes the system and allows one to extract the Stokes parameters from first principles. However the intensity is typically measured using photodiodes, which obviously surpass the speed capacity of cameras. There may still be some use in cameras in the context of multiplexing. Indeed, in the standard scheme just described, measuring the polarisation state of k laser beams would require $4k$ measurements after a combination of birefringent and polarising elements, which would naturally increase in complexity and become less easily computable

from first principles. The camera on the other hand already contains by design a large number of measurement points, each with a different Mueller matrix, and does not require any hardware modification for a different value of k. However in practice this method would be limited by the speckle contrast reduction as more beams are added, which in turn reduces the efficiency of the polarisation retrieval (as the image becomes more and more uniform). Note that standard polarimetry could in fact be used for more than one beam, if we sequentially launch each separate beam into the apparatus (by sequential blocking for example), but then the measurement is no longer instantaneous, as it is with a camera.

Chapter 8

The text of this chapter has been embargoed at the author's request.

Conclusion

In this thesis, we tackled various aspects of speckle patterns using the three ways of physical sciences: theoretical models, numerical simulations, and experiments. We arrived at a number of results that we shall summarise here, along with perspectives for the future.

We found a general expression (Eq. 3.14) that predicts the amount of change in a speckle pattern resulting from an arbitrary transformation, in the particular case of speckle patterns produced by an integrating sphere. We experimentally tested this model in three cases: wavelength variation, refractive index variation, and displacement. We found very good agreement within experimental errors in each case. Only the case of transverse displacement showed a systematic deviation from the model. We could show analytically that transverse displacement is a special case of transformation which is most sensitive to the assumptions behind the model, in particular the Lambertian reflectance of the inner surface. Using an approach where the deviation from the Lambertian reflectance is parametrised by two variables, we could explain the observations, using these variables as free parameters. More analytical work on this matter might lead to new ways of investigating some reflectance properties of surfaces.

We used the case of a wavelength variation to validate our model. We predicted a Lorentzian similarity profile as a function of wavelength variation, and found the relevant parameters that determine the width of the profile: reflectivity and radius. We experimentally verified this functional form, and its parameters, and found excellent agreement with no free parameter. We found that this approach, taken in reverse, can be used to measure reflectivity by measuring the HWHM of the similarity curve, knowing the radius and wavelength. Finally, we analytically showed that the speckle patterns produced by an integrating sphere are about 19000 times more sensitive than those produced by a typical multimode fibre of the same size.

We exploited the exceptional sensitivity of the speckle patterns produced by an integrating sphere in a metrological perspective. We showed that the multiple

scattering of light, intrinsic to that geometry, dramatically increases the performance of speckle-based methods. We showed this in the particular case of refractive index variation measurement where we could measure variations of the order of 10^{-9} (or 3 orders of magnitude improvement compared to previous methods), and in the case of displacement measurement where we could measure displacements of the order of 10^{-11} m (or 2 orders of magnitude improvement compared to previous methods).

Expression 3.14 is valid for an effect that changes only the phase of light along its propagation throughout the sphere. This is the case of all effects investigated experimentally in this thesis. But we also considered effects that change the two other properties of light: amplitude and polarisation. In the case of amplitude, we could give an explicit result, analog to 3.14. In the case of polarisation however, no explicit result was found, but we gave a few hints for future work. We also speculated on the speckle patterns produced by another kind of wave: electron waves, where the phase considered is that of the Aharonov-Bohm effect. We found an explicit expression for the similarity of the electron wave speckle pattern as a function of the magnetic field.

On the other hand, we elucidated how multiple scattering only benefits speckle metrology for certain measurands: those which involve a path-dependent phase. In general, for a measurand which changes only the input field, a single-plane scatterer yields the same sensitivity to a change in the measurand as a multiple scattering geometry (like a multi-mode fibre or an integrating sphere). Path-dependent changes correspond to changes in the scatterer, while path-independent changes correspond to changes in the input light (with the exception of wavelength change, which is path-dependent).

We also explored the relation between speckle patterns and polarisation, where we proved that the speckle patterns produced by an input laser beam is linearly related to its Stokes parameters. From this relation we developed a metrology technique which retrieves the polarisation states of a test beam by comparing it to an arbitrary set of reference polarisation states, via simple linear algebra. We also described an extension of this method to the case of multiple beams (multiplexing), allowing the determination of the polarisation state of multiple beams simultaneously. Multiplexing is the main benefit of this method, as it can be difficult to achieve in other methods based on first principles.

Finally, we developed a number of methods for the design of speckle patterns with custom properties, using light shaping. We developed a general approach to answer the following problem: what input field should be chosen so that the resulting speckle pattern is maximally/minimally sensitive to some parameter of interest?

Using either the similarity or the distance as a measure of sensitivity, this led us to 4 answers. One of those (minimising sensitivity using the similarity) corresponds to the well known principal modes (eigenvectors of the Wigner-Smith operator). We tested all these numerically, and obtained encouraging results. Most notably, we managed to increase sensitivity by a factor of 40, and we found a particular input field that increases sensitivity only in a very narrow region around a certain target value of the parameter of interest. The experimental verification of those results will be the natural continuation for future work.

Bibliography

[1] T. Maiman. Stimulated optical radiation in ruby. *Nature*, 187:493–494, 1960.

[2] J. D. Rigden and E. I. Gordon. The granularity of scattered optical maser light. *Proc. IRE*, 50:2367–2368, 1962.

[3] BM Oliver. Sparkling spots and random diffraction. *Proceedings of the IEEE*, 51(1):220–221, 1963.

[4] Robert V. Langmuir. Scattering of laser light. *Applied Physics Letters*, 2(2):29–30, 1963.

[5] Eugenio R Mendez. Laser and stellar speckle. *Science Progress (1933-)*, pages 365–380, 1987.

[6] René Dändliker. The story of speckles in interferometry. In Pierre Jacquot and Jean-Marc Fournier, editors, *Interferometry in Speckle Light*, pages 3–10, Berlin, Heidelberg, 2000. Springer Berlin Heidelberg.

[7] Yimin Gan and Wolfgang Steinchen. *Speckle Methods*, pages 655–674. Springer US, Boston, MA, 2008.

[8] Speckle (interference). https://en.wikipedia.org/wiki/speckle_(interference)#speckle_pattern. Accessed: 2022-06-24.

[9] M. Françon. *Laser speckle and related phenomena*, chapter Information Processing Using Speckle Patterns. Springer, 1975.

[10] J. W. Goodman. *Speckle Phenomena in Optics*. Roberts and Company Publishers, 2007.

[11] Isaac Newton. *Opticks, or, a treatise of the reflections, refractions, inflections & colours of light*. Courier Corporation, 1952.

[12] Néstor Gustavo Gaggioli and Juan Antonio Pomarico. *The speckle phenomenon*. CRC Press, 2009.

[13] Maurice Françon. *Laser Speckle and Applications in Optics*. Academic Press, 1979.

[14] P Hariharan. Speckle patterns: a historical retrospect. *Optica Acta: International Journal of Optics*, 19(9):791–793, 1972.

[15] DB Barker and ME Fourney. Measuring fluid velocities with speckle patterns. *Opt. Letters*, 1(4):135–137, 1977.

[16] Zeev Zalevsky, Yevgeny Beiderman, Israel Margalit, Shimshon Gingold, Mina Teicher, Vicente Mico, and Javier Garcia. Simultaneous remote extraction of multiple speech sources and heart beats from secondary speckles pattern. *Opt. Express*, 17(24):21566–21580, 2009.

[17] Yevgeny Beiderman, Israel Horovitz, Natanel Burshtein, Mina Teicher, Javier Garcia, Vicente Mico, and Zeev Zalevsky. Remote estimation of blood pulse pressure via temporal tracking of reflected secondary speckles pattern. *Journal of biomedical optics*, 15(6):061707, 2010.

[18] E Archbold and AE Ennos. Two-dimensional vibrations analysed by speckle photography. *Optics & Laser Technology*, 7(1):17–21, 1975.

[19] Silvio Bianchi. Vibration detection by observation of speckle patterns. *Applied Optics*, 53(5):931–936, 2014.

[20] David A Boas and Andrew K Dunn. Laser speckle contrast imaging in biomedical optics. *Journal of Biomedical Optics*, 15(1):011109, 2010.

[21] David Briers, Donald D Duncan, Evan R Hirst, Sean J Kirkpatrick, Marcus Larsson, Wiendelt Steenbergen, Tomas Stromberg, and Oliver B Thompson. Laser speckle contrast imaging: theoretical and practical limitations. *Journal of Biomedical Optics*, 18(6):066018, 2013.

[22] Brandon Redding and Hui Cao. Using a multimode fiber as a high-resolution, low-loss spectrometer. *Opt. Letters*, 37(16):3384–3386, 2012.

[23] Brandon Redding, Seng Fatt Liew, Raktim Sarma, and Hui Cao. Compact spectrometer based on a disordered photonic chip. *Nat. Photonics*, 7(9):746, 2013.

[24] Brandon Redding, Sebastien M Popoff, and Hui Cao. All-fiber spectrometer based on speckle pattern reconstruction. *Opt. Express*, 21(5):6584–6600, 2013.

[25] Hui Cao. Perspective on speckle spectrometers. *J. Opt.*, 19:060402, 2017.

[26] Lukasz Lasyk, Michał Łukomski, and Łukasz Bratasz. Simple digital speckle pattern interferometer (dspi) for investigation of art objects. *Optica Applicata*, 41(3):687–700, 2011.

[27] Thomas OH Charrett, Yashwanth K Bandari, Florent Michel, Jialuo Ding, Stewart W Williams, and Ralph P Tatam. A non-contact laser speckle sensor for the measurement of robotic tool speed. *Robotics and Computer-Integrated Manufacturing*, 53:187–196, 2018.

[28] Daniel Francis, Thomas OH Charrett, L Waugh, and Ralph P Tatam. Objective speckle velocimetry for autonomous vehicle odometry. *Applied optics*, 51(16):3478–3490, 2012.

[29] David L Fried. Optical resolution through a randomly inhomogeneous medium for very long and very short exposures. *JOSA*, 56(10):1372–1379, 1966.

[30] J Christopher Dainty. Stellar speckle interferometry. In *Laser speckle and related phenomena*, pages 255–280. Springer, 1975.

[31] European Machine Vision Association et al. Standard for characterization of image sensors and cameras. *EMVA Standard*, 1288, 2010.

[32] Morgan Facchin, Kishan Dholakia, and Graham David Bruce. Wavelength sensitivity of the speckle patterns produced by an integrating sphere. *Journal of Physics: Photonics*, 3:035005, 2021.

[33] Glenn D. Boreman, Yuankun Sun, and Anthony B. James. Generation of laser speckle with an integrating sphere. *Optical Engineering*, 29(4):339 – 342, 1990.

[34] Valerie E Anderson, Nigel P Fox, and David H Nettleton. Highly stable, monochromatic and tunable optical radiation source and its application to high accuracy spectrophotometry. *Applied Optics*, 31(4):536–545, 1992.

[35] Jane Hodgkinson, Dackson Masiyano, and Ralph P Tatam. Gas cells for tunable diode laser absorption spectroscopy employing optical diffusers. part 1: single and dual pass cells. *Applied Physics B*, 100(2):291–302, 2010.

[36] Dackson Masiyano, Jane Hodgkinson, and Ralph P Tatam. Gas cells for tunable diode laser absorption spectroscopy employing optical diffusers. part 2: Integrating spheres. *Applied Physics B*, 100(2):303–312, 2010.

[37] Antonio Manuel Pozo and Manuel Rubiño. Optical characterization of ophthalmic lenses by means of modulation transfer function determination from a laser speckle pattern. *Applied optics*, 44(36):7744–7748, 2005.

[38] Alicia Fernández-Oliveras, Antonio M Pozo, and Manuel Rubiño. Speckle-based modulation transfer function measurements for comparative evaluation of ccd and cmos detector arrays. *Optical review*, 20(1):41–49, 2013.

[39] N K Metzger, R Spesyvtsev, G D Bruce, B Miller, G T Maker, G Malcolm, M Mazilu, and K Dholakia. Harnessing speckle for a sub-femtometre resolved broadband wavemeter and laser stabilization. *Nature Communications*, 8:15610, 2017.

[40] Laura O'Donnell, Kishan Dholakia, and Graham D Bruce. High speed determination of laser wavelength using poincaré descriptors of speckle. *Opt. Communications*, 459:124906, 2020.

[41] Roopam K Gupta, Graham D Bruce, Simon J Powis, and Kishan Dholakia. Deep learning enabled laser speckle wavemeter with a high dynamic range. *Laser & Photonics Reviews*, 14(9):2000120, 2020.

[42] A Dávila and JA Rayas. Single-shot phase detection in a speckle wavemeter for the measurement of femtometric wavelength change. *Optics and Lasers in Engineering*, 125:105856, 2020.

[43] Jane Hodgkinson, Dackson Masiyano, and Ralph P Tatam. Using integrating spheres as absorption cells: path-length distribution and application of beer's law. *Applied Optics*, 48(30):5748–5758, 2009.

[44] KF Carr. Integrating sphere theory and applications part i: integrating sphere theory and design. *Surface coatings international*, 80(8):380–385, 1997.

[45] J. W. Goodman. *Statistical Optics*. Wiley Classics Library, 2000.

[46] Edward S. Fry, Joe Musser, George W. Kattawar, and Peng-Wang Zhai. Integrating cavities: temporal response. *Appl. Opt.*, 45(36):9053–9065, Dec 2006.

[47] David Berengut. Random chords of a sphere. Technical report, Stanford University Department of Statistics, 1972.

[48] Panagiotis Sidiropoulos. N-sphere chord length distribution. *arXiv preprint arXiv:1411.5639*, 2014.

[49] PAM Dirac. Approximate rate of neutron multiplication for a solid of arbitrary shape and uniform density. *Declassified British Report MS-D-5, Part I*, 1943.

[50] Richard P Feynman, Robert B Leighton, and Matthew Sands. *The Feynman lectures on physics, The new millennium edition*, volume 1, chapter 23-1. Basic books, 2011.

[51] Harold J Metcalf and Peter Van der Straten. Laser cooling and trapping of neutral atoms. *The Optics Encyclopedia: Basic Foundations and Practical Applications*, 2007.

[52] Maumita Chakrabarti, Michael Linde Jakobsen, and Steen G Hanson. Speckle-based spectrometer. *Opt. Letters*, 40(14):3264–3267, 2015.

[53] M Mazilu, T Vettenburg, A Di Falco, and K Dholakia. Random super-prism wavelength meter. *Opt. Letters*, 39:96–99, 2014.

[54] Yangyang Wan, Shuai Wang, Xinyu Fan, Zhaopeng Zhang, and Zuyuan He. High-resolution wavemeter using rayleigh speckle obtained by optical time domain reflectometry. *Opt. Letters*, 45(4):799–802, 2020.

[55] Graham D. Bruce, Laura O'Donnell, Mingzhou Chen, Morgan Facchin, and Kishan Dholakia. Femtometer-resolved simultaneous measurement of multiple laser wavelengths in a speckle wavemeter. *Opt. Letters*, 45(7):1926–1929, Apr 2020.

[56] Graham D Bruce, Laura O'Donnell, Mingzhou Chen, and Kishan Dholakia. Overcoming the speckle correlation limit to achieve a fiber wavemeter with attometer resolution. *Opt. Letters*, 44(6):1367–1370, 2019.

[57] Steen G Hanson, Michael Linde Jakobsen, and Maumita Chakrabarti. The dynamic speckle-based wavemeter. In *Speckle 2018: VII International Conference on Speckle Metrology*, volume 10834, pages 620–625. SPIE, 2018.

[58] E. G. Rawson, J. W. Goodman, and R. E. Norton. Frequency dependence of modal noise in multimode optical fibers. *J. Opt. Soc. Am.*, 70:968–976, 1980.

[59] Noel H Wan, Fan Meng, Tim Schröder, Ren-Jye Shiue, Edward H Chen, and Dirk Englund. High-resolution optical spectroscopy using multimode interference in a compact tapered fibre. *Nature Communications*, 6:7762, 2015.

[60] Brandon Redding and Hui Cao. Using a multimode fiber as a high-resolution, low-loss spectrometer. *Opt. Letters*, 37(16):3384–3386, 2012.

[61] Brandon Redding, Mansoor Alam, Martin Seifert, and Hui Cao. High-resolution and broadband all-fiber spectrometers. *Optica*, 1(3):175–180, Sep 2014.

[62] Seng Fatt Liew, Brandon Redding, Michael A Choma, Hemant D Tagare, and Hui Cao. Broadband multimode fiber spectrometer. *Opt. Letters*, 41(9):2029–2032, 2016.

[63] Brandon Redding, Seng Fatt Liew, Raktim Sarma, and Hui Cao. Compact spectrometer based on a disordered photonic chip. *Nat. Photonics*, 7(9):746, 2013.

[64] Matthias C Velsink, Zhouping Lyu, Pepijn WH Pinkse, and Lyubov V Amitonova. Comparison of round-and square-core fibers for sensing, imaging and spectroscopy. *arXiv preprint arXiv:2101.07153*, 2021.

[65] Nur Ismail, Cristine Calil Kores, Dimitri Geskus, and Markus Pollnau. Fabry-pérot resonator: spectral line shapes, generic and related airy distributions, linewidths, finesses, and performance at low or frequency-dependent reflectivity. *Opt. Express*, 24(15):16366–16389, Jul 2016.

[66] M. Facchin, G.D. Bruce, and K. Dholakia. Measurement of variations in gas refractive index with 10^{-9} resolution using laser speckle. *ACS Photonics*, 9:830–836, 2022.

[67] I. Silander, C. Forssén, J. Zakrisson, M. Zelan, and O. Axner. Invar-based refractometer for pressure assessments. *Opt. Lett.*, 45(9):2652–2655, May 2020.

[68] E. A. Abbondanzieri, W. J. Greenleaf, J. W. Shaevitz, R. Landick, and S. M Block. Direct observation of base-pair stepping by RNA polymerase. *Nature*, 438(7067):460–465, 2005.

[69] H. Fang and P. Juncar. A new simple compact refractometer applied to measurements of air density fluctuations. *Rev. Sci. Instrum.*, 70(7):3160–3166, 1999.

[70] N. Khélifa, H. Fang, J. Xu, P. Juncar, and M. Himbert. Refractometer for tracking changes in the refractive index of air near 780 nm. *Appl. Opt.*, 37(1):156–161, Jan 1998.

[71] O. Kruger and N. Chetty. Robust air refractometer for accurate compensation of the refractive index of air in everyday use. *Appl. Opt.*, 55(32):9118–9122, Nov 2016.

[72] H. Chen, X. Hu, M. He, P. Ren, C. Zhang, and H. Qu. Ultrasensitive gas refractometer using capillary-based Mach–Zehnder interferometer. *Sensors*, 20(4):1191, 2020.

[73] M. Quan, J. Tian, and Y. Yao. Ultra-high sensitivity fabry-pérot interferometer gas refractive index fiber sensor based on photonic crystal fiber and vernier effect. *Opt. Lett.*, 40(21):4891–4894, Nov 2015.

[74] Z. Zhang, J. He, B. Du, K. Guo, and Y. Wang. Highly sensitive gas refractive index sensor based on hollow-core photonic bandgap fiber. *Opt. Express*, 27(21):29649–29658, Oct 2019.

[75] L. Li, Y. Liang, J. Guang, W. Cui, X. Zhang, J.-F. Masson, and W. Peng. Dual Kretschmann and Otto configuration fiber surface plasmon resonance biosensor. *Opt. Express*, 25(22):26950–26957, Oct 2017.

[76] A. Urrutia, I. Del Villar, P. Zubiate, and C. R. Zamarreño. A comprehensive review of optical fiber refractometers: Toward a standard comparative criterion. *Laser Photonics Rev.*, 13(11):1900094, 2019.

[77] D. Conteduca, I. Barth, G. Pitruzzello, C. P. Reardon, E. R. Martins, and T. F. Krauss. Dielectric nanohole array metasurface for high-resolution near-field sensing and imaging. *Nat. Commun.*, 12(1):3293, 2021.

[78] U Köpf. Application of speckling for measuring the deflection of laser light by phase objects. *Opt. Commun.*, 5(5):347–350, 1972.

[79] S. Debrus, M. Françon, C. P. Grover, M. May, and M. L. Roblin. Ground glass differential interferometer. *Appl. Opt.*, 11(4):853–857, Apr 1972.

[80] J. Lapsien and D. Meiners. Digital speckle techniques for measuring light deflection profiles of inhomogeneous phase objects. *Appl. Opt.*, 36(28):7180–7187, Oct 1997.

[81] C. Guo, D. Li, D. P. Kelly, H. Li, J. P. Ryle, and J. T. Sheridan. Measuring refractive index of glass by using speckle. *Appl. Opt.*, 57(22):E205–E217, Aug 2018.

[82] V. Trivedi, S. Mahajan, M. Joglekar, V. Chhaniwal, Z. Zalevsky, B. Javidi, and A. Anand. 3D printed hand-held refractometer based on laser speckle correlation. *Opt. Lasers Eng.*, 118:7–13, 2019.

[83] V. Tran, S. K. Sahoo, D. Wang, and C. Dang. Utilizing multiple scattering effect for highly sensitive optical refractive index sensing. *Sens. Actuators, A*, 301:111776, 2020.

[84] J. H. Gladstone and T. P. Dale. XIV. Researches on the refraction, dispersion, and sensitiveness of liquids. *Philos. Trans. R. Soc. London*, (153):317–343, 1863.

[85] P. E. Ciddor. Refractive index of air: new equations for the visible and near infrared. *Appl. Opt.*, 35(9):1566–1573, 1996.

[86] Morgan Facchin, Graham David Bruce, and Kishan Dholakia. Measuring picometre-level displacements using speckle patterns produced by an integrating sphere. *arXiv preprint arXiv:2110.15939*, 2021.

[87] G. Berkovic and E. Shafir. Optical methods for distance and displacement measurements. *Advances in Optics and Photonics*, 4:441–471, 2012.

[88] P.J. De Groot. A review of selected topics in interferometric optical metrology. *Reports on Progress in Physics*, 82:056101, 2019.

[89] G.H. Yuan and N.I. Zheludev. Detecting nanometric displacements with optical ruler metrology. *Science*, 364:771–775, 2019.

[90] Raouf Barboza, Amin Babazadeh, Lorenzo Marrucci, Filippo Cardano, Corrado de Lisio, and Vincenzo D'Ambrosio. Ultra-sensitive measurement of transverse displacements with linear photonic gears. *Nature communications*, 13(1):1–5, 2022.

[91] Isaac Freund, Michael Rosenbluh, and Shechao Feng. Memory effects in propagation of optical waves through disordered media. *Phys. Rev. Lett.*, 61:2328–2331, Nov 1988.

[92] E. Archbold, J.M. Burch, and A.E. Ennos. Recording of in-plane surface displacement by double-exposure speckle photography. *Optica Acta: International Journal of Optics*, 17(12):883–898, 1970.

[93] Bjarke Rose, Husain Imam, Steen G Hanson, Harold T Yura, and Rene S Hansen. Laser-speckle angular-displacement sensor: theoretical and experimental study. *Applied optics*, 37(11):2119–2129, 1998.

[94] J.A. Leendertz. Interferometric displacement measurement on scattering surfaces utilizing speckle effect. *Journal of Physics E: Scientific Instruments*, 3:214, 1970.

[95] L. Yang, X. Xie, L. Zhu, S. Wu, and Y. Wang. Review of electronic speckle pattern interferometry (ESPI) for three dimensional displacement measurement. *Chinese Journal of Mechanical Engineering*, 27:1–13, 2014.

[96] Wei Wang, Tomoaki Yokozeki, Reika Ishijima, Mitsuo Takeda, and Steen G Hanson. Optical vortex metrology based on the core structures of phase singularities in laguerre-gauss transform of a speckle pattern. *Opt. Express*, 14(22):10195–10206, 2006.

[97] Wei Wang, Tomoaki Yokozeki, Reika Ishijima, Atsushi Wada, Yoko Miyamoto, Mitsuo Takeda, and Steen G Hanson. Optical vortex metrology for nanometric speckle displacement measurement. *Opt. Express*, 14(1):120–127, 2006.

[98] Martin P Levesque and Maria Dissanska. Correction of the calibration measurement by taking into account the spectralon spectro-polarimetric brdf model. In *Reflection, Scattering, and Diffraction from Surfaces VI*, volume 10750, pages 60–70. SPIE, 2018.

[99] M.T. Cone, J.A. Musser, E. Figueroa, J.D. Mason, and E.S. Fry. Diffuse reflecting material for integrating cavity spectroscopy, including ring-down spectroscopy. *Appl. Opt.*, 54:334–346, 2015.

[100] Morgan Facchin, Graham D Bruce, and Kishan Dholakia. Speckle-based determination of the polarisation state of single and multiple laser beams. *OSA Continuum*, 3(5):1302–1313, 2020.

[101] Isaac Freund. Stokes-vector reconstruction. *Opt. Letters*, 15(24):1425–1427, 1990.

[102] Thomas Kohlgraf-Owens and Aristide Dogariu. Finding the field transfer matrix of scattering media. *Opt. Express*, 16(17):13225–13232, 2008.

[103] Thomas Kohlgraf-Owens and Aristide Dogariu. Spatially resolved scattering polarimeter. *Opt. Letters*, 34(9):1321–1323, 2009.

[104] Thomas W Kohlgraf-Owens and Aristide Dogariu. Transmission matrices of random media: means for spectral polarimetric measurements. *Opt. Letters*, 35(13):2236–2238, 2010.

[105] Beth Schaefer, Edward Collett, Robert Smyth, Daniel Barrett, and Beth Fraher. Measuring the stokes polarization parameters. *American Journal of Physics*, 75(2):163–168, 2007.

[106] Ivo M Vellekoop and AP Mosk. Focusing coherent light through opaque strongly scattering media. *Opt. Letters*, 32(16):2309–2311, 2007.

[107] Ivo Micha Vellekoop, EG Van Putten, A Lagendijk, and AP Mosk. Demixing light paths inside disordered metamaterials. *Opt. express*, 16(1):67–80, 2008.

[108] Ivo Micha Vellekoop and AP Mosk. Universal optimal transmission of light through disordered materials. *Physical review letters*, 101(12):120601, 2008.

[109] I. M. Vellekoop, A. Lagendijk, and A. P. Mosk. Exploiting disorder for perfect focusing. *Nat. Photonics*, 4:320–322, 2010.

[110] Hasan Yılmaz, Matthias Kühmayer, Chia Wei Hsu, Stefan Rotter, and Hui Cao. Customizing the angular memory effect for scattering media. *Physical Review X*, 11(3):031010, 2021.

[111] Maxime W Matthès, Yaron Bromberg, Julien de Rosny, and Sébastien M Popoff. Learning and avoiding disorder in multimode fibers. *Physical Review X*, 11(2):021060, 2021.

[112] Shanhui Fan and Joseph M Kahn. Principal modes in multimode waveguides. *Opt. Letters*, 30(2):135–137, 2005.

[113] B.L. Heffner. Automated measurement of polarization mode dispersion using jones matrix eigenanalysis. *IEEE Photonics Technology Letters*, 4(9):1066–1069, 1992.

[114] Joel Carpenter, Benjamin J Eggleton, and Jochen Schröder. First demonstration of principal modes in a multimode fibre. In *2014 The European Conference on Optical Communication (ECOC)*, pages 1–3. IEEE, 2014.

[115] Joel Carpenter, Benjamin J Eggleton, and Jochen Schröder. Observation of eisenbud–wigner–smith states as principal modes in multimode fibre. *Nature Photonics*, 9(11):751–757, 2015.

[116] Wen Xiong, Philipp Ambichl, Yaron Bromberg, Brandon Redding, Stefan Rotter, and Hui Cao. Spatiotemporal control of light transmission through a multimode fiber with strong mode coupling. *Physical review letters*, 117(5):053901, 2016.

[117] Joel Carpenter, Benjamin J Eggleton, and Jochen Schröder. Comparison of principal modes and spatial eigenmodes in multimode optical fibre. *Laser & Photonics Reviews*, 11(1):1600259, 2017.

[118] Michael Horodynski, Matthias Kühmayer, Andre Brandstötter, Kevin Pichler, Yan V Fyodorov, Ulrich Kuhl, and Stefan Rotter. Optimal wave fields for micromanipulation in complex scattering environments. *Nature Photonics*, 14(3):149–153, 2020.

[119] Philipp Ambichl, Wen Xiong, Yaron Bromberg, Brandon Redding, Hui Cao, and Stefan Rotter. Super-and anti-principal-modes in multimode waveguides. *Physical Review X*, 7(4):041053, 2017.

[120] Sébastien M Popoff, Geoffroy Lerosey, Rémi Carminati, Mathias Fink, Albert Claude Boccara, and Sylvain Gigan. Measuring the transmission matrix in optics: an approach to the study and control of light propagation in disordered media. *Physical review letters*, 104(10):100601, 2010.

[121] SM Popoff, Geoffroy Lerosey, Mathias Fink, Albert Claude Boccara, and Sylvain Gigan. Controlling light through optical disordered media: transmission matrix approach. *New Journal of Physics*, 13(12):123021, 2011.

[122] John A Neff, Ravinda A Athale, and Sing H Lee. Two-dimensional spatial light modulators: a tutorial. *Proceedings of the IEEE*, 78(5):826–855, 1990.

[123] Sylvain Gigan, Ori Katz, Hilton B de Aguiar, Esben Ravn Andresen, Alexandre Aubry, Jacopo Bertolotti, Emmanuel Bossy, Dorian Bouchet, Joshua Brake, Sophie Brasselet, et al. Roadmap on wavefront shaping and deep imaging in complex media. *Journal of Physics: Photonics*, 4(4):042501, 2022.

[124] Eugene P. Wigner. Lower limit for the energy derivative of the scattering phase shift. *Phys. Rev.*, 98:145–147, Apr 1955.

[125] Felix T. Smith. Lifetime matrix in collision theory. *Phys. Rev.*, 118:349–356, Apr 1960.

[126] Philipp Ambichl, Andre Brandstötter, Julian Böhm, Matthias Kühmayer, Ulrich Kuhl, and Stefan Rotter. Focusing inside disordered media with the generalized wigner-smith operator. *Physical review letters*, 119(3):033903, 2017.

[127] Dorian Bouchet, Stefan Rotter, and Allard P Mosk. Maximum information states for coherent scattering measurements. *Nature Physics*, 17(5):564–568, 2021.

[128] Roy J Glauber. The quantum theory of optical coherence. *Physical Review*, 130(6):2529, 1963.

[129] Marc-Olivier Renou, David Trillo, Mirjam Weilenmann, Thinh P Le, Armin Tavakoli, Nicolas Gisin, Antonio Acín, and Miguel Navascués. Quantum theory based on real numbers can be experimentally falsified. *Nature*, 600(7890):625–629, 2021.

[130] Ming-Cheng Chen, Can Wang, Feng-Ming Liu, Jian-Wen Wang, Chong Ying, Zhong-Xia Shang, Yulin Wu, M Gong, H Deng, F-T Liang, et al. Ruling out real-valued standard formalism of quantum theory. *Physical Review Letters*, 128(4):040403, 2022.

Appendices

Appendix A

Why complex numbers?

In our first attempt at modelling speckle patterns in Chapter 1, we made use of complex numbers to describe the underlying field. As this procedure is quite ubiquitous in wave theory, and a common source of confusion, here is a good opportunity to discuss it and unveil a few non-trivial aspects of it. This will serve as a retrospective catharsis for the puzzled student I was on the matter, and might be useful for future students.

Complex numbers are traditionally used to describe waves, such as sound or light, and yet those are fundamentally real quantities (density field and electric field, respectively). This can cause some rightful confusion. However, it all makes sense. Let us consider any physical quantity x, and define an artificial complex quantity $\tilde{x}$ associated to it, such that $\mathrm{Re}(\tilde{x}) = x$. This means that the complex version is the real quantity plus some imaginary part, which is arbitrary. The first thing to realise is that we can always use $\tilde{x}$ instead of x in any equation of physics implying x, as long as this equation is *linear* in x [50, Chapter 23.1]. Indeed, if the equation is linear, the real and imaginary parts of $\tilde{x}$ will always be decoupled, as only nonlinear terms can mix them up. It follows that, if we take the real part of an equation at any stage of a calculation using $\tilde{x}$, we get what we would have got if we had started with x in the first place. We can then just solve our equations of physics using $\tilde{x}$ and keep somewhere in the back of our mind that the true physical quantity is hidden in the real part.

The linear vs non-linear aspect is essential. To illustrate this, let us consider the following examples. The first example is the potential energy of a mass m in a uniform gravity field g at a height x ($E = mgx$), and the second is the potential energy of a body in a Hookean potential of constant k at a distance x from the equilibrium position ($E = kx^2/2$). We now replace x by a complex quantity $\tilde{x} = x + iI$, with I any real number. Using this $\tilde{x}$ in our expressions of energy yields a

new complex version of energy $\tilde{E}$. Using $\tilde{x}$ makes sense only if taking the real part of $\tilde{E}$ yields E, that is, what we would have had in the first place if we had not been playing with complex numbers. Let us check this:

$$\begin{aligned} \tilde{E} &= mg\tilde{x} & \tilde{E} &= k\tilde{x}^2/2 \\ \tilde{E} &= mgx + imgI & \tilde{E} &= k(x^2 - I^2)/2 + ikxI \\ \mathrm{Re}(\tilde{E}) &= mgx & \mathrm{Re}(\tilde{E}) &= k(x^2 - I^2)/2 \\ &= E & &\neq E \end{aligned}$$

In the first case, the potential is linear and the real part of the complex energy is indeed the same as what we would have by simply using x. In the second case, the non linearity of the Hookean potential couples the real and imaginary parts of $\tilde{x}$, leading to the presence of an artefactual term in the real part. Therefore the real part of the complex energy is not the same as the original one. We cannot use a complex version of x to manipulate this equation.

Note that the parameters of the problem, for example g in the first case, must remain real for the present purpose, as a complex value could also mix the real and imaginary part. However there exists situations where the physical parameters themselves can be allowed to be complex. The coexistence of complex parameters and complex variables, in a twist of mathematical beauty, typically allows the description of additional aspects of phenomena. For example, this is the case of evanescent fields, which naturally emerge from inserting a complex solution of the Snell-Descartes law for the wavenumber into a complex wave. An analogous example is absorption of light, which naturally emerges from allowing complex values to the refractive index.

The use of complex quantities in the two examples shown above is obviously not pertinent, those are purely illustrative. However there is a particular class of phenomena where the benefit of complex numbers is immense, which is oscillations. Most oscillatory phenomena follow a second order differential equation in time and/or space, admitting solutions of the form $u = A\cos\phi$, with ϕ containing the appropriate time and space dependence. Let us construct a complex quantity out of this, $\tilde{u} = u + iI$. Remember that I is arbitrary, and is entirely up to us. There exists, it turns out, one supremely convenient choice for I in this particular case, which is $A\sin\phi$ (sometimes fancifully called the harmonic conjugate). By making this particular choice we find $\tilde{u} = A\exp i\phi$, according to Euler's formula. At the end of the day, we simply traded a cos for an exp, but it is known that exponentials are remarkably simpler to manipulate than trigonometric functions, particularly when derivatives and factorisations are involved. This is the fundamental reason why

waves are commonly expressed as complex quantities. Although this is an oblivious reflex of the physicist, it is important to be aware of the thought process behind, and to keep in mind that the true physical quantity is real, hidden in the real part. Once this is understood, we no longer need to explicitly take the real part of a result, or add the complex conjugate terms, as is sometimes seen.

It is worth being aware however, that another more radical point of view exists on the matter (in the particular case of light) which considers the wave to be an actual complex quantity. This is a counter-intuitive position, very conducive to passionate debates. At the end of the day, to decide the issue, one may wonder: can we not measure the field and see? It turns out that the electric field is *not* measurable in the optical domain. This might be surprising because we inherit from classical physics a misleading picture of what an electric field does. Indeed, we might think that in principle the electric field of a light wave can be measured directly by simply placing a test charge in the field and measure its motion. However, this picture of the oscillating charge is in fact only true in the limit of low-frequency waves. In reality, the interaction between the charge and the field is a quantum process and occurs in discrete packets. For low frequency waves, such as radio waves, the energy packets are small enough to give the illusion of continuity, and the picture of the oscillating charge is approximately correct [128] (all radio-based technology relies on the idea that we directly measure the field). In the optical domain however, this is no longer true. Once we realise that the field cannot be directly measured, the idea of a complex field might seem less absurd.

A very analogous discussion exists concerning the wavefunction of quantum mechanics, which is not measurable and is indeed a fundamentally complex quantity. In fact, the possibility of a real-valued formulation of quantum mechanics has recently been proved falsifiable [129], and indeed experimentally ruled out [130]. This is a whole debate of its own, but I got to stop somewhere[1].

[1] To quote a famous physicist.

Appendix B

Path-length distribution

In section 3.2 we mentioned the path-length distribution in the sphere, where one of our assumptions was that the coherence length of the light source is large compared to the spread in the path-length distribution. This distribution was derived in [43], in the context of studying gas absorption in integrating spheres. Here I provide an alternative derivation.

Before turning to the problem of path-length distribution, we might ask the simpler question "what is the average path-length in the sphere?". This turns out to be a non-trivial question, and as the same non-triviality is found in deriving the path-length distribution, it is a good starting point. This question on its own is not a well posed problem, we must specify how a path is defined. If we use the definition we have been using in our model, that is, a succession of straight lines joining any of the M surface elements of the sphere, the answer turns out to be undefined. Indeed there are M paths of (approximately) length $\overline{z}$, M^2 paths of length $2\overline{z}$, M^3 paths of length $3\overline{z}$, etc. The average is then

$$\frac{\sum_{n=0}^{\infty} n\overline{z}M^n}{\sum_{n=0}^{\infty} M^n} = \text{undefined.} \tag{B.1}$$

In the infinite population of paths, the number of paths of a certain length increases with that length. The average length in that population is therefore undefined. We can still make sense of the notion of average path-length if we introduce power. If, when computing the average above, we give a weight to each path equal to the power carried by that path, we obtain a finite answer. We saw that the Lambertian reflectance and spherical geometry imply that power is equally distributed among the paths. This means that a path containing N reflections carries a power

proportional to $(\rho/M)^N$. When introducing this weighting, we have

$$\frac{\sum_{n=0}^{\infty} n\overline{z}\rho^n}{\sum_{n=0}^{\infty} \rho^n} = -\frac{\overline{z}}{\ln \rho}. \tag{B.2}$$

Turning now to path-length distribution. With this new notion of path-length weighted by power, finding the path-length distribution becomes a very simple task, as it comes down to finding the power as a function of path-length. Indeed the power carried by a path of length z is proportional to ρ^N, with N the number of reflections along the path, which is approximately $z/\overline{z}$. Using an exponential form we have $f(z) \propto \exp(\ln \rho \, z/\overline{z})$, and after normalising we have

$$f(z) = -\frac{\ln \rho}{\overline{z}} \, e^{\ln \rho \, \frac{z}{\overline{z}}}. \tag{B.3}$$

This yields the previous result (B.2) for the average path-length when computing $\int_0^\infty z f(z) \mathrm{d}z$. It also allows us to compute the spread in path-length, that we mentioned in section 3.2. A measure of spread is the standard deviation of the distribution, given by $\sigma_z^2 = \int_0^\infty z^2 f(z) \mathrm{d}z - (\int_0^\infty z f(z) \mathrm{d}z)^2$, which gives $\sigma_z = -\overline{z}/\ln \rho$, the same as the average path-length (it is a property of the exponential distribution, that the mean is equal to the standard deviation).

Appendix C

Geometric series solution

In section 3.2, we used an integral approximation to obtain a simpler form for Eq. (3.14). Here, we give the exact solution obtained using geometrical series instead. We start from Eq. (3.12):

$$S = \left| \frac{\sum_N \rho^N \left(e^{iN\mu - N\sigma^2/2} \right)}{\sum_N \rho^N} \right|^2 ,$$

and use the standard relation of geometric series $\sum_{n=0}^{\infty} r^n = 1/(1-r)$, which gives

$$S = \left| \frac{1-\rho}{1-\rho e^{i\mu-\sigma^2/2}} \right|^2 \tag{C.1}$$

$$= \frac{(1-\rho)^2}{1+\rho^2 e^{-\sigma^2} - 2\rho e^{-\sigma^2/2}\cos\mu}. \tag{C.2}$$

Note that Eq. (C.2) yields a non-zero similarity when μ and σ tend to infinity, equal to $(1-\rho)^2$. This is a surprising artefact of the model. However this allows us to quantify the difference between Eq. (C.2) and Eq. (3.14). Indeed this difference generally[1] increases monotonically, and as Eq. (3.14) does tend to zero, $(1-\rho)^2$ is of the order of the maximal difference between them. A maximal difference of 0.01 if found for $\rho = 0.9$, which we shall set as the critical value below which geometrical series must be used. This critical value is of course arbitrary and depends on the level of accuracy desired.

[1] This depends on the relative behaviour of μ and σ as a function of the variable of interest, but is correct in most cases.

Appendix D

Neglecting the σ term

At several occasions we neglected the σ term in Eq. (3.14) whenever the μ term was non-zero. We justify this here in the general case.

We start by developing the denominator in Eq. (3.14), which gives the terms

$$1 - \frac{\sigma^2}{\ln \rho} + \frac{\sigma^4}{4 \ln \rho^2} + \frac{\mu^2}{\ln \rho^2}. \tag{D.1}$$

As all terms are positive, we see that if $\mu = |\ln \rho|$, we are at least at the HWHM of the similarity profile. Evaluating the terms at $\mu = |\ln \rho|$, and assuming $\sigma = \alpha\mu$ with α a proportionality constant close to unity (this is true in all cases studied in this thesis where μ is non-zero), we have

$$1 - \alpha^2 \ln \rho + \frac{\alpha^4}{4} \ln \rho^2 + 1. \tag{D.2}$$

As $\ln \rho$ is a small number, the leading σ term is the second term. Keeping only the second term and inserting back in the similarity, we have

$$S = \frac{1}{2 - \alpha^2 \ln \rho} \tag{D.3}$$

$$\approx \frac{1}{2} + \frac{\alpha^2 \ln \rho}{4}. \tag{D.4}$$

With our value of reflectivity $\rho = 0.918$, the additional term is -0.02 (for $\alpha = 1$), which is a very small correction at the HWHM. This justifies that we can neglect the σ term in the original expression of the similarity (3.14) whenever α is of the order of unity (or smaller).

In all cases of Table 3.2, α^2 is 0.125, except for axial displacement where it is 1.25. Note that having $\mu = 0$, such as in the case of transverse displacement, is equivalent

to $\alpha = \infty$. There is a certain angle between axial and transverse displacement where neglecting the σ term starts to fail.

Appendix E

Deriving $P(s=1|\theta)$

In Chapter 3, we used the quantity $P(s=1|\theta)$, which is the probability of s being 1 for a given θ. Put into words, this is the fraction of chords that touch both hemispheres, among all those that form an angle θ with the z-axis. It turns out that this problem becomes (almost) straightforward once we realise the following fact, that we shall refer to as proposition 1 (even though there is no proposition 2):

Proposition 1. *The set of chords that point around a certain direction ("around" meaning within an infinitesimal solid angle) cross uniformly any disk perpendicular to that direction.*

Let us first prove proposition 1, which is somewhat counter-intuitive, before proceeding to the determination of $P(s=1|\theta)$. Consider the set of chords that point in a given direction (say, for simplicity, the vertical direction) within an infinitesimal solid angle $\mathrm{d}\Omega$. With what density do those chords cross the (horizontal) equatorial disk? If we mentally cover the sphere with small surface elements, the set of all possible chords is given by all the possible lines joining two such elements. Among all the possible chords, we are interested in those that point around the vertical direction. Intuitively, we might think of this as looking at the sphere from above and consider the lines that connect two elements along the line of sight. With this picture however, the number of chords diverge on the edge of the sphere, and is not uniform. The problem with this picture is that it misses the implication of the solid angle. The number of surface elements do diverge on the edge, but concurrently the number of chords departing from each element decreases in the same proportion. This is because the number of chords connected to an element on one side of the sphere is equal to the number of elements on the other side contained within a cone of solid angle $\mathrm{d}\Omega$, which goes to zero on the edge.

This is shown in more details in Fig. E.1. D is the equatorial disk, of which $\mathrm{d}s$ is a surface element. We want to know how many chords cross $\mathrm{d}s$. We consider each

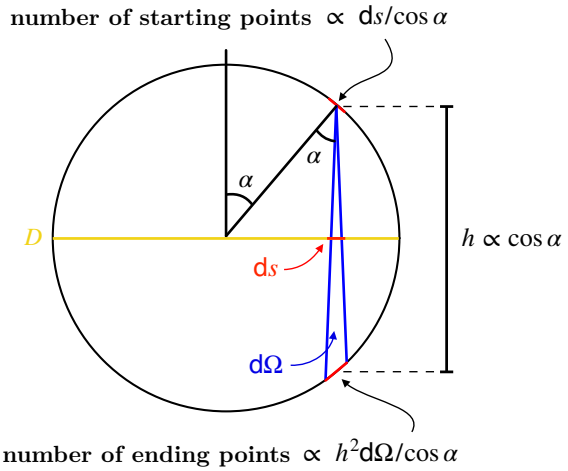

Figure E.1: Side view of the sphere, where we consider the set of chords pointing around the vertical direction. D is the equatorial disk, of which $\mathrm{d}s$ is a surface element. The area directly above $\mathrm{d}s$ on the upper surface is $\mathrm{d}s/\cos\alpha$. The area of the lower surface intersected by a cone of solid angle $\mathrm{d}\Omega$ starting at the upper surface is $h^2\mathrm{d}\Omega/\cos\alpha$. The total number of chords crossing $\mathrm{d}s$ is proportional to those two quantities, which is a constant.

chord as starting from an element of the upper surface and ending at an element of the lower surface. The number of starting elements directly above $\mathrm{d}s$ is proportional to the projection of $\mathrm{d}s$ onto the upper surface, which is equal to $\mathrm{d}s/\cos\alpha$, with α defined on the figure. For each element of the upper surface, the number of accessible elements on the lower surface is proportional to the area contained in a cone of solid angle $\mathrm{d}\Omega$, which is equal to $h^2\mathrm{d}\Omega/\cos\alpha$, with h the distance between the starting and ending element. The total number of chords crossing $\mathrm{d}s$ is proportional to the product of those two quantities. Moreover, as $h \propto \cos\alpha$, everything cancels out and the result no longer depends on the position of $\mathrm{d}s$. It follows that the chords cross D with a uniform density.

Now that we have proved proposition 1, we can turn to the determination of $P(s=1|\theta)$, which follows (almost) straightforwardly. Fig. E.2 shows a side view of the sphere with the separation between the two hemispheres denoted as D_0. Among the chords that point around a certain direction $\boldsymbol{u}$, those that touch both hemispheres (what we are interested in, remember) are those that are contained in the "shadow" of D_0 in the direction of $\boldsymbol{u}$. Additionally, proposition 1 tells us that the chords pointing around $\boldsymbol{u}$ cross uniformly the disk perpendicular to $\boldsymbol{u}$ (denoted D). Therefore $P(s=1|\theta)$ is proportional to the projection of D_0 onto D, from which it follows $P(s=1|\theta) = \cos\theta$, with θ the angle between $\boldsymbol{u}$ and the vertical axis.

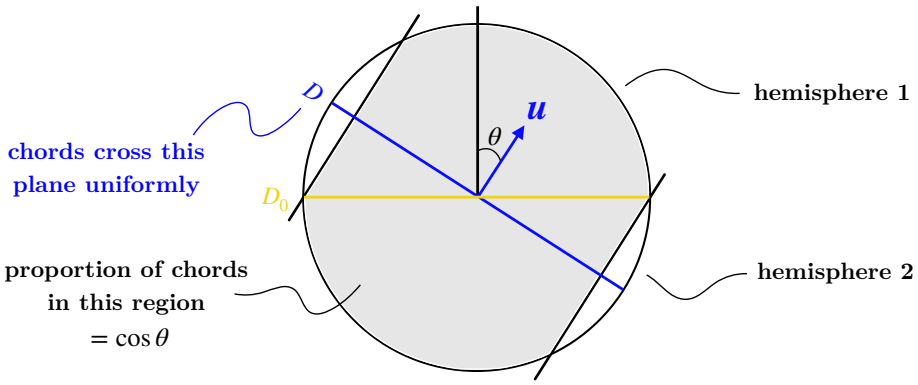

Figure E.2: Side view of the sphere with the separation between the two hemispheres forming the disk D_0. The chords pointing around the direction $\boldsymbol{u}$ cross uniformly the disk D. Among those, the chords that touch both hemispheres are contained in the shaded region. The proportion of chords in this region is equal to $\cos\theta$.